Laser cooling in thulium-doped solids

by

Chad William Hoyt

B. S., Bethel College, 1994

DISSERTATION

Submitted in Partial Fulfillment of the
Requirements for the Degree of

Doctor of Philosophy
Optical Sciences

The University of New Mexico

Albuquerque, New Mexico

May, 2003

Dedication

This work is dedicated to my wife, Jenni. Together we offer it to God, who reveals mysteries both natural and personal.

Acknowledgments

My wife is an unwavering support – my thankfulness for her is deeper than words. I am happy to have "grown up" in my research group at UNM. From its members there is a balance of professionalism, accountability, and fun. Mike Hasselbeck has been a tireless, unselfish and enjoyable help in recent years. Richard Epstein has encouraged me and shown me what it means to be a good scientist. My Advisor, Mansoor Sheik-Bahae, has positively fulfilled his title to such an extent that I consider myself quite fortunate. He has given me both freedom and challenges, and has shown a remarkable wisdom for their timing. His interest in and enjoyment of the lab, as well as an authentic open-door policy ensured his availability. I hope to have bright, respectful, and enjoyable mentors such as these in my future.

Fellow students and other research groups have graciously lent equipment and ideas. Carl and Pablo in the machine shop have rescued me many times with good solutions and mechanical skills. The administrative professionals in the physics department are an essential part of the research engine and I'm thankful for their efforts. Many helped with specific parts of the research – taken together, they are indispensable to the project: Diplom students Frank Wipperman, Mike Thieme, and Dominique Buchenau; PURSUE students Ameer Bauer, Frank Garcia, and Jeff McDaniel; Majid Ebrahimzadeh and Ian Hoffman who assisted with the OPO; Babak Imangholi and Joachim Zeller who shared much help with me; and Richard Epstein, Brad Edwards, Al Gibbs, Jared Thiede and John Valencia from Los Alamos. I'm indebted to gifted teachers like Ivan Deutsch and Sudhaker Prasad who make elegant parts of physics accessible and exciting. I also thank my dissertation committee for their time and effort: Steve Brueck, Richard Epstein, Wolfgang Rudolph, and Mansoor Sheik-Bahae.

Laser cooling in thulium-doped solids

by

Chad William Hoyt

ABSTRACT OF DISSERTATION

Submitted in Partial Fulfillment of the
Requirements for the Degree of

Doctor of Philosophy
Optical Sciences

The University of New Mexico

Albuquerque, New Mexico

May, 2003

Laser cooling in thulium-doped solids

by

Chad William Hoyt

B. S., Bethel College, 1994

Ph.D, Optical Sciences, University of New Mexico, 2003

Abstract

Theoretical and experimental research in cooling thulium-doped heavy metal fluoride glass is presented. The first observation of anti-Stokes fluorescence cooling in a thulium-doped material is reported. Cooling to 24 K below ambient with a multiple pump-pass scheme is attained, as well as results yielding 2.2 W of absorbed power and a cooling power of 73 mW. Single-pass cooling results agree with a simple model for anti-Stokes fluorescence cooling that includes considerations of quantum efficiency and parasitic heating mechanisms. Issues relating to a practical optical refrigerator are examined, including a general model for the effects of multiple pump passes. Spectroscopic studies of Tm^{3+}:ZBLANP – including Fourier-transform infrared absorption, photoluminescence excitation, and fluorescence measurements – allow low-temperature cooling behavior to be predicted. Such modelling indicates the feasibility of cooling to below 150 K.

Contents

List of Figures

List of Tables

Chapter 1

Introduction

The idea of using radiation to cool matter in the solid state was first proposed by Pringsheim in 1929 [24]. Its first observation, however, did not take place until 1995 [21]. The anti-Stokes fluorescence cooling process is illustrated in Fig. 1.1 with a simplified energy level structure of a member of an dopant ensemble in a transparent solid host. A laser excites the dopant atom, which absorbs light at energy $E_1 - E_0$. The ensemble thermalizes within the glass host by absorbing vibrational energy contained in the host. The atom illustrated in the figure decays to level E_0 by releasing fluorescent light at energy $E_2 - E_0$. In this simplified picture, the fluorescent light carries away thermal energy of magnitude $E_2 - E_1$. In order to achieve net cooling in such a system, the host must be pure (*i.e.* low parasitic absorption), the transition from levels E_2 to E_0 must be primarily radiative (*i.e.* high quantum efficiency) and the fluorescence must be efficiently extracted from the host. Each of these issues will be addressed in Chapters 2 and 4 below.

Practical cooling systems based on the interaction of narrow-band radiation and solid-state matter have many benefits [1]. Thermoelectric coolers (TEC) are able to reach 180 K. Optical coolers share the benefit of low mechanical vibrations with

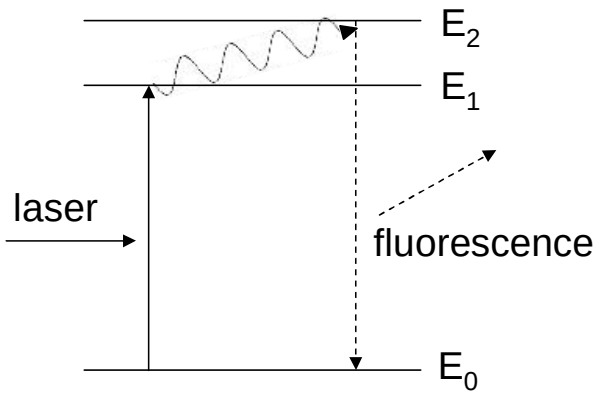

Figure 1.1: Anti-Stokes fluorescence.

TEC's, but can cool at temperatures as low as 100 K [2]. Mechanical coolers such as Stirling cycle coolers can reach temperatures of order 10 K but are relatively large and cause vibrations that are problematic for many applications such as focal-plane sensor elements. Optical coolers do not have this problem and cause low electromagnetic interference in the region of cooling. They can be based on long-lived and rugged diode laser systems. A representation of such an optical cooler is shown in Fig. 1.2, where a cold finger is attached to the doped-glass cooling element.

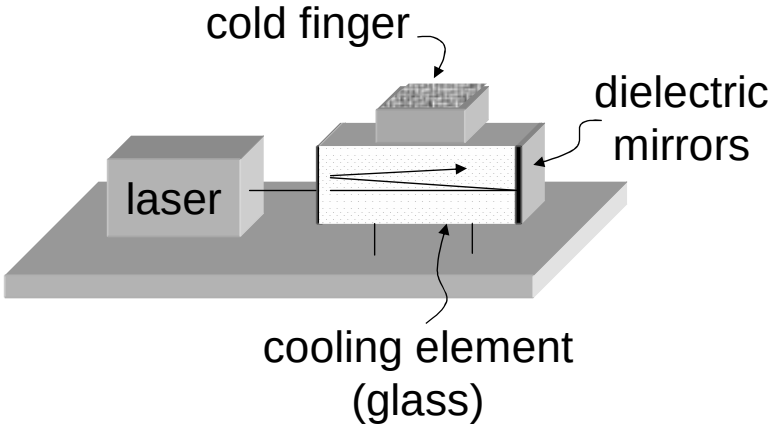

Figure 1.2: Cryogenic optical refrigerator.

As discussed below, rare-earth atoms in solid hosts generally have high quantum efficiency. This makes them good dopants for optical coolers. Further, cooling efficiency scales inversely with the dopant energy gap used for cooling. For ytterbium this gap is ~ 1.25 eV and for thulium it is ~ 0.7 eV. From this basic scaling relation we expect thulium-based coolers to perform nearly twice as efficiently as those based on ytterbium.

The dissertation below describes the development of a thulium-based optical cooling system. Cooling efficiencies of greater than 3% are demonstrated, and temperature changes of -24 K are achieved along with predictions for cooling to 150 K. This chapter outlines the historical development of solid-state cooling as well as some of the important physical issues in solid-state cooling. It is the most theoretical of all chapters, giving a basic understanding of the origin of the energy level structures and time scales necessary for cooling. The main ideas will be used and mentioned later in the dissertation so one may choose to skip Sec. 1.2 altogether. Section 1.1 highlights the achievements of experimental cooling research and Sec. 1.3 summarizes the organization of the manuscript.

1.1 Historical development

Parallel to advances in laser cooling of atoms and ions in dilute gas phase, major experimental progress has recently been made in laser cooling of matter in solid and liquid phases [21, 22]. Laser refrigeration of solids can potentially lead to the development of an all solid-state cryocooler (illustrated in Fig. 1.2) that can be used for a variety of applications such as cooling sensors and electronics [23]. Although the notion of using blue-shifted fluorescence to decrease the temperature of an object [24] was initially dismissed by some as contrary to the second law of thermodynamics, Landau established its fundamental validity in 1946 [25]. Kastler suggested that rare-

earth doped crystals might provide a medium for solid-state cooling resulting from anti-Stokes emission [26]. However, obstacles to its realization remained – primarily the highly efficient, heat-generating processes typically associated with absorption in optical materials.

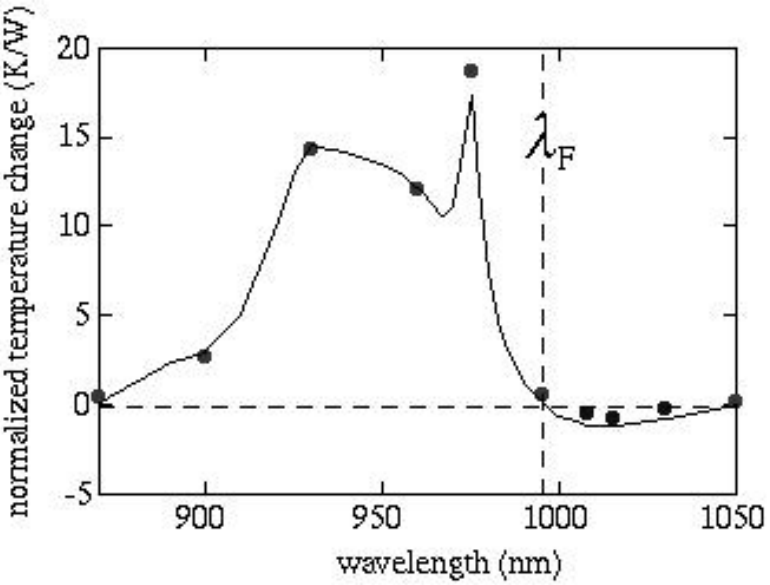

Figure 1.3: First solid-state laser cooling in ytterbium-doped glass. Data is taken from Ref. [21].

The first solid to be cooled as a result of interaction with light was a ytterbium-doped fluorozirconate glass [21]. Results of the experiment are shown in Fig. 1.3, where normalized temperature change is plotted against pump wavelength. The vertical line indicates mean fluorescent wavelength. A local decrease in temperature was detected by a photo-thermal deflection technique when the sample was pumped by a Ti:Sapphire laser beam. Bulk cooling was also detected directly from measurements with a calibrated thermally-sensitive camera. The results shown in Fig. 1.3 correspond to a single pass of the pump beam. Subsequent multiple-pass schemes have improved cooling in Yb^{3+}:ZBLANP to -70 K from room temperature. To date, thulium-doped glass is the second and only other class of solid to achieve bulk cool-

ing. First cooled to 1.2 K below room temperature in 2000 [27], bulk cooling in a thulium-doped fluorozirconate by -24 K from room temperature is described below.

Ytterbium-doped glasses have been cooled to 70 K below room temperature and have been reported cooled at temperatures as low as 77 K [28]. Edwards *et al.* demonstrated a prototypical cryogenic refrigerator based on Yb^{3+}:ZBLANP pumped with a 1.6 W Ti:Sapphire laser and measured a temperature decrease of 48 K from room temperature [23]. Cooling from low starting temperatures in various Yb^{3+}-doped glasses has been observed, suggesting that a cryogenic refrigerator with an extended dynamic range can be built. Mungan *et al.* observed local cooling in a Yb^{3+}:ZBLANP sample at temperatures between 100 and 300 K, maintaining a cooling efficiency of $\sim$1% throughout this range [2]. Local cooling between 77 K and room temperature has been shown using photo-thermal deflection and spectroscopic techniques in a fluorochloride glass (Yb^{3+}:CNBZn), and a fluoride glass (Yb^{3+}:BIG), by Fernandez *et al.* [28]. The cooling efficiency was shown to change with temperature, varying between $\sim$2% and $\sim$0.6% in the two materials. Rayner *et al.* have cooled a Yb^{3+}-doped fiber [29]. Gosnell cooled a Yb^{3+}-doped fiber by an amount $\Delta T = -65$ K from room temperature [30]. The temperature of the fiber was monitored through its temperature-dependant emission spectra. Epstein *et al.* have cooled a dielectric-mirrored Yb^{3+}:ZBLANP sample by 70 K from room temperature as measured directly with a thermocouple.

In addition to glasses, ytterbium-doped crystalline samples have been cooled. Crystals offer advantages over glass materials such as high thermal conductivity, improved ruggedness, and potentially larger absorption cross sections. Bowman and Mungan used photo-thermal deflection to demonstrate local cooling in a Yb^{3+}-doped $KGd(WO_4)_2$ crystal [31]. Epstein *et al.* observed bulk cooling in Yb^{3+}:YAG, recording a net sample temperature change of $\sim$8.9 K below room temperature [32]. They also cooled a sample of Yb^{3+}:Y_2SO_5 by 1 K below room temperature. Mendioroz *et*

al. recently showed local cooling in samples of Yb^{3+}:KPb_2Cl_5 crystal [33].

Optical cooling has been pursued in other condensed matter materials such as dyes and semiconductors [34, 35, 11]. Clark *et al.* excited rhodamine 101 dye with radiation at 1.96 eV and found that it cooled at a rate of 0.7 Kh^{-1} [22, 36]. A GaAs/GaInP heterostructure was studied for possible cooling by Gauck *et al.* [12]. They observed blue-shifted luminescence but did not see net cooling. Finkeißen *et al.* detected local cooling in the area of the pump beam spot due to anti-Stokes photoluminescence in a GaAs quantum well structure, recording a temperature drop of 7 K from liquid-nitrogen temperature [13]. As mentioned above, a requirement for net cooling is efficient extraction of anti-Stokes fluorescence from the solid. Due to their high refractive indices, luminescence trapping from total internal reflection remains a major obstacle to observing net cooling in semiconductor materials.

1.2 Physical background

Cooling atoms in the gas phase has shown remarkable success in recent years [3, 4, 5, 6, 7]. As a result of interaction with laser radiation the random velocities associated with an ensemble of atoms are reduced. Insofar as these velocities can be assigned a temperature – defined for a body at equilibrium with respect to its surroundings in the presence of heat exchange [3] – cooling is observed.

Atomic cooling is illustrated in Fig. 1.4. An atom at thermal velocity $v = \sqrt{k_B T/m}$ and momentum mv absorbs a photon of momentum $\hbar k$. The inelastic collision results in a reduced atomic momentum in the direction opposite to the laser wavevector, $-\hat{\mathbf{k}}$. The atom subsequently spontaneously emits a photon into a random direction, which means the recoil momentum from this emission after many cycles of absorption and emission averages to zero. The net effect is a reduced velocity along the linear dimension of the laser wave vector. However, the fraction of atoms that are cooled

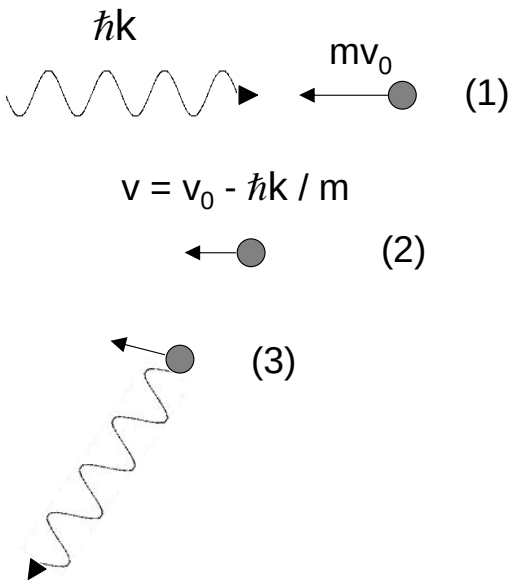

Figure 1.4: Laser cooling of atomic gases.

in an atomic beam with a thermal velocity distribution is limited due to the Doppler shift. Depending on the linewidth of the atomic transition, only atoms within a certain range of velocities will be in resonance with the laser. Certain methods are used to compensate for this effect, most prominently laser chirping and Zeeman-shifting. The former technique involves changing the frequency of the laser such that atoms will continue to absorb laser light even as they slow. The latter technique uses a current-carrying coil of tapered dimension to gradually decrease the strength of a magnetic field at the atomic beam that passes through the coil. This causes a gradual shift in atomic energy levels due to the Zeeman effect that compensates for the shift out of resonance as the atoms are slowed. In this manner all atoms below a certain initial velocity are cooled to a narrow velocity distribution. This compression is shown in Figure 1.5. The figure illustrates data from an early Doppler laser cooling experiment [8]. The dashed line is the initial thermal distribution of velocities and the solid line is the distribution after laser cooling. The arrow indicates the velocity

above which all atoms are out of resonance with the laser beam at all points.

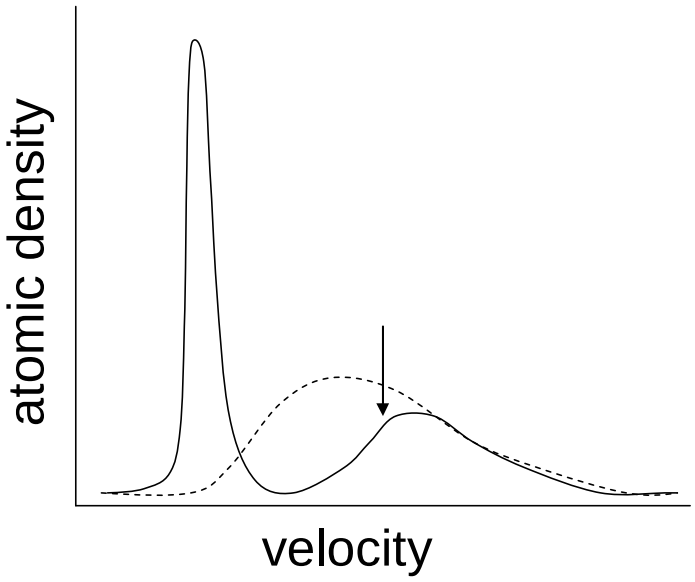

Figure 1.5: Phase space compression.

Atoms have been cooled using the Doppler technique to temperatures of order milliKelvin. Elegant trapping and cooling techniques involving both lasers and electromagnetic fields have further reduced temperatures to order nanoKelvin, even reaching Bose-Einstein condensation [9, 10]. Considering standard Doppler cooling of sodium atoms, a typical change in velocity magnitude upon absorption of a photon of light at $\lambda \sim 590$ μm is 3 cm/sec. A typical initial thermal beam velocity is 10^5 cm/sec. The net change in velocity in one dimension as described above corresponds to a change in energy of $\sim 10^{-24}$ J. The sodium transition has a lifetime of ~ 32 ns. One can define cooling efficiency as the ratio of cooling power to absorbed power – for sodium cooling, this ratio is $\sim 3\text{x}10^{-6}$. As will be discussed below, solid-state coolers produce cooling efficiencies of $\sim 3\text{x}10^{-2}$, a factor of 10^4 greater.

Like laser cooling in gases, solid-state laser cooling involves decreasing temperature through laser-atom interactions. Solid-state cooling is defined by a reduction

in average thermal vibrations of the constituent atoms in a solid host rather than a reduction in translational kinetic energy. The solid is in thermal contact with its surroundings, primarily through radiative coupling. Similar to other cooling mechanisms such as thermo-electric coolers, this heat load determines the final steady-state temperature of the solid for a given cooling power.

Solid-state laser cooling involves a particular solid material that presents an absorbing transition to the laser beam. This may include the energy band structure of a semiconductor [11, 12, 13] or an electronic transition for dopant atoms in hosts transparent to the laser radiation. In the latter scheme, a dopant ion is added to a solid host by substituting for a particular atomic species. The ion interacts with its surroundings primarily via an electrostatic Coulomb potential. For crystalline hosts the ion is surrounded by a system with long-range order and glass hosts present only short-range order to the ion. The Hamiltonian for the ion in a solid host can be written as

$$H_{ion} = H_0 + H_{ES} + H_{SO} + H_{CF}. \tag{1.1}$$

The first three terms on the right side of Eq. 1.1 describe the dominant terms of the bare ion. H_0 is the central-force Coulomb interaction, H_{ES} is the electrostatic interaction between electrons, and the spin-orbit interaction is included as H_{SO}. The perturbation due to the presence of a static crystal field arising from the host is H_{CF}. Energy states given by H_0 are labelled by quantum numbers n and l ($4f$ for rare-earth ions). The electrostatic interaction lifts the angular-related degeneracy in angular momentum, so states are labelled in the Russell-Saunders (R-S) scheme according to total spin and orbital angular momentum: ^{2S+1}L. The spin-orbit interaction lifts the degeneracy in total angular momentum ($J = L + S$) and states are labelled $^{2S+1}L_J$. For small spin-orbit coupling with respect to electrostatic inter-

actions, states are treated as eigenstates of L and S and R-S labelling is retained. However, as in the case of rare-earth atoms with large atomic numbers, spin-orbit coupling is significant and the states are eigenstates of J but not S or L. The interaction can cause mixing of states and leads to some confusion in the literature, notably for Thulium: some researchers label states as if L-S coupling were negligible while others use a label that indicates the dominant L-S term. Figure 1.6 illustrates energy level splittings using the latter interpretation for relevant transitions of the $1s^2 2s^2 2p^6 3s^2 3p^6 3d^{10} 4s^2 4p^6 4d^{10} 4f^{13} 5s^2 5p^6 5d 6s^2$ electronic configuration of thulium.

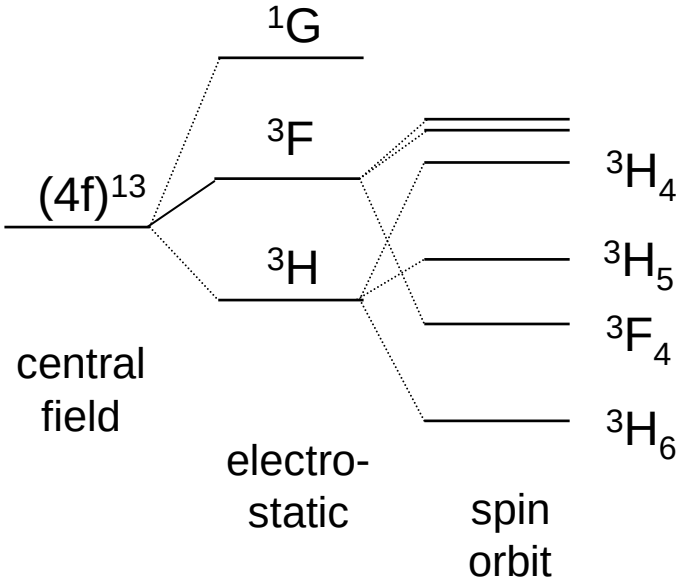

Figure 1.6: Rare-earth energy splittings.

The $^{2S+1}L_J$ levels are further split by the electric field caused by the surrounding host ions (ligands). An expression for the magnitude of the Stark splittings within each $^{2S+1}L_J$ manifold is derived from standard crystal-field theory [14, 15]. The matrix element of the energy splitting of a particular L-S state β to first order can be expressed as a spherical harmonic expansion of the charge density surrounding the ion. Treating all species as point charges the integral over the charge density

reduces to a sum over the $4f$ electrons of the dopant ion:

$$\begin{aligned} M &= \langle\psi_\beta|V_{CF}|\psi_\beta\rangle \\ &= \langle\psi_\beta|\sum_{kq} A^*_{kq} \sum_i r_i^k C_{kq}(\mathbf{r}_i)|\psi_\beta\rangle. \end{aligned} \tag{1.2}$$

In Eq. 1.2, $C_{kq}(\mathbf{r}_i)$ is a spherical tensor operator of rank k and projection q operating on the ith electron with an orbital radius r_i. A^*_{kq} is a crystal field parameter that is a sum over charges and positions of the ligands surrounding the ion. Orthogonality relationships simplify the above expression to only terms of rank two, four and six. It can then be expressed in terms of reduced matrix elements, 3-j and 6-j symbols for a particular L, S, J and $\mathrm{M_j}$ state, all of which are tabulated. For thulium-doped ZBLAN glass, the average ion-ligand distance is found to be 0.23 nm and the ligands are arranged with low symmetry in groups of eight [15]. For rare-earth dopants in glass, the magnitude of the matrix element in Eq. 1.2 is of order 10-100 cm^{-1} [16]. This is the intra-manifold splitting and is small relative to optical transitions ($\sim 6000\ \mathrm{cm}^{-1}$). As discussed below, the relationship between these values will enable relatively fast thermalization within manifolds, which is necessary for the cooling process.

The interaction between the dopant ion and host phonons is an important perturbation. It leads to fast transitions within a particular $^{2S+1}L_J$ manifold as well as radiationless transitions between manifolds. Rare-earth ions have relatively low electron-phonon interaction strengths due to their electronic structure: the optically-active 4f electrons are screened by the orbitals of the 5s, 5p and 6s electrons. This is illustrated in Fig. 1.7, which shows the radial wavefunctions for various electron orbitals. The Hamiltonian for the host can be expressed in terms of an ensemble of harmonic oscillators (phonon modes). These modes modulate the relative positions

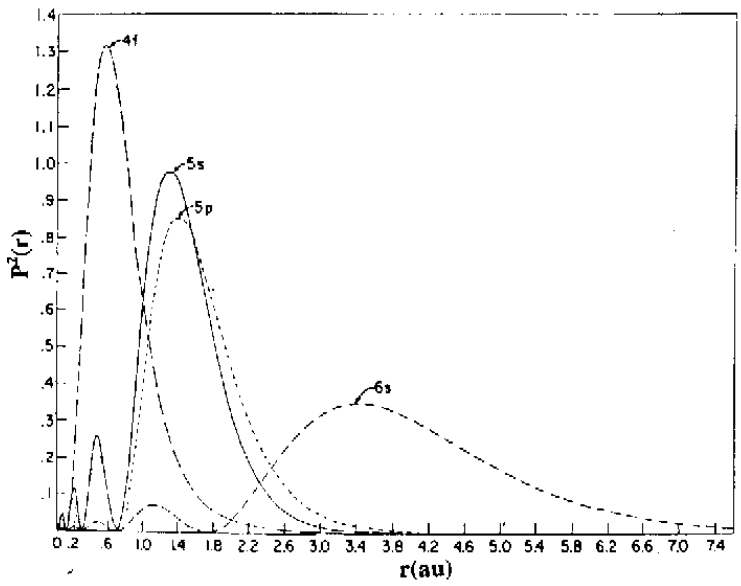

Figure 1.7: Radial wavefunctions for orbitals of rare-earth atoms, taken from Ref. [14, 17]. The optically active orbital in rare-earth materials is 4f.

of the dopant ions and ligands, which changes the crystal-field interaction. This perturbation is known as the deformation potential. The electron-phonon interaction can be considered a perturbation to the crystal-field Hamiltonian:

$$H'_{CF} = H_{CF} + \epsilon V. \tag{1.3}$$

Here H_{CF} is the crystal-field Hamiltonian described above, V is the energy of the perturbation, and ϵ is a parameter expressing the strength of the interaction. The latter term is expressed in terms of phonon creation and annihilation operators, $b_q^\dagger$ and b_q. For rare-earths in glasses $\epsilon \approx 0.075$ [14] so terms of order $\mathrm{O}(\epsilon^2)$ or greater are neglected in the expansion of the crystal-field Hamiltonian. Using Fermi's golden rule, the transition probability per frequency (energy) interval between electronic states of the dopant ion due to electron-phonon (ep) interactions is generally

$$w_{ep} = \frac{2\pi}{\hbar}|M_{ep}|^2\rho_f, \tag{1.4}$$

where ρ_f is the density of electron and phonon final states and $M_{ep} = \langle\Psi_f|\epsilon V|\Psi_i\rangle$ is the matrix element for the transition involving the total state vector. In this weak-coupling approximation the electron and phonon states are separable and the transition rate for direct phonon absorption (*i.e.* single-phonon) is

$$\begin{aligned} w_{ep}^{abs} &= \frac{\pi\omega_q}{Mv^2}|\langle\psi_f^{el}|V|\psi_i^{el}|^2|\langle n_q - 1|b_q|n_q\rangle|^2\rho_f \\ &= \frac{\pi\omega_q}{Mv^2}n_q|\langle\psi_f^{el}|V|\psi_i^{el}\rangle|^2\rho_f. \end{aligned} \tag{1.5}$$

Similarly, the probability for emission of a phonon of wave vector q is

$$w_{ep}^{em} = \frac{\pi\omega_q}{Mv^2}(n_q+1)|\langle\psi_f^{el}|V|\psi_i^{el}\rangle|^2\rho_f. \tag{1.6}$$

In Eq. 1.5 and 1.6, ω_q is the phonon frequency, M is the total mass of the host, v is the phonon velocity defined by its momentum, $|\psi_{i,f}^{el}\rangle$ are the initial and final electronic states of the dopant ion, and n_q is the phonon occupation number for wave vector q. If the width of the electronic transition is narrow with respect to the spread in phonon energies, the density of final electronic states can be approximated by a delta function. In the Debye model the phonon density of states is $3\Omega\omega_q^2/2\pi^2v^3$ for phonon frequencies below the Debye cutoff frequency [18] with volume Ω. The phonon occupation number is determined by Bose-Einstein statistics:

$$n_q = \frac{1}{e^{\hbar\omega_q/k_BT} - 1}., \tag{1.7}$$

where k_B is the Boltzmann constant and T is temperature. Total transition rates are obtained by integrating over electronic and phonon frequency intervals:

$$W_{ep}^{abs} = \frac{\omega_0^3}{2\pi\rho v^5\hbar}|\langle\psi_f^{el}|V|\psi_i^{el}\rangle|^2 n_0 \tag{1.8}$$

$$W_{ep}^{em} = \frac{\omega_0^3}{2\pi\rho v^5\hbar}|\langle\psi_f^{el}|V|\psi_i^{el}\rangle|^2 (n_0+1). \tag{1.9}$$

Here ω_0 is the center frequency for the transition with the corresponding phonon occupation number n_0, and $\rho = M/\Omega$. The matrix elements $|\langle\psi_f^{el}|V|\psi_i^{el}\rangle|$ are generally difficult to calculate analytically and are therefore determined experimentally.

For rare-earth ions in glass hosts the rates in Eq. 1.8 and 1.9 correspond to a time scale of order picosecond [16]. These rates differ only in their occupation numbers that have temperature dependence given by Eq. 1.7. Since radiative lifetimes between manifolds of interest for lasers or cooling are of order millisecond these phonon-caused transitions result in a thermal equilibrium within each manifold.

Consider the situation shown in Fig. 1.8. Figure 1.8(a) shows two $^{2S+1}L_J$ manifolds separated by an energy ΔE_{LS} large compared to the crystal-field splitting. The upper manifold shows two adjacent Stark-split levels $|1\rangle$ and $|2\rangle$ with exaggerated spacing. Considering only these two levels in Fig. 1.8 with total population $N = n_1 + n_2$, the rate equations for the two levels are

$$\dot{n_a} = -n_a W_{ab} + n_b W_{ba}$$

$$\dot{n_b} = -n_b W_{ba} + n_a W_{ab},$$

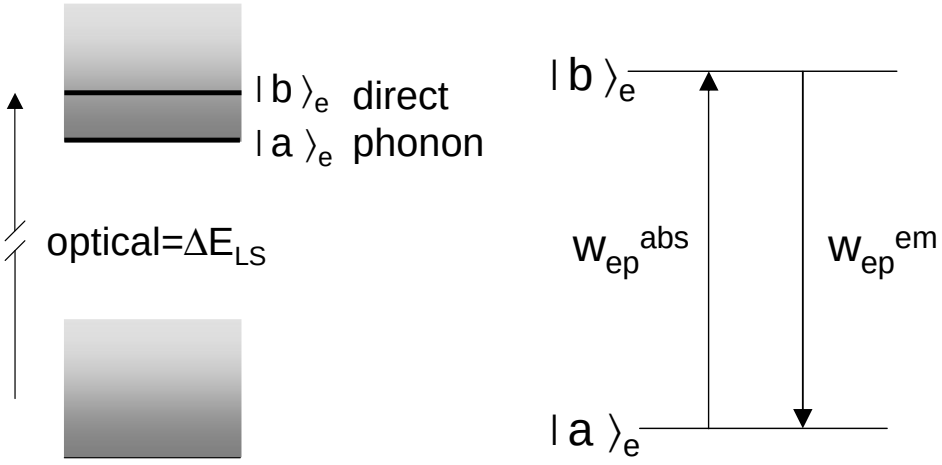

(a) (b)

Figure 1.8: Energy manifolds showing direct phonon transition.

In thermal equilibrium the time derivatives are zero and Eqs. 1.8, 1.9 and 1.7 can be used to give the relationship between populations:

$$n_b = n_a e^{-\hbar\omega_0/k_B T} \tag{1.10}$$

Equation 1.10 describes the intra-manifold population distributions under the assumptions given above. The distribution is illustrated in Fig. 1.9 for two $^{2S+1}L_J$ manifolds with lowest intra-manifold energies E_1 and E_2.

This situation can be referred to as local thermal equilibrium (LTE) [19] – it is the reason that solid-state systems exhibit differences in absorption and emission. Consider Fig. 1.10, which depicts two manifolds A and B again separated by an energy large with respect to the crystal field splitting. The intra-manifold population is illustrated in each manifold with energy increasing vertically and population increasing to the right in the figure. With no optical pumping from A to B as in

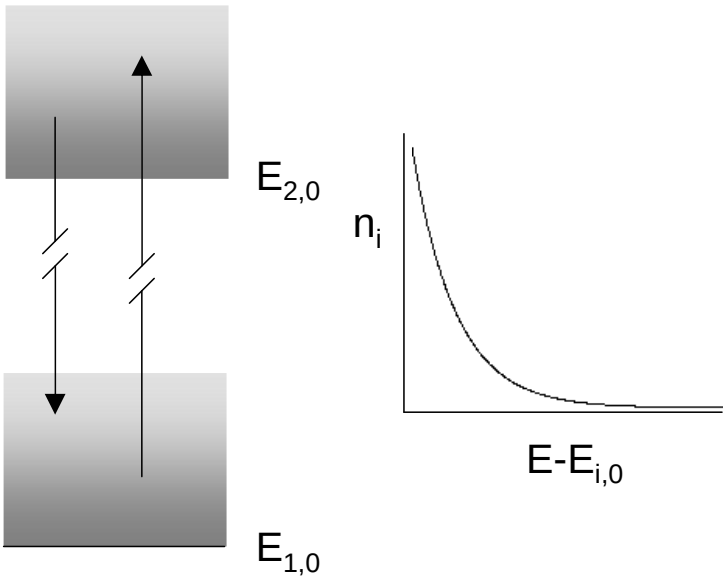

Figure 1.9: Local thermal equilibrium.

the right figure, the population in B is low with respect to A. Absorption varies with frequency according to the population in A, which means low absorption at low energies. In the presence of optical pumping as shown in the right figure both manifolds thermalize quickly with respect to radiative lifetimes. Strong absorption at high energies remains but the character of emission spectra is shaped by the thermal distribution of B, which can include strong emission at low frequencies as shown in the figure at right.

A formal relationship between absorption and emission cross-sections was established by McCumber [20]. It will be discussed in detail in Chpt. 5 in the context of spectroscopy of thulium-doped ZBLANP glass. The result is stated here for absorption and emission cross-sections ($\sigma_{abs}(\nu)$ and $\sigma_{em}(\nu)$) at frequency ν to indicate the explicit temperature dependence:

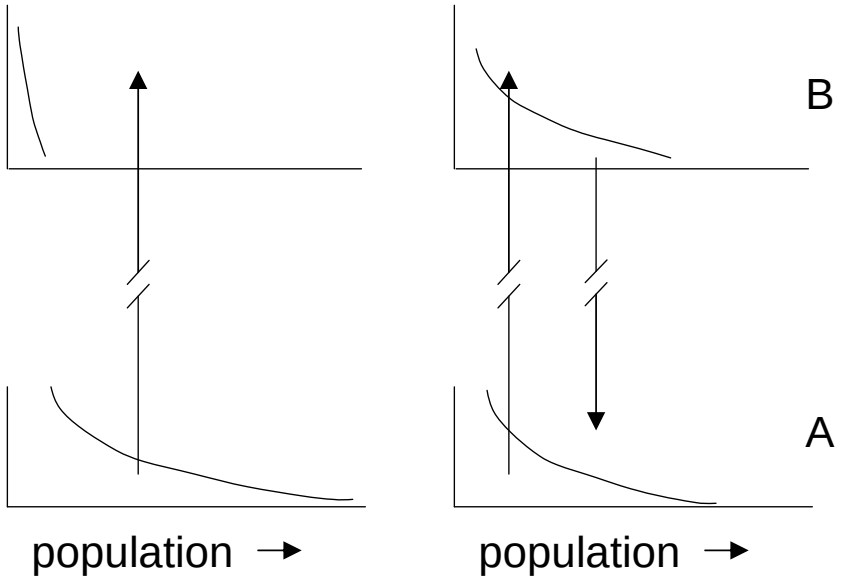

Figure 1.10: The character of emission and absorption.

$$\sigma_{abs}(\nu) = e^{(h\nu-\epsilon)/k_BT}\sigma_{em}(\nu). \tag{1.11}$$

One final consideration must be made with respect to electron-phonon perturbations to the electronic states of the dopant ion. Even in the weak-coupling approximation used above, higher-order phonon decay processes between manifolds are possible and must be described in order to compare their magnitude to those of radiative transitions. Higher-order terms in the perturbation expansion are used to describe multiphonon processes and are generally complicated. However, the ratio of probabilities for decay via a p-phonon emission process and a $p-1$ emission process of a single effective phonon mode with frequency ω_0 is ϵ (see Eq. 1.3). Therefore the non-radiative (nr) decay rate for a p-phonon emission process is

$$\begin{aligned} W_{nr}^{p} &= W_{nr}^{0}\epsilon^{p} \\ &= W_{nr}^{0}e^{ln(\epsilon)\Delta E/\hbar\omega_0}, \end{aligned} \tag{1.12}$$

where $\Delta E = p\hbar\omega_0$ is the electronic energy gap spanned by p phonons of energy $\hbar\omega_0$. The factor W_{nr}^{0} in Eq. 1.12 has temperature dependence given by Eq. 1.7 and is generally difficult to calculate analytically. However, the exponential behavior is confirmed through experiment by recording non-radiative rates for different dopant ions with various energy gaps (ΔE) in the same host. In this manner the factors in Eq. 1.12 can be determined. This expression describing multi-phonon decay has direct implications for quantum efficiency and will be discussed further in Chapters 2 and 5.

1.3 Manuscript organization

This dissertation is organized as follows. Chapter 2 outlines a simple derivation of the cooling power possible with anti-Stokes fluorescence. This includes considerations for non-unity external quantum efficiency, parasitic heating mechanisms, and an approximate expression for temperature change in terms of pump power and wavelength. Chapter 3 relates the details and important characteristics of the tunable pump source. Experiments that demonstrate cooling and the related efficiency scaling are presented in Chpt. 4. Chapter 5 reports the results of spectroscopic measurements and subsequent modelling of cooling efficiency as a function of temperature to investigate the minimum attainable temperature. The last chapter discusses future directions of this work. Calculations and experimental details that are not critical to the major point of the manuscript can be found in the appendix.

Each chapter begins with an introduction that highlights its contents and attempts to put results in a larger context. References to the literature are indicated where the interested reader can find further details or more comprehensive treatment. A list of salient results of the chapter is included as a method for reading only the most important parts of the chapter.

The results presented in this dissertation have been published in Physical Review Letters [27], Optics Letters [37], and the Journal of the Optical Society of America - B [38]. They were also presented in the post-deadline session at the conference on Quantum Electronics and Laser Science [39] and were highlighted in Nature [40].

Chapter 2

Simple model of anti-Stokes fluorescence cooling

2.1 Introduction

This chapter details a theoretical description of anti-Stokes fluorescence cooling in a rare-earth doped solid. Models for this process have recently been developed by other researchers and can be found in Ref. [23, 32, 41, 36, 31, 28, 30, 42, 43, 44, 45]. The treatment below most closely resembles that of Luo *et al.* [42], the major differences being that we include effects of non-unity quantum efficiency and a wavelength-independent background absorption. Various other models begin from a purely quantum mechanical treatment and reduce to similar results. Reference [45] compares cooling efficiencies in optical and Peltier coolers. Comprehensive considerations of thermodynamic physics involved in the cooling process (*e.g.* entropy-related limits) can be found in Ref. [25, 46, 47, 48]. The most important relations derived here and used in later chapters under various approximations are the following:

- Cooling power (Eq. 2.6)
- External quantum efficiency (Eq. 2.7)
- Thermodynamic heat load to sample (Eq. 2.11)

2.2 Model

Though general, the principle of anti-Stokes fluorescence cooling is seen in a description of our particular system. The samples consist of high purity ZBLANP (in mol%: 53% ZrF_4, 18% BaF_2,4-x%LaF_3, 3%AlF_3, 20%NaF, 2% PbF_2, x%TmF_3) cut from a fiber preform. The relevant energy manifolds for Tm^{3+} ions in this host are shown in Fig. 2.1 [49, 50].

Each level corresponds to a Stark-split manifold of several inhomogeneously-broadened levels. We use the transitions between the $^3H_6$ and $^3F_4$ manifolds for cooling. The cycle leading to anti-Stokes fluorescence cooling involves pump excitation, thermalization and spontaneous decay. As shown in Fig. 2.1, laser pump photons excite the dopant ensemble from the top of the ground state manifold to the bottom of the excited state manifold. The excitations thermalize within the upper and lower manifolds by absorbing vibrational energy from the host. The atoms decay through spontaneous emission (fluorescence) with a mean photon energy of $h\nu_f$, where ν_f is the mean fluorescent frequency. In the ideal case, for each absorbed pump photon of energy $h\nu$ an average energy $h\nu_f - h\nu$ is removed from the glass and carried out of the system. Cooling power is thus proportional to absorbed power (P_{abs}) and the difference between mean fluorescent and pump photon energies:

$$P_{cool} = P_{abs}\frac{h\nu_f - h\nu}{h\nu} = P_{abs}\frac{\lambda - \lambda_f}{\lambda_f}, \tag{2.1}$$

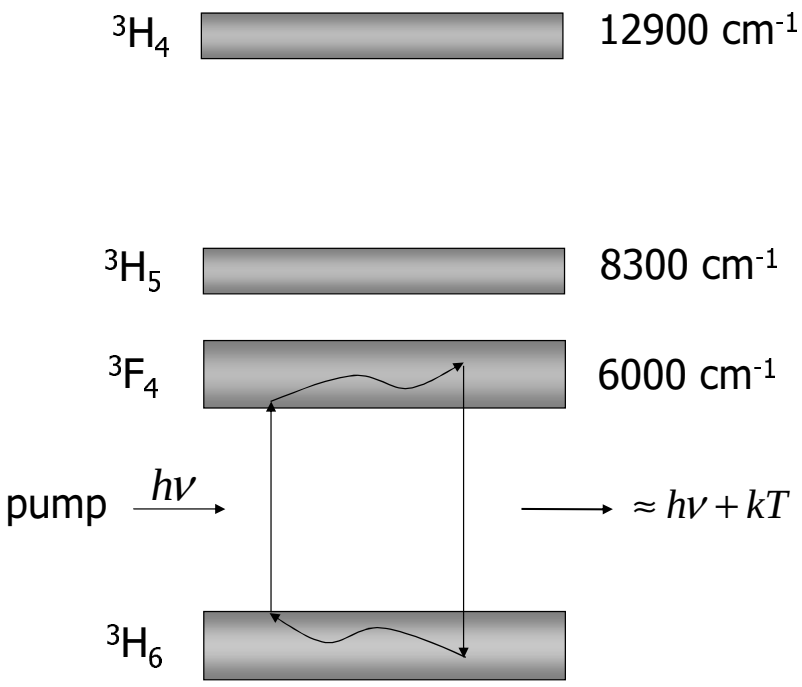

Figure 2.1: Energy manifold diagram of Tm^{3+}:ZBLANP after Ref. [49, 50]. The dopant ensemble is excited by the pump from the top of the ground state manifold ($^3H_6$) to the bottom of the excited state manifold ($^3F_4$). The atoms thermalize in both manifolds by absorbing vibrational energy from the host and the subsequent fluorescence, on average, removes an energy $h\nu_f - h\nu$ for each absorbed photon.

where λ and $\lambda_f = c/\nu_f$ are the pump and mean fluorescent wavelengths, respectively. Figure 2.2 shows room temperature emission and absorption spectrum of a 1 wt. % Tm^{3+}:ZBLANP sample. Details of spectroscopic experiments will be discussed in Chpt. 5. Defining cooling efficiency as $\eta_{cool} = P_{cool}/P_{abs}$, Eq. 2.1 gives the fundamental limit on cooling performance. It suggests that, for a given material, longer pump wavelengths produce higher efficiencies. In practice, however, diminished pump absorption at long wavelengths due to the thermal distribution of the ground-state population limits the useful maximum pump wavelength. Moreover, parasitic absorption due to uncontrolled impurities further limits the effective range of long-wavelength excitations. The practical range of the energy difference $h\nu_f - h\nu$

is of the order of thermal energy (k_BT) as a consequence of the ground-state Boltzmann distribution. Therefore, Eq. 2.1 indicates that Tm^{3+}-doped materials with $h\nu_f \approx 0.7$ eV have the potential to cool nearly twice as efficiently as Yb^{3+}-doped materials with $h\nu_f \approx 1.25$ eV. This is illustrated in Fig. 2.3, which shows the relative energy gaps for four rare-earth atoms: ytterbium (~ 1 μm), thulium (~ 2 μm), holmium (~ 2 μm), and dysprosium (~ 3.5 μm).

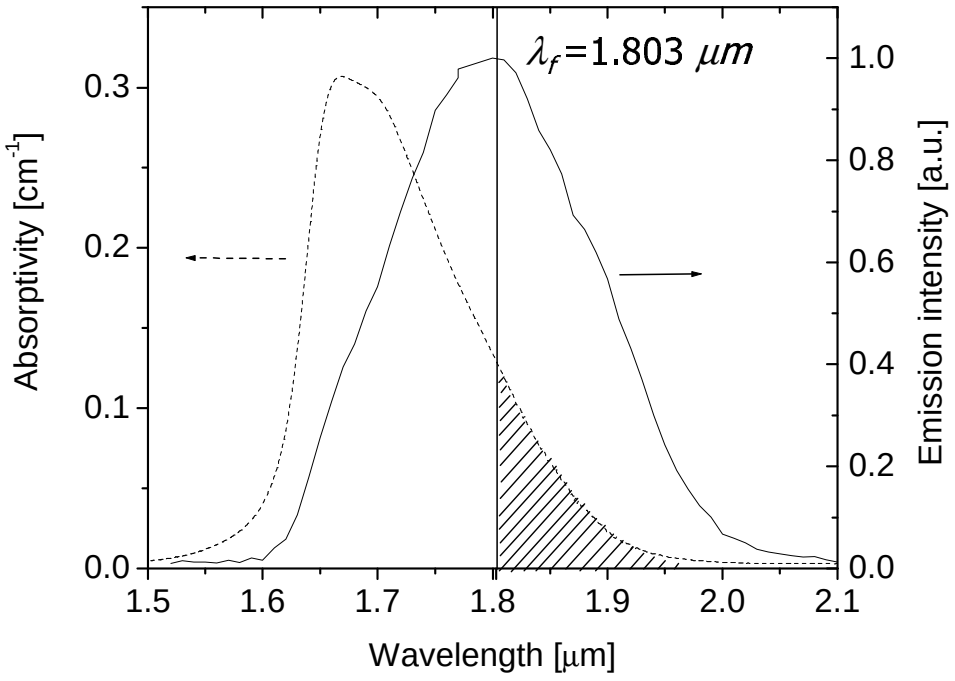

Figure 2.2: Absorptivity and fluorescence spectra of 1 wt.% Tm^{3+}:ZBLANP. The dotted curve is absorptivity data obtained with an FTIR photo-spectrometer, and the solid curve is fluorescence data obtained with a monochrometer and PbS detector. The vertical dashed line marks the mean fluorescent wavelength at 1.803 μm, and the shaded area indicates the pump wavelength region where cooling is expected.

Although dopant ions with lower energy gaps such as rare-earths shown in Fig. 2.3 can produce more efficient cooling, they will generally be subject to higher non-radiative decay rates that are strongly host-dependent. This dependence is due to phonon energy distributions that vary with material composition and symmetry.

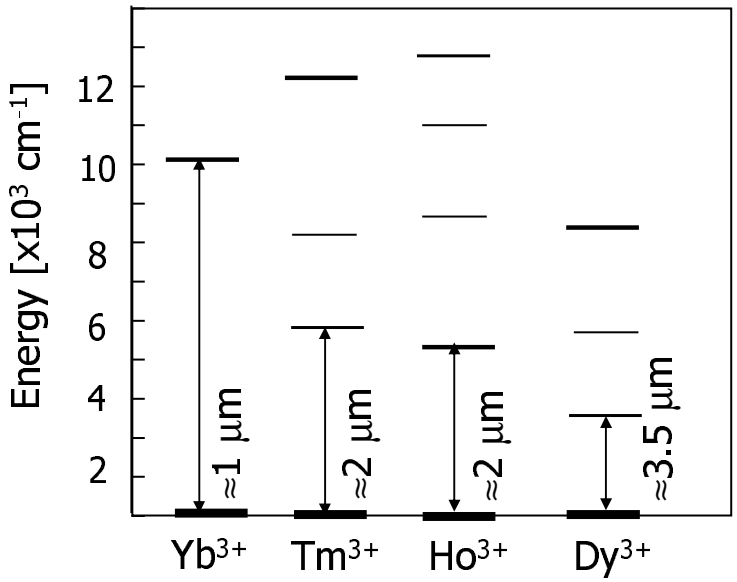

Figure 2.3: Rare-earth energy level scaling.

ZBLANP has a relatively low maximum phonon energy, $\hbar\omega_{max} = 580\,\mathrm{cm}^{-1}$ [51]. Non-radiative decay in various hosts by multi-phonon emission has been shown to exhibit a simple approximate behavior as described in Chpt. 1. The energy gap law states that the multi-phonon emission rate is inversely proportional to the exponential of energy difference (ΔE) between the initial energy state and energy state below:

$$W_{nr} = W_0 e^{-a\Delta E}. \tag{2.2}$$

Here, W_0 is a phenomenological parameter that depends strongly on host material. The parameter a in Eq. 2.2 is inversely proportional to the characteristic phonon energy in a given material and is thus strongly host-dependent. The symbol ΔE in Eq. 2.2 represents the energy gap of the particular electronic state transition. Figure 2.4 is a logarithmic plot of the non-radiative decay rate as a function of energy gap for a number of different hosts [49, 16]. In this figure, Equation 2.2 has been fit to data

obtained from experiments involving various dopant ions in a given host material. The shaded region is defined by the lowest absorption energy gap (~ 2 μm) and peak of absorption (~ 1.7 μm) for the $^3H_6 \rightarrow ^3 F_4$ transition. For ZBLAN the values of W_0 and a are found to be 1.99x10^5 s^{-1} and 0.0021 cm, respectively [49]. The energy gap in ZBLAN (~ 6000 cm^{-1} at the peak of absorption) therefore corresponds to $W_{nr} = 0.64$ s^{-1} which is significantly less than the radiative rate of ~ 83 s^{-1}. The radiative rate is determined from lifetime measurements as shown in Fig. 2.5. The resultant heating due to non-radiative processes in pure Tm^{3+}:ZBLANP should be small relative to cooling processes. To see this, assume that the average energy removed in the cooling process per absorbed photon is k_BT and the average heating due to non-radiative decay of an excitation per absorbed photon is $\Delta E \approx 0.7$ eV. Given the rates above, the average energy removed from the sample in a given time due to cooling is almost five times greater than the energy deposited as heat as a result of non-radiative decay. Stated another way, cooling efficiency is sensitive to the role non-radiative decay plays in quantum efficiency, but the above rates predict a high quantum efficiency (see discussion below).

Excitations to the $^3H_4$ manifold in Tm^{3+}:ZBLANP have the potential to produce fluorescence cooling. The path $^3H_4 \rightarrow ^3H_5$ is primarily radiative (see Fig. 2.4), while the $^3H_5 \rightarrow ^3F_4$ transition is strongly non-radiative. This non-radiative decay can cause heating that would overwhelm the optical cooling effect. Fortunately, the branching ratio for the $^3F_4 \rightarrow ^3H_5$ transition is 0.03 [16], which indicates that the population of the non-radiative branch should be small. Since the $^3H_4$ manifold lies 6900 cm^{-1} above the $^3F_4$ level, it can be populated via excited-state absorption (ESA) during illumination by the OPO at 1.85 μm $< \lambda <$ 1.97 μm. This was verified by observing fluorescence at ~ 1 μm using a silicon-based video camera. This ESA process is endothermic and should contribute extra cooling if fluorescence efficiency and background absorption are in the acceptable range. At typical pump wavelengths, the absorption cross section for the $^3H_6 \rightarrow ^3F_4$ transition is $\sim 2 \times 10^{-22}$ cm^2 [16]. With a

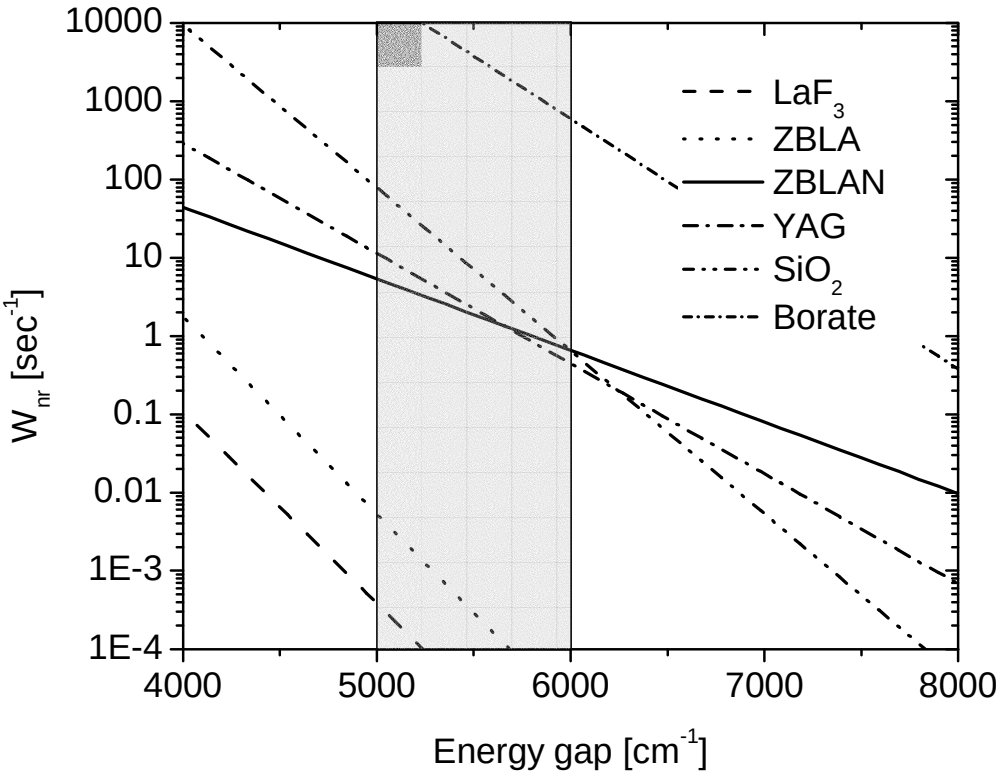

Figure 2.4: Non-radiative decay rates versus energy gap for various host materials after Ref. [49, 16]. The shaded region corresponds to the energy gap for the $^3H_6 \rightarrow {}^3F_4$ transition.

radiative lifetime of 12 ms at a pump wavelength of 1.9 μm, the saturation irradiance is ~ 84 kW/cm^2. Our average irradiance is less than 10% of this value, so we expect the population of the $^3F_4$ manifold to be much larger than that of the $^3H_4$ manifold. Any heating or cooling effects from the ESA process should therefore be small relative to the cooling effects on the $^3H_6 \rightarrow {}^3F_4$ transition. We examine transitions to the $^3H_4$ manifold by directly pumping the $^3H_6 \rightarrow {}^3H_4$ transition using a Ti:sapphire laser at 790-900 nm. The sample showed slight heating. This may indicate the presence of strong fluorescence quenching in addition to the processes described above that led to heating.

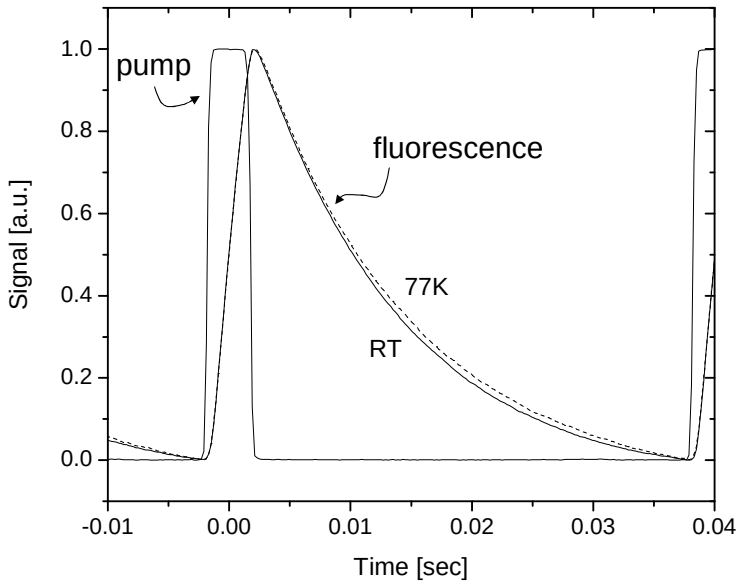

Figure 2.5: Room temperature (solid line) and 77 K (dotted line) radiative lifetimes.

The amount of cooling power possible in a realistic system can be obtained from a simplified rate-equation model for the $^3H_6$ and $^3F_4$ manifolds:

$$\frac{dN}{dt} = \frac{\mathcal{P}^r_{abs}}{h\nu} - W_{rad}N - W_{nr}N + (1-\eta_e)W_{rad}N, \tag{2.3}$$

where N is the number density of excited dopant atoms in the $^3F_4$ manifold, $\mathcal{P}^r_{abs}$ is the resonantly-absorbed power density, $h\nu$ is the pump photon energy, and $W_{rad,nr}$ are the radiative and non-radiative decay rates, respectively.

The last term in Eq. 2.3 describes excitations by fluorescence absorbed in transit through the sample. Due to total internal reflection, a fraction of the fluorescence will be trapped within the host and will effectively decrease cooling efficiency because of re-absorption. This fraction will depend on the relative indices of refraction of the cooling and surrounding materials. The fluorescence that meets the condition for escape is illustrated in Fig. 2.6 as cones originating from a small volume $d\Omega$. Light

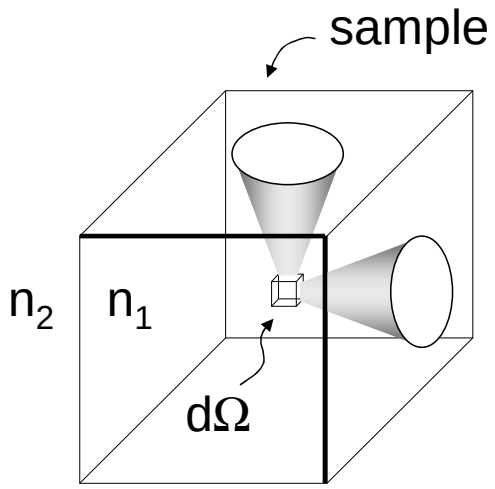

Figure 2.6: Fluorescence escape illustration. The shaded cones correspond to fluorescence from volume $d\Omega$ that satisfies the criterion for escape from cooling material with index of refraction n_1. For clarity, only two of the six cones are illustrated.

emitted from $d\Omega$ outside of the cones is totally internally reflected. The extent of the cones is determined by a given pair of cooling and surrounding material indices (n_1 and n_2, respectively). By integrating over these cones for $n_2 = 1$ the emitted fluorescence power coupled out of the glass as a fraction of the total generated fluorescence power is

$$\eta_e \approx 3[1 - (1 - (1/n_1)^2)^{1/2}] \exp[-\alpha_r(\lambda) l] \tag{2.4}$$

for $n_1 > \sqrt{2}$, where n_1 is the cooling material index of refraction [52]. The exponential factor accounts for fluorescence re-absorption along a characteristic sample dimension l. Equation 2.4 assumes that all totally internally reflected fluorescence is re-absorbed. If $\alpha(\lambda) l \ll 1$ the extraction efficiency is $\eta_e \approx 76\%$ for $n = 1.5$. Estimating an average absorption of ~ 0.1 cm^{-1} for the fluorescence spectrum from Fig. 2.2, this value is further reduced to $\sim$74%. Cooling schemes that use dielectric mirrors

directly deposited on the sample to increase absorbed power as discussed in Chpt. 4 will reduce this value further due to confinement of two of the six fluorescence cones for $d\Omega$ in Fig. 2.6. This effect will depend on the ratio of mirrored facet surface area to total surface area as well as the off-normal incidence reflectivity of the dielectric mirror.

The net laser power density transferred to the sample can be expressed as

$$\mathcal{P}_{net} = \mathcal{P}^{r}_{abs} + \mathcal{P}^{b}_{abs} - \eta_e N_{ss} h\nu_f W_{rad}. \tag{2.5}$$

Here, N_{ss} represents the steady-state number density of excited dopant atoms and $h\nu_f$ is the mean fluorescent photon energy. $\mathcal{P}^{b}_{abs}$ is a nearly wavelength-independent background laser absorption that contributes only to heating. This term corresponds to the background absorption coefficient α_b. The total absorption (α_{total}), which includes α_b, the resonant absorption coefficient $\alpha_r(\nu)$ and any other generalized absorption coefficient (*e.g.* effective absorption due to scattering losses), attenuates the input laser power such that absorbed power is expressed $P^{i}_{abs} = P_{in}(\alpha_i/\alpha_{total})(1 - \exp[-\alpha_{total}L])$. Here P_{in} is the input laser power, L is the physical path length of the beam in the sample, and the index i refers to the particular absorption channel: resonant (r) or background (b).

Combining Eq. 2.3 and Eq. 2.5 we can express the net power transferred to the sample from the laser radiation as the product of absorbed power and cooling efficiency (η_{cool}):

$$\begin{aligned} P_{net} &= P_{abs}\eta_{cool} \\ &= \left[P_{in}(1 - e^{-\alpha_{total}(\nu)L})\right] \left[\frac{\alpha_b + (1-\widetilde{\eta_q})\alpha_r(\nu) - \alpha_r(\nu)\widetilde{\eta_q}\frac{h\nu_f - h\nu}{h\nu}}{\alpha_{total}(\nu)}\right]. \end{aligned} \tag{2.6}$$

A negative net power transferred to the sample in Eq. 2.6 corresponds to cooling. Here $\widetilde{\eta_q}$ is the external quantum efficiency which accounts for the effect of imperfect fluorescence out-coupling:

$$\widetilde{\eta_q} \equiv \frac{\eta_e W_{rad}}{\eta_e W_{rad} + W_{nr}}. \tag{2.7}$$

Since $W_{nr} \approx 0.6\ \mathrm{s}^{-1}$ and $W_{rad} = 83\ \mathrm{s}^{-1}$, we expect an external quantum efficiency of $\sim 99\%$. Equation 2.6 indicates that the cooling power is the product of two factors. The term in the first set of brackets is the total absorbed power and the second term is cooling efficiency. Expressed such that a positive sign corresponds to cooling, the second term of Eq. 2.6 can be written

$$\eta_{cool} = \widetilde{\eta_q} \frac{\lambda}{\lambda_f} \left[1 + \frac{\alpha_b}{\alpha_r(\lambda)} \right]^{-1} - 1. \tag{2.8}$$

In the spectral region $\lambda \approx \lambda_f$ the ratio $\alpha_b/\alpha_r(\lambda) \ll 1$, so according to Eq. 2.8 cooling efficiency should be approximately linear with respect to pump wavelengths in this region. Further, the slope and zero-crossing of a plot of $\eta_{cool}(\lambda)$ are given by $\widetilde{\eta_q}/\lambda_f$ and its inverse, respectively. A measure of quantum efficiency can be made from the pump wavelength at which $\eta_{cool}(\lambda) = 0$ in this linear region. At this point $\lambda \approx \lambda_f/\widetilde{\eta_q}$. Resonant absorption typically approaches zero for $\lambda \gg \lambda_f$, making $\alpha_b/\alpha_r(\lambda) \gg 1$ for finite α_b. In this case Eq. 2.8 becomes large in magnitude and negative in sign, indicating significant heating. The ideal efficiency in Eq. 2.1 is recovered in the limit $\alpha_b = 0$ and $\widetilde{\eta_q} = 1$.

Equation 2.8 gives a lower limit on the external quantum efficiency allowed in the cooling process for a given pump wavelength. Assuming no background absorption, we see that to observe cooling the material must meet the condition

$$\widetilde{\eta_q} > 1 - \frac{k_B T}{h\nu_f} \tag{2.9}$$

if the pump is tuned such that $h\nu_f - h\nu = k_B T$. At room temperature Eq. 2.9 indicates that cooling is achieved for $\widetilde{\eta_q} > 96.3\%$. This also means that the material must have a non-radiative decay rate less than 2.4 s^{-1} given the measured value of $W_{rad} = 83$ s^{-1}. According to Fig. 2.4, the $^3F_4 \rightarrow {}^3H_6$ cooling transition in a fluorozirconate host such as ZBLAN or ZBLANP – indicated by the shaded region in the figure – safely meet this criterion while hosts such as silicates, YAG, or borates do not.

Two approximate expressions are helpful in data analysis, both based on measured temperature change. One follows from Eq. 2.6 and the other from a consideration of thermodynamic factors. In the low pump-depletion limit, such as occurs in a single pass through the sample where $(\alpha_r(\nu) + \alpha_b)L \approx 0.01$, we can express the normalized change in temperature of the sample for small temperature changes as

$$\frac{\Delta T}{P_{in}} \approx \kappa \left[\alpha_b + \alpha_r(\lambda)(1 - \widetilde{\eta_q}) - \alpha_r(\lambda)\widetilde{\eta_q} \frac{\lambda - \lambda_f}{\lambda_f} \right], \tag{2.10}$$

where κ is a constant that depends on experimental factors such as radiative load from the surrounding chamber walls and heat conduction to the sample through the physical supports (*e.g.* glass fibers) and convection from residual gas in the vacuum chamber.

In steady-state, the cooling power expressed in Eq. 2.6 is equal to the external heat load. Assuming negligible conductive and convective loads, the environmental coupling to the sample is radiative. The steady-state cooling power can then be expressed as [36, 53, 54]

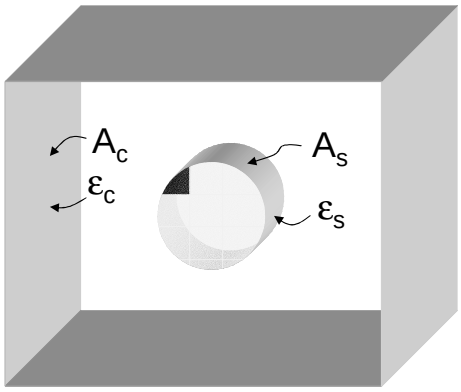

Figure 2.7: Illustration of thermal factors in experimental setup.

$$P_{cool} = P_{load} = \frac{1}{1+\chi}(T_c^4 - T_s^4)\epsilon_s \sigma A_s, \tag{2.11}$$

where $T_{s,c}$ correspond to the temperature of the sample and the surrounding chamber, respectively, ϵ_s is the emissivity of the sample, σ is the Stefan-Boltzmann constant, A_s is sample surface area, and $\chi \equiv (\epsilon_s A_s/\epsilon_c A_c)(1-\epsilon_c)$ is a ratio involving surface areas and emissivities of the sample and chamber. Figure 2.7 illustrates these quantities. Equation 2.11 indicates that well-designed experimental conditions can facilitate low sample temperatures for a given laser cooling power. For example, the sample can be placed in a small chamber with surface area approximately equal to its own ($A_s \approx A_c$), and a low-emissivity coating can be designed for the chamber walls such that $\epsilon_c/\epsilon_s \ll 1$. For fluorescence around $\lambda_f = 995$ nm in ytterbium-based cooling systems, such commercially available coatings have been shown to reduce radiative load by greater than a factor of ten relative to a blackbody [55]. Because they do not absorb at longer wavelengths (*i.e.* 2 μm) these coatings are not adequate for thulium-based refrigerators. Instead we are developing coatings for gold chamber walls based on long wavelength absorbers PbS, InSb, or InAs. Without special attention to these issues, non-ideal experimental conditions result: $\epsilon_{s,c} \approx 1$ and $A_s/A_c \ll 1$. In this

case, for small temperature changes (*i.e.* $T_s/T_c \approx 1$) Eq. 2.11 can be written

$$P_{cool} = P_{load} \approx 4\sigma A_s T_c^3 \Delta T, \tag{2.12}$$

where ΔT is the temperature difference between the sample and its surrounding chamber walls. Equations 2.10 and 2.12 characterize the single pump-pass cooling experiments described below. The constant κ in Eq. 2.10 can be evaluated under these approximations. Considering only radiative load to the sample and the steady-state condition $P_{net} = P_{cool}$, from Eqs. 2.6 and 2.12 we have

$$\kappa \equiv \frac{L}{4\epsilon_s A_s \sigma T_c^3}. \tag{2.13}$$

Using Eq. 2.11 and assuming negligible heat load to the sample through convective and conductive channels, an estimation of the time constant for reaching steady-state temperature can be made. The derivation is included in Appendix A and the result is stated here for cooling rate $k = 1/\tau$:

$$\Delta T = \frac{P_{abs}\eta_{cool}}{kC}(exp[-t/\tau] - 1), \tag{2.14}$$

with

$$\tau = \frac{c_m \rho V_s (1+\chi)}{4\epsilon_s \sigma A_s T_c^3}. \tag{2.15}$$

In these expressions ρ and V_s are sample density and volume, respectively, and c_m is specific heat.

From Eq. 2.1 and Fig. 2.2, one can see that a proper pump source in the vicinity of $\lambda \approx 2$ μm is necessary to efficiently cool Tm^{3+}:ZBLANP. We now turn to a description of the optical parametric oscillator, a high-power tunable source in this wavelength region.

Chapter 3

Pump source: optical parametric oscillator

3.1 Introduction

This chapter describes the pump system for cooling on the $^3F_4 \rightarrow {}^3H_6$ transition in Tm^{3+}:ZBLANP. The system consists of an optical parametric oscillator (OPO) based on periodically-poled lithium niobate (PPLN) pumped by a cw-modelocked Nd^{3+}:YAG laser. The OPO is tunable between 1.7 μm and 2.05 μm and has demonstrated a maximum signal output power of 8 W and a combined power (signal + idler) of over 12 W – to our knowledge the highest power PPLN-based OPO in any pulsewidth regime. This chapter contains experimental details and interesting results of the OPO, most of which can be found in Ref. [37]. Among these results are the following:

- Output slope efficiency for signal and idler (Fig. 3.4)
- Pump depletion as a function of pump power (Fig. 3.4)

- Temperature tuning (Fig. 3.3)
- Output power as a function of resonated idler loss (Fig. 3.5)
- Effect of intra-cavity frequency-narrowing optics (*e.g.* etalons, prism, silicon window)
- Detailed results and descriptions of autocorrelation measurements are contained in Appendix B

A comprehensive theory of the general OPO can be found in Ref. [56], while the theory of periodically-poled OPO's is described in Ref. [57, 58]. General nonlinear theory leading to an understanding of parametric frequency conversion is contained in Ref. [59]. Theory regarding short-pulse diagnostics, especially second order autocorrelations, is treated in Ref. [60]. In addition, Ref. [61] can be used to understand information related to first order autocorrelations. Lastly, Ref. [62] contains a broad overview and working description of OPO's.

The tunability and remarkable wavelength range available from OPO's have made them attractive sources for a variety of applications. Picosecond OPO's offer a balance between short pulse duration and relatively narrow bandwidth. They also have the potential for large output powers. Contributing to this are factors such as the availability of high power pump sources, low threshold average powers, and long nonlinear interaction lengths in non-critically phasematched schemes. Oscillators based on lithium triborate (LBO) have generated combined output powers (signal + idler) of 5.5 W [63] and 2.4 W [64]. A KTP ($KTiOPO_4$) OPO has generated a combined 2.9 W [65] and a non-tunable critically-phasematched KTA ($KTiOAsO_4$) system has produced a combined 21 W [66].

In recent years, the development of periodically poled nonlinear materials has enhanced the flexibility and performance of OPO's [62]. In the case of much-studied

PPLN, one can access the material's highest effective nonlinearity as well as retain generous flexibility in phase-matching parameters and nonlinear interaction lengths. Both continuous-wave [67, 68] (cw) and picosecond [69] OPO systems based on PPLN have generated multi-Watt output powers. Combined outputs as high as 4.85 W from a PPLN OPO synchronously pumped by a 7.9 W, 70 ps cw mode-locked source have been reported [70].

3.2 Experiment, results, and discussion

Scaling PPLN-based OPO's to high power levels is potentially problematic due to the onset of thermal lensing, thermal phase-mismatching, and the increasing effects of photorefractive damage arising from the large amounts of non-phase-matched visible light generation in the crystal. These can lead to spatial, temporal, and output power instabilities, limiting the practical utility of PPLN-based OPO's at high operating power levels. Described below is the successful operation of a picosecond PPLN OPO at out-coupled power levels greater than 12 W with good output stability, limited only by the stability of the pump source. The OPO is synchronously pumped by a high-power picosecond Nd^{3+}:YAG laser (Coherent Antares) at 1.064 μm and is continuously tunable between 1.7 and 2.84 μm. Up to 7.7 W signal radiation at 1.85 μm and 4.7 W idler radiation at 2.5 μm is simultaneously extracted from 17.7 W average pump power, corresponding to a total external efficiency of 70%. Over a period of one hour the output power is stable to within five percent and is correlated to the stability of the pump laser. This implies that the deleterious effects discussed above are absent even at high powers. We also achieve spectral narrowing of the OPO pulses, resulting in transform-limited performance at multi-Watt power levels. Our results indicate that further power scaling of the PPLN OPO to greater than 12 W should also be attainable, making the device a stable source of high-power,

high-quality picosecond pulses for many applications.

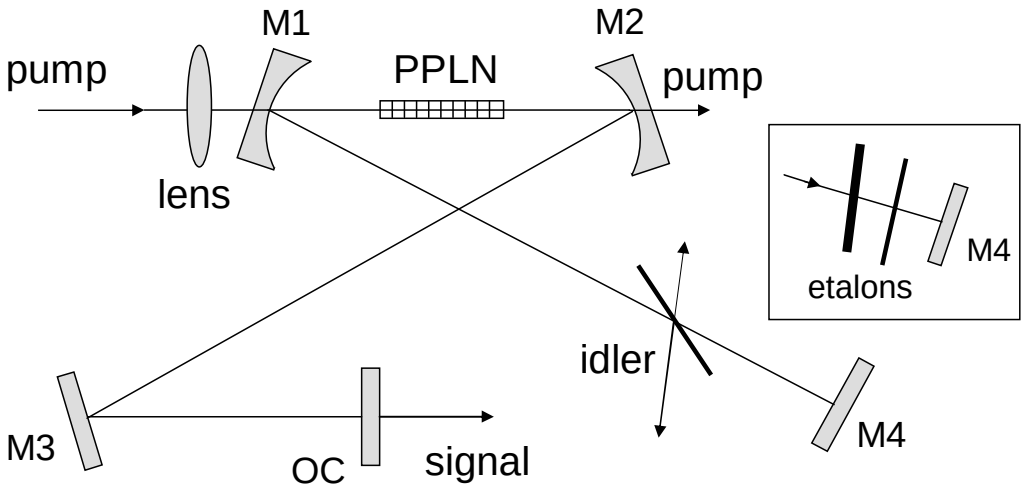

Figure 3.1: Diagram of the asymmetric gamma-cavity OPO. The output coupler (OC) is highly reflecting for the idler and highly transmitting for the signal. All other mirrors are highly reflecting for both signal and idler and highly transmitting for the pump. Fresnel reflections from a transparent window at a finite angle are used to couple idler radiation from the cavity. High power, nearly transform-limited pulses are obtained by replacing the transparent window with two dieletric-coated glass etalons as shown in the inset.

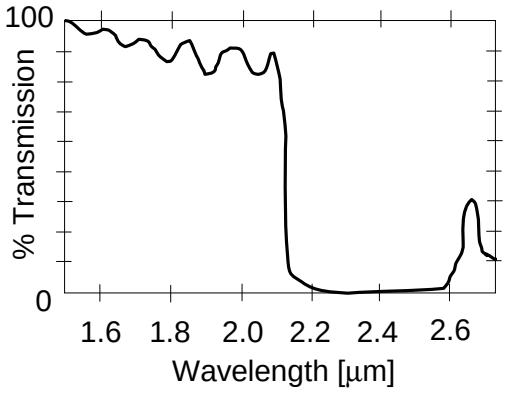

Figure 3.2: OPO output-coupler transmission.

Figure 3.1 shows the asymmetric gamma-cavity configuration of the OPO. The pump source comprises 80 ps (FWHM) cw mode-locked pulses from a Nd^{3+}:YAG laser at a wavelength of 1.064 μm and repetition rate of 76 MHz. Figure B.5 shows a background-free intensity autocorrelation of the pump pulse. The pump is focused into a 47 mm PPLN crystal (Crystal Technology) that contains eight quasi-phasematching periods. The waists of the pump and resonated idler inside the crystal are 37 μm and 66 μm, respectively, corresponding to an optimum overlap parameter of $\xi \approx 2$, where $\xi \equiv L_{crystal}/2z_o$ and $2z_o$ is the confocal parameter [71]. The two curved mirrors (M1 and M2, R=20 cm) are highly reflecting for both the signal and idler and mirror M1 transmits 85.5% of the pump. The planar output coupler (OC) is highly transmitting for the signal and highly reflecting for the idler (T≈98% and 0.1% at 1.85 μm and 2.5 μm, respectively). The transmission of this mirror is critical to OPO optimization and since we are operating near degeneracy it must have a sharp transition between high and low transmission. Figure 3.2 illustrates the transmission cutoff for the OC (Rocky Mountain Instruments). The other planar mirrors (M3 and M4) are highly reflecting for both signal and idler. The length of the cavity is matched to the repetition rate of the pump laser pulse-train. Idler radiation is coupled from the cavity through the Fresnel reflections from an intra-cavity transparent material. This partially reflecting element is placed in the cavity arm opposite that containing the OC so as to avoid loss of the non-resonated signal. Signal and corresponding idler wavelengths are tuned by changing the temperature of the crystal. Tuning data for three of the eight available quasi-phasematching periods (31.2 μm, 31.1 μm and 30.95 μm) is shown in Fig. 3.3, along with the corresponding theoretical curves based on the appropriate Sellmeier equations [72]. The data corresponds to a single set of mirrors.

Since the OPO is operating at high powers near degeneracy (2.128 μm), an expected large signal bandwidth is observed [73]. With 16.9 W pump incident on the crystal, three polished silicon substrates are placed in the cavity arm containing M4

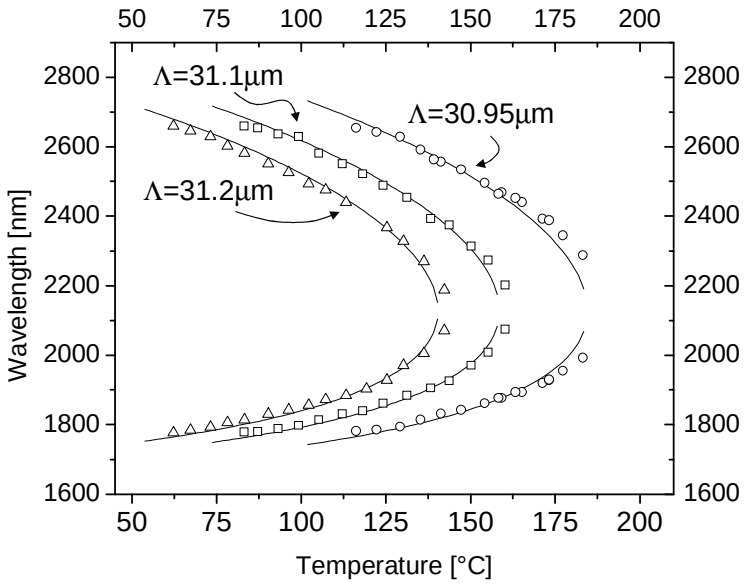

Figure 3.3: Tuning curves for three quasi-phasematching periods of the 47 mm PPLN crystal for a single set of mirrors. Triangles, squares, and circles correspond to periods of 31.2 μm, 31.1 μm, and 30.95 μm, respectively. Solid lines indicate corresponding theoretical tuning curves.

with their normals at an angle of 38 degrees with respect to the propagation direction of the resonated idler. Together these substrates serve as both an idler loss mechanism and frequency-stabilizing etalons. Under these conditions we extract 4.3 W idler from reflections, 5.3 W signal from the output coupler, and the bandwidth of the signal radiation is reduced from a maximum tens of nanometers at highest powers to within the limitations of our current spectrometer ($\sim$1 nm). Replacing the silicon substrates with two dielectric-coated glass etalons (0.5 mm and 0.25 mm thickness) with their normals at small angles with respect to the cavity beam and each other also significantly reduces the signal bandwidth. We obtain 6.5 W of signal light at 1.87 μm from the OC at a pump power of 16.4 W – a loss of 9% compared to the case of no intracavity elements. First and second order autocorrelations of this signal radiation yield a time-bandwidth product of $\Delta\tau_{FWHM} \cdot \Delta\nu_{\mathrm{FWHM}} = 72$ ps$\cdot$6.6 GHz $= 0.48$.

See Appendix B for a full description of autocorrelation results.

Another technique to decrease bandwidth is the insertion of an intracavity prism at approximately Brewster's angle into the arm containing M4. Together with a subsequent planar mirror with reflectance characteristics identical to those of M3 and M4, the prism acts analogous to an intracavity grating [73]. In this case, autocorrelation measurements reveal a full width half-maximum bandwidth of 0.1 nm. A time-bandwidth product of 0.7 follows from a second-order autocorrelation yielding $\Delta\tau_{FWHM}$=72 ps. Signal output powers of 4W were obtained with this spectral profile. (See Fig. B.6(b) and Fig. B.3 for first- and second-order autocorrelations, respectively.) Signal pulsewidths are approximately 77 ps (FWHM) at highest powers without any frequency-selecting elements in the cavity. In this case the spectrum is wide (tens of nanometers) and unstable due to the proximity to degeneracy (2.128 μm) and the imperfect transmission cutoff of the output coupler. With high pump powers and no intracavity elements many frequencies find high gain and may meet the threshold condition for oscillation. However, the pulsed nature and repetition rate of the signal output is unchanged because the OPO cavity is synchronously pumped. The bandwidth characteristics of the signal for various intracavity elements are shown in Table 3.1.

Table 3.1: OPO temporal and frequency characteristics for signal pulses

Intracavity element	Output power [W]	$\Delta\lambda$ [nm]	$\Delta\tau\Delta\nu$
Two etalons	6.5	0.07	0.48
Prism	1.1	0.1	0.73
None	1.6	30	–
None	7.4	55	–

Figure 3.4 shows the average output idler, signal, and total powers as a function of pump power before the crystal for the case of optimum coupling for the idler.

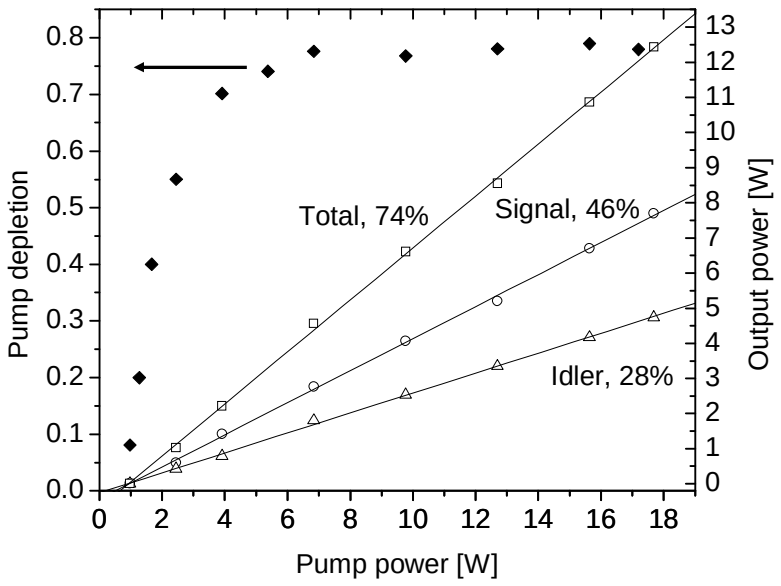

Figure 3.4: Pump depletion and output powers as a function of average input pump power before the crystal for the case of optimum intra-cavity loss for the idler. Open triangles indicate the idler, open circles the signal, and open squares the total extracted power. Slope efficiencies of these three are 28%, 46%, and 74%, respectively. Solid diamonds indicate pump depletion.

Threshold is at 980 mW and output slope efficiencies for the idler, signal, and total powers are 28%, 46%, and 74%, respectively. The slope efficiency remains linear even at pump powers 18 times above threshold, which implies further scaling is possible. Both threshold and slope efficiency are changed with the introduction of loss for the idler. The optimum loss for maximum extracted total power ($\sim$60%) can be figured from the data in Fig. 3.5, which shows total signal and idler output powers as a function of intra-cavity loss associated with the Fresnel reflections of a thin glass window. Pump depletion (Fig. 3.4) is approximately 80% at this optimum. The bandwidth is decreased by approximately a factor of five when large losses are introduced for the idler. The highest loss is obtained using only a glass wedge in place of M4. For the case of no intra-cavity loss (*i.e.* window at Brewster's angle and low cavity losses) we extract 8.0 W average power from the output coupler at a

signal wavelength of 1.85 μm and 17.7 W pump power.

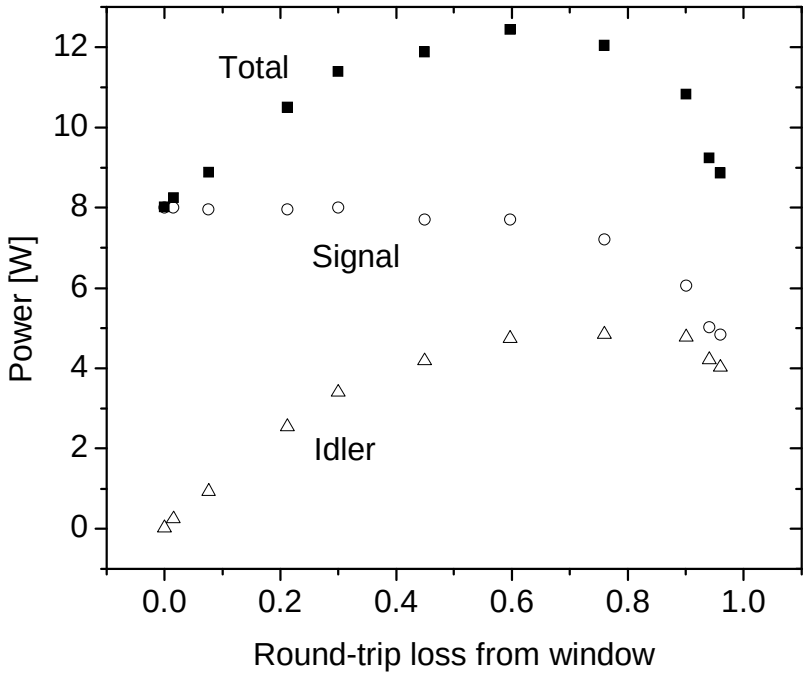

Figure 3.5: Output powers as a function of round-trip intra-cavity loss for the idler due to the insertion of a glass window in the arm containing M4 (see Fig. 3.1). The circles indicate signal power extracted from the output coupler, triangles indicate total idler power extracted from the glass window, and filled squares indicate total extracted power. The highest loss is obtained using only a glass wedge in place of M4.

An acceptable bandwidth for cooling on the $^3F_4 \rightarrow {}^3H_6$ transition in Tm^{3+}:ZBLANP corresponds to $\sim k_B T$. This thermal energy is approximately 75 nm at room temperature and 25 nm at 100 K. Because of this, cooling should be possible even at highest output powers ($\sim$ 8 W) where the bandwidth is on the order of tens of nanometers. The radiative lifetime of the excited manifold ($^3F_4$) is 12 ms and the thermalization time of the Stark levels within the manifold due to electron-phonon interaction is of order sub-picosecond to picosecond at low temperatures (see Chpt. 1). Because the OPO pulses are 80 ps with a repetition period of $\sim$ 13 ns, the atoms thermalize

quickly with respect to the pulse duration and radiatively decay slowly with respect to pulse repetition. Therefore the pump beam is effectively continuous wave from the perspective of the cooling process.

This chapter has outlined the setup and results from the OPO pump system. Due to the high damage threshold, high gain and long length of the PPLN crystal, the high pump source ($\sim$ 25 W) leads to high output powers. The stability and tunability of the OPO can be used for both precision wavelength studies of cooling as well as high absorbed power studies leading to low temperatures. We now turn to a discussion of these studies.

Chapter 4

Cooling experiments

4.1 Introduction

This chapter reports the results of cooling various Tm^{3+}:ZBLANP samples. We first observed anti-Stokes fluorescence cooling in this material in 2000 [27]. In this experiment the sample rested on glass slides inside a small vacuum chamber. The pump passed through the sample once and a maximum steady-state temperature change of -1.2 K from room temperature (RT) was recorded by a thermal camera. Since that time a number of improvements have been made to the system, notably a higher pump power (see Chpt. 3), a successful configuration for multiple pump passes, and a non-contact temperature measurement system with a large dynamic range. As a result of these improvements, a Brewster-cut sample has been cooled -24 K from RT. Another larger Brewster-cut sample is cooled -19 K from RT – this corresponds to ~ 2.2 W of absorbed power and a cooling power of ~ 73 mW. This cooling power (heat lift) is almost a factor of three greater than the highest published optical cooling power of 25 mW [23]. The results, fitting and discussion presented below characterize cooling behavior and include:

- Cooling 1 and 2 wt. % samples in single-pass configurations, resulting in precision fits that yield material parameters such as quantum efficiency (Fig. 4.7 and Table 4.3)
- Experimental and calculated cooling efficiencies (Fig. 4.10 and Table 4.3)
- Comparison between Yb^{3+}- and Tm^{3+}-based coolers (Fig. 4.11 and Table 4.4)
- Interferometric temperature measurement (Fig. 4.3)
- A simple model for multiple-pass configurations and numerical simulations illustrating effects of mirrored and Brewster-cut samples (Fig. 4.18)
- Cooling two Brewster-cut samples in multiple-pass arrangements (Fig. 4.20)
- Results of heating in mirrored sample (Fig. 4.15)

4.2 Experiment

4.2.1 General description

A number of Tm^{3+}-doped glasses and crystals (CaF_2, BaF_2, YAlO, LuAG, ZBLANP) were studied and only certain Tm^{3+}:ZBLANP samples exhibit a net cooling effect. The cause of heating in other samples is primarily due to impurities in combination with various effective phonon energies that impact non-radiative decay rates as discussed in Chapters 1 and 2. Fluorescence quenching and parasitic absorption due to uncontrolled transition metals (*e.g.* Fe^{2+} or Cu^{2+}) and other rare-earths can lead to net heat generation in the sample. See Table 4.5(a) for a description of cooled samples. In a cooling experiment the pump beam is focused into the sample, which rests on glass supports (microscope cover slips or fibers) that contact relatively small surface area and are transparent to the fluorescence (*e.g.* ZBLANP fibers). The

sample is placed in a vacuum chamber held at $\sim 10^{-5}$ Torr. For experiments using a thermal camera for temperature measurement, an identical reference sample is placed in the chamber on separate supports out of the beam path.

Samples are cooled in both single- and multiple-pass configurations for the pump beam. The former allows us to make high-resolution and precise measurements of sample temperature change with various pump wavelengths, while the latter increases absorbed power. (The effect of increased absorbed power can be seen in the first bracketed factor of cooling power in Eq. 2.6.) For small temperature changes as occurs in the single-pass scenario, we record the net temperature change of the sample relative to the reference sample using a pyroelectric (ISI Group) or microbolometer-based (Raytheon) thermal camera. The samples are observed through a thermally-transparent window (*e.g.* CaF_2 or NaCl) in the chamber after the sample reaches a steady-state with its surroundings inside the vacuum chamber. The single pass setup is illustrated in Fig. 4.1.

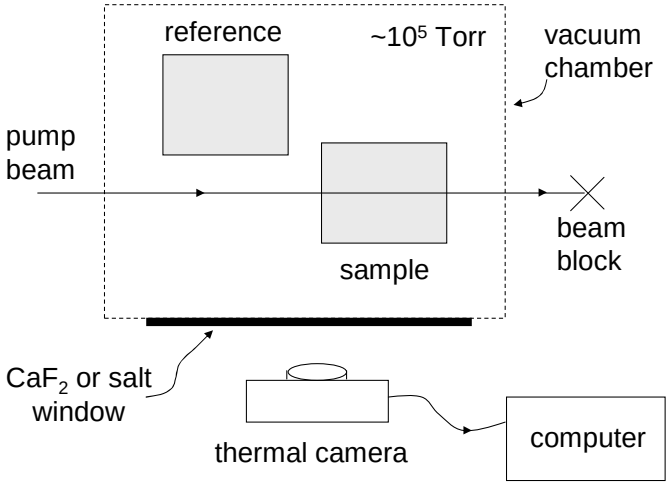

Figure 4.1: Single pass cooling arrangement.

In the multiple-pass experimental configuration as illustrated in Fig. 4.2, the sample is placed on glass supports between two dielectric mirrors of high reflectance

($\sim$ 99.9%) for the pump beam. The beam passes through a small hole of diameter $\sim$0.4 mm in the dielectric coating of a planar mirror. After the first pass through the sample the pump beam is reflected from a second dielectric mirror with a radius of curvature and back into the sample. The mirrors are optimized such that the beam slightly misses the hole in the first mirror resulting in multiple passes.

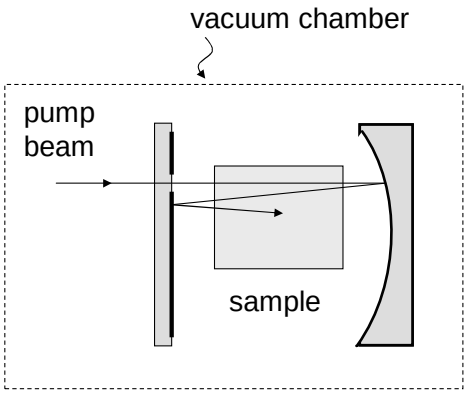

Figure 4.2: Cavity arrangement for multiple passes.

4.2.2 Non-contact temperature measurement

Thermal camera

The thermal cameras are calibrated by controlling the temperature of a ZBLANP glass sample: a digitized image yields an average 8-bit value that corresponds to the temperature of the sample as read by a reference thermocouple. The attenuation of blackbody emission varies with window material, resulting in correspondingly different calibrations. Specific calibrations for the Raytheon micro-bolometer camera are found in Table 4.1. For each window material the calibration is listed in terms of an 8-bit pixel value (0-255) difference with respect to an identical reference sample kept at RT for a degree (Celsius or Kelvin) temperature change. Also included in

the table is the maximum statistical error in percentage of pixel value found in the calibration experiment, obtained by taking five identical images and recording the standard deviation of the pixel value over identical image areas on both the sample and reference. There is a related error associated with the slope of the line fitted to the data in the calibration experiment, the maximum of which is also listed in the table.

Table 4.1: Micro-bolometer camera calibrations

Window	calibration [pixel value/K]	statistical error [%]	slope error
None	25.3	3	0.7
Salt	21.7	3	0.7
CaF_2, 3 mm	12.6	3	0.7

Interferometer

Based on the errors listed in Table 4.1 and similar errors for the pyroelectric camera (ISI group), the thermal cameras have a resolution of 0.2 K in the range $\Delta T \approx \pm 10$ K from room temperature. This range changes with window material. To measure larger temperature changes in multiple-pass schemes we instead use a calibrated Mach-Zehnder interferometer (MZ). This technique is possible because the optical path length of the sample changes with temperature linearly over a wide range [74, 75]. A diagram of the interferometer is shown in Fig. 4.3.

The difference in optical path length between the two arms is defined as $\mathcal{L} = nL - L$ with sample length L and refractive index n. The pathlengths through the sample and vacuum are nL and L, respectively. We can then describe the change in path length difference with respect to sample temperature as :

$$\frac{d\mathcal{L}}{dT} = L\left[\frac{dn}{dT} + \beta(n-1)\right]. \tag{4.1}$$

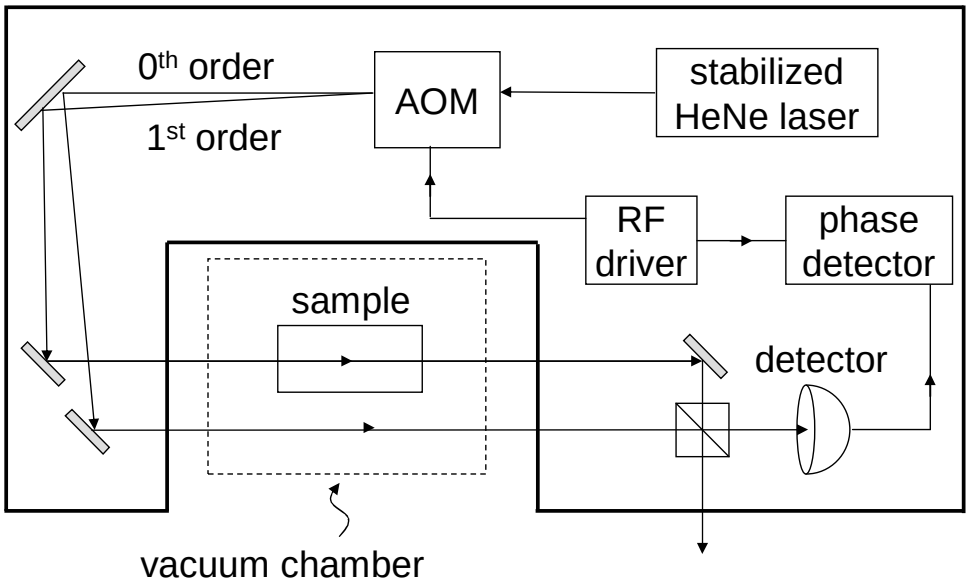

Figure 4.3: Diagram of the calibrated Mach-Zehnder heterodyne interferometer used for non-contact temperature measurement. The phase of the 40 MHz beat signal at the detector changes as the sample temperature changes. The interferometer is placed in an enclosure to reduce phase fluctuations from air movement.

Here and below the subscript for sample temperature T_s is omitted. The quantity in brackets describes the material's refractive index change (dn/dT) and the coefficient of thermal expansion $\beta \equiv 1/L \cdot dL/dT$, and is defined as

$$\frac{ds}{dT} \equiv \frac{dn}{dT} + \beta(n-1). \tag{4.2}$$

Previously reported values for ds/dT for ZBLAN are $-5.9\text{x}10^{-6}$ K^{-1} [75] and $-5.8\text{x}10^{-6}$ K$^{-1}\pm 0.4$ [76, 74]. By placing the sample in an optical cryostat (Janis Research) located in the interferometer, we measure ds/dT to be $-6.6\text{x}10^{-6}$ K$^{-1} \pm 0.8$ for Tm^{3+}:ZBLANP. Data for this calibration is shown in Fig. 4.4.

Using Eq. 4.1, one obtains the following expression for temperature change in terms of number of 2π radian phase changes (m fringes), interferometer laser wavelength

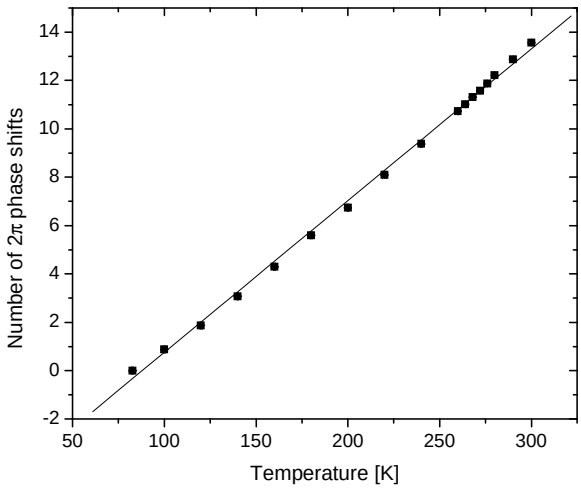

Figure 4.4: Mach-Zehnder calibration data

λ, sample length L and ds/dT:

$$\Delta T = \frac{m\lambda}{L\ (ds/dT)}. \tag{4.3}$$

Heterodyne phase detection schemes can make sensitive measurements of small or rapidly fluctuating phase change [77, 78, 79]. As shown in Fig. 4.3, one arm of the MZ is shifted by 40 MHz using an acousto-optic modulator (AOM). When the two beams interfere on the detector, the phase of the beat signal is monitored with respect to the stable 40 MHz AOM reference signal. Signal processing allows phase information to be retrieved with high accuracy. For this purpose one may use a high-frequency lock-in amplifier that directly displays relative phase. In the experiments described below, the beat signal is analyzed with respect to the reference through a 200 MHz lock-in amplifier (Stanford Research SR844). A computer records the phase change as a function of time via GPIB communications with the amplifier.

Interferometers are sensitive to phase changes within a fraction of 2π. This cor-

responds to a small fraction of a wavelength in optical path length change – on the order of a few nanometers for a helium-neon laser. Systematic and statistical errors in phase information must be carefully monitored and are analyzed in detail in Appendix C. The maximum error assigned to temperatures obtained with this interferometric technique is ± 3 K.

4.3 Single-pass cooling

Overview

The table in Fig. 4.5(a) lists some specific properties of four Tm^{3+}:ZBLANP samples that are discussed below. The accompanying Fig. 4.5(b) shows the geometry of the two cylindrical samples cut such that the angle of incidence of the pump beam is at Brewster's angle. Table 4.2 lists various properties of ZBLANP and ZBLAN and the corresponding sources in the literature. The 1 wt. % cuboid sample (Tm A) is cooled in both single- and multiple-pass schemes. The former results will be compared to cooling in 1 wt. % Yb^{3+}:ZBLANP [21] and are listed in Table 4.4 in Sect. 4.4 below. The 2 wt. % cuboid sample (Tm B) is cooled in a single-pass geometry. A relatively large Brewster-cut sample (Tm C) is cooled in single- and multiple-pass geometries. The former results are used to analyze surface area scaling behavior. A smaller Brewster-cut sample (Tm D) is cooled in a multiple-pass geometry. Multiple-pass results are discussed in Sect. 4.4 below.

Table 4.3 lists the salient results of single-pass cooling for samples Tm A and Tm B. Listed in the table are quantum efficiency ($\widetilde{\eta_q}$) and background absorption (α_b) as determined by fitting Eq. 2.10 to temperature data normalized to incident pump power. Also included in the table are two values for κ (see Eq. 2.10) determined as follows: i) κ_{fit} is obtained directly from the data by fitting Eq. 2.10; ii) κ_{calc} is found from Eq. 2.13. The difference between the two calculations is the use of and assumptions about specific experimental parameters. Specifically, whereas κ in Eq. 2.10 is kept as a fitting parameter that involves thermodynamic quantities, in Eq. 2.12 these quantities are fixed. Values are assigned to such parameters as emissivity, surface area, and ambient temperature, while heat load to the sample through convective or conductive channels is neglected.

Also listed in Table 4.3 is cooling efficiency (η_{cool}) determined from the data in two ways: i) the ratio of cooling power in Eq. 2.12 (Stefan's Law) to absorbed power; ii) the model of Eq. 2.6 using the values for $\widetilde{\eta}_q$ and α_b found in the table. Method i) is based on experimental parameters and small temperature changes. For small absorption, it is written explicitly using Eq. 2.12:

$$\begin{aligned} \eta_{cool,exp} &\equiv \frac{P_{cool}}{P_{abs}} \\ &\approx \frac{4\sigma A_s \Delta T T_c^3}{P_{in}\alpha_r(\lambda)L}. \end{aligned} \tag{4.4}$$

In Eq. 4.4 A_s is sample surface area, ΔT is the change in sample temperature with respect to the chamber temperature (T_c), P_{in} is the incident pump power, $\alpha_r(\lambda)$ in the resonant absorption at the pump wavelength λ, and L is sample length. Method ii) is based on the model of Eq. 2.6, where efficiency is given by the second bracketed term, defined such that a positive sign corresponds to cooling:

$$\eta_{cool,model} = \frac{\alpha_r(\lambda)\widetilde{\eta}_q(\lambda - \lambda_f)/\lambda_f - \alpha_b - (1-\widetilde{\eta}_q)\alpha_r(\lambda)}{\alpha_r(\lambda) + \alpha_b}. \tag{4.5}$$

Sample	Shape	Dim. [mm]	Doping [wt. %]
Tm A	Cuboid	4x4x8	1
Tm B	Cuboid	3x3x10	2
Tm C	Brewster	Dia.=12, L=10.4	1
Tm D	Brewster	Dia.=6.5, L=10	1

(a)

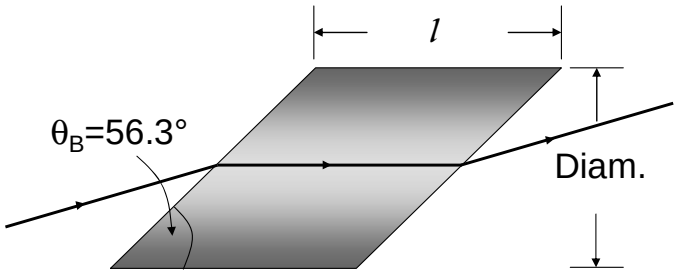

(b)

Figure 4.5: Sample descriptions (a) and geometry of Brewster samples (b).

Table 4.2: Material properties

Property	Units	Value	Material	Source
Refractive index	n	1.49	ZBLANP	[51]
Density	g/cm^2	4.414	ZBLANP	[51]
Glass transition temp.	Celsius	298	ZBLANP	[74]
Crystallization temp.	Celsius	331	ZBLANP	[51]
Thermal expansion	K^{-1}	17.5	ZBLAN	[75]
Temperature coefficient	dn/dT K^{-1}(x10^{-6})	-14.5	ZBLAN	[74]
		-14.45	ZBLAN	[75]
Specific heat	J g^{-1} K^{-1}	0.596	ZBLAN	[42]
Thermal conductivity	W K^{-1} cm^{-1} (x10^{-3})	7.7	ZBLAN	[74]

Results and discussion

Figure 4.6 shows the induced temperature change in sample Tm B versus the pump wavelength for a single pass of the pump beam. Temperature change is normalized to incident pump power. The insets are false color thermal images representing sample cooling (bright) and heating (dark). At a pump wavelength of 1.9 μm and incident average power of ~ 2.72 W, the sample cools to 2 K below room temperature for a single pass of the pump beam. This corresponds to an absorbed power of ~ 120 mW. The heating at wavelengths longer than ~ 1.97 μm can be attributed to parasitic background absorption (α_b) from uncontrolled impurities in the glass such as transition metals. Since absorption in this sample is twice that of Tm A, the approximation leading to Eq. 2.10 must be adjusted. Instead of keeping only first order terms we use the first terms in the expansion of the exponential for absorbed power (*i.e.* first bracketed quantity) in Eq. 2.6. This form of Eq. 2.10 is indicated by the solid line in Fig. 4.6. The sample is found to have an external quantum efficiency $\widetilde{\eta_q} \approx 97.5\%$ and a background absorption $\alpha_b \approx 4 \times 10^{-4}$ cm^{-1}.

The proportionality constant κ in Eqs. 2.10 and 2.13 can be used to evaluate the fidelity of our model. The fit of Eq. 2.10 to the data in Fig. 4.6 finds $\kappa_{fit} = 1002$ cmK/W and the value from Eq. 2.13 is $\kappa_{calc} = 1224$ cmK/W, which is an 18% difference. These values are listed in Table 4.3. The calculated and fitted values agree to within 3% when experimental error is considered, which is satisfactory under the given assumptions.

Figure 4.7 shows the induced temperature change of sample Tm A (solid squares) versus the pump wavelength for a single pass of the pump beam. The single-pass cooling data for sample Tm B from Fig. 4.6 is also shown in the figure for comparison (open triangles). Temperature change is normalized to incident pump power. For sample Tm A, at a pump wavelength of 1.9 μm and incident average power

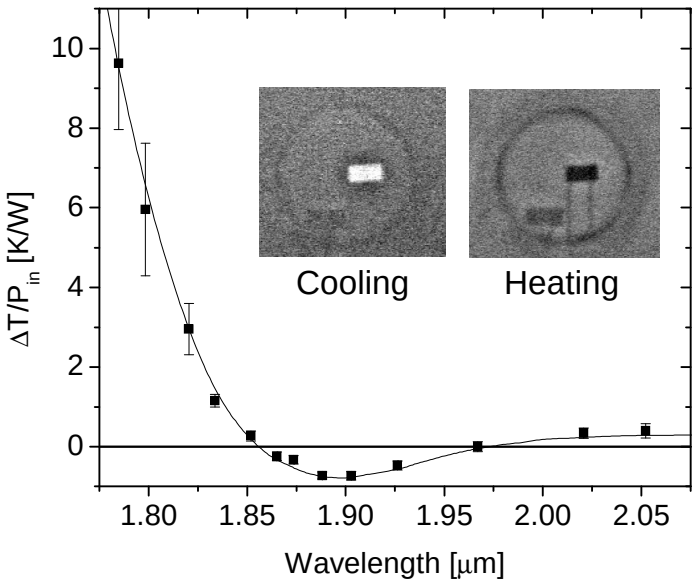

Figure 4.6: Temperature change normalized to incident power versus pump wavelength for a 2 wt.% Tm^{3+}:ZBLANP sample. The solid line is a theoretical fit using Eq. (2.10) with $\lambda_f = 1.803$ μm, $\alpha_b = 0.0004$ cm^{-1} and $\widetilde{\eta_q} = 97.5\%$ The insets are thermal images corresponding to different pump wavelengths. Bright color indicates cooling and dark indicates heating.

of $\sim$ 2.5 W, the sample cools to 1.3 K below room temperature for a single pass of the pump beam. This corresponds to an absorbed power of $\sim$ 48 mW. The heating at wavelengths longer than $\sim$ 1.97 μm can be attributed to parasitic background absorption (α_b). The solid line is a fit of Eq. 2.10 and finds $\widetilde{\eta_q} = 99\%$ and a background absorption of $\alpha_b = 2 \times 10^{-4}$ cm^{-1} for this sample. Also from the fit, $\kappa_{fit} = 591$ cmK/W is 28% below the calculated value $\kappa_{calc} = 825$ cmK/W. The calculated and fitted values agree to within 8% when experimental error is considered, which is satisfactory under the given assumptions.

As shown in Fig. 4.7, a significant difference between the data of the two samples is the pump wavelength at which the sample temperature change is zero ($\Delta T = 0$) in the vicinity of the mean fluorescent wavelength ($\lambda_f = 1.803$ μm). As discussed

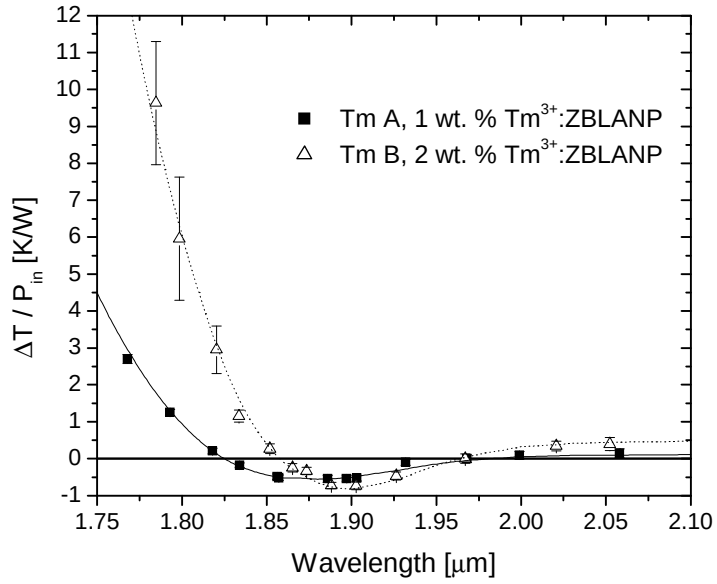

Figure 4.7: Temperature change, normalized to incident power, versus pump wavelength for the 1 and 2 wt.% Tm^{3+}:ZBLANP samples (Tm A and Tm B). The solid and dotted lines are theoretical fits using Eq. (2.10) with $\alpha_b = 0.0002$ cm^{-1} and $\alpha_b = 0.0004$ cm^{-1}, respectively, and $\widetilde{\eta_q} = 0.99$ and $\widetilde{\eta_q} = 0.975$, respectively. Mean fluorescent wavelength is $\lambda_f = 1.803$ μm.

in Chpt. 2 (*c.f.* Eq. 2.8), this yields information primarily about external quantum efficiency. As quantum efficiency deviates from unity, this zero-crossing moves to longer wavelengths with respect to $\lambda_f = 1.804$ μm. Cooling magnitude and cooling efficiency are sensitive to this deviation from unity as can be seen in Fig. 4.8. In this figure the value for $\widetilde{\eta_q}$ is varied in the fit to sample Tm A data in Fig. 4.7, while keeping all other parameters the same, including $\alpha_b = 2 \times 10^{-4}$ cm^{-1}. The figure indicates that the zero crossing is significantly changed even with a change in quantum efficiency from 0.99 to 0.98. Further, no cooling occurs for $\widetilde{\eta_q} \leq 0.95$.

As expected, the cooling process is also sensitive to parasitic absorption. Figure 4.9 shows the fit to sample Tm A cooling data as α_b is varied between its best-fit value of 2×10^{-4} cm^{-1} and 24×10^{-4} cm^{-1} while keeping quantum efficiency

at its best-fit value ($\widetilde{\eta}_q = 0.99$). As indicated in the figure, no cooling occurs for $\alpha_b \geq 12 \times 10^{-4}$ cm^{-1}.

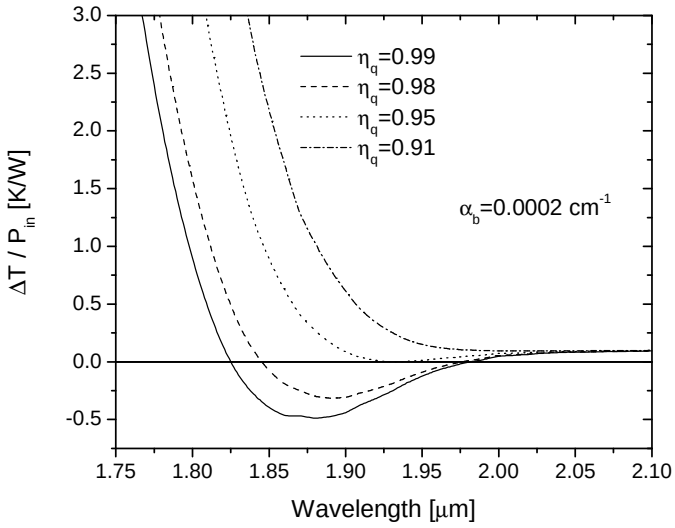

Figure 4.8: Temperature change fit for sample Tm A data varying quantum efficiency. All other fitting parameters are fixed including $\alpha_b = 2 \times 10^{-4}$ cm^{-1}.

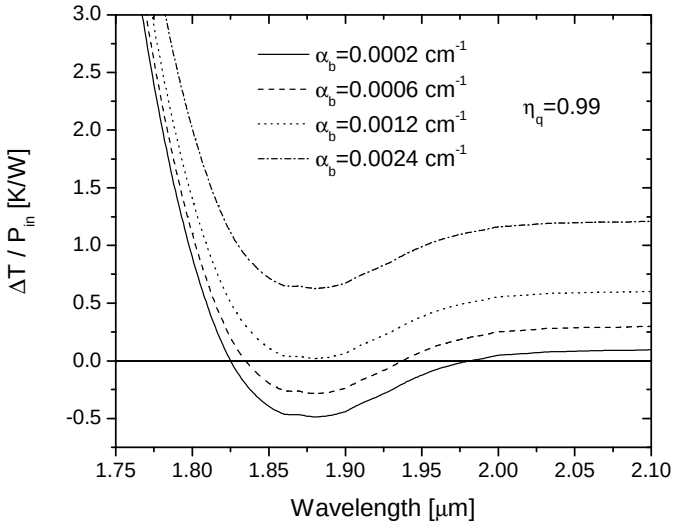

Figure 4.9: Temperature change fit for sample Tm A data varying background absorption. All other fitting parameters are fixed including $\widetilde{\eta}_q = 0.99$.

Table 4.3: Data analysis

Sample	Doping [wt. %]	$\widetilde{\eta_q}$ Eq. 2.10	α_b [cm^{-1}] Eq. 2.10	κ_{fit} [cmK/W] Eq. 2.10	κ_{calc} Eq. 2.13	$\eta_{cool,exp}$ Eq. 4.4	$\eta_{cool,model}$ Eq. 4.5
Tm A	1	0.99	0.0002	590	825	0.028	0.036
Tm B	2	0.975	0.0004	1002	1244	0.013	0.02

Tm^{3+}:ZBLANP sample parameters for the $^3H_6 \rightarrow ^3 F_4$ cooling transition. Quantum efficiency ($\widetilde{\eta_q}$), background absorption (α_b), and κ_{fit} are determined by fitting Eq. 2.10 to temperature data. κ_{calc} is determined from Eq. 2.13. Cooling efficiency is determined experimentally by Eqs. 4.4 (Stefan's Law) and according to the model of 4.5 for a pump wavelength of $\lambda = 1.9$ μm.

Cooling efficiency

Observed cooling efficiencies can be compared to the efficiency predicted by the model of Eq. 2.8. Figure 4.10 shows cooling efficiency ($\eta_{cool} = P_{cool}/P_{abs}$) versus pump wavelength for samples Tm A and Tm B. This data is determined for a given temperature change by Eq. 4.4 assuming unity emissivity for the sample and chamber and neglecting heat load to the sample through conductive or convective channels. The solid squares correspond to the single-pass cooling data of sample Tm A shown in Fig. 4.7. The solid line is the cooling efficiency model given by Eq. 2.8 with $\lambda_f = 1.803$ μm, $\widetilde{\eta_q} = 99\%$, and $\alpha_b/\alpha_r(\lambda) << 1$. The dashed line in Fig. 4.10 is obtained by including the full expression in Eq. 2.8 (*i.e.* the addition of both $\widetilde{\eta_q}$ and α_b). The rapid drop in efficiency with increasing pump wavelength is explained by the diminishing resonant absorption that allows background absorption (α_b) to dominate.

The open squares in Fig. 4.10 correspond to the single-pass cooling data of sample Tm B shown in Fig. 4.6. There is a shifted ordinate-intercept, zero-crossing, and a slightly shifted slope with respect to sample Tm A (solid squares). As discussed above, these shifts offer information about the sample, primarily its external quantum efficiency. We find $\widetilde{\eta_q} \approx 98\%$ for sample Tm B by fitting Eq. 2.8 to the data. This estimate is confirmed by the fit in Eq. 2.10 to the sample's single-pass normalized temperature. Using this fit $\widetilde{\eta_q} \approx 97.5\%$ and $\alpha_b \approx 4 \times 10^{-4}$ cm^{-1}. These values indicate that even though a higher doping concentration increases absorbed power, this may not necessarily improve cooling. It is well known that higher rare-earth concentrations are related to energy-transfer processes that reduce lifetimes and quantum efficiency [16, 80, 81, 82, 83, 84], although McDougall *et al.* claim that doping percentages $\leq 2\%$ in ZBLAN do not effect these quantities. Sample Tm B has a $\sim 10\%$ reduction in extraction efficiency (η_e) with respect to the lower-doping sample due to increased fluorescence re-absorption. Using the same radiative

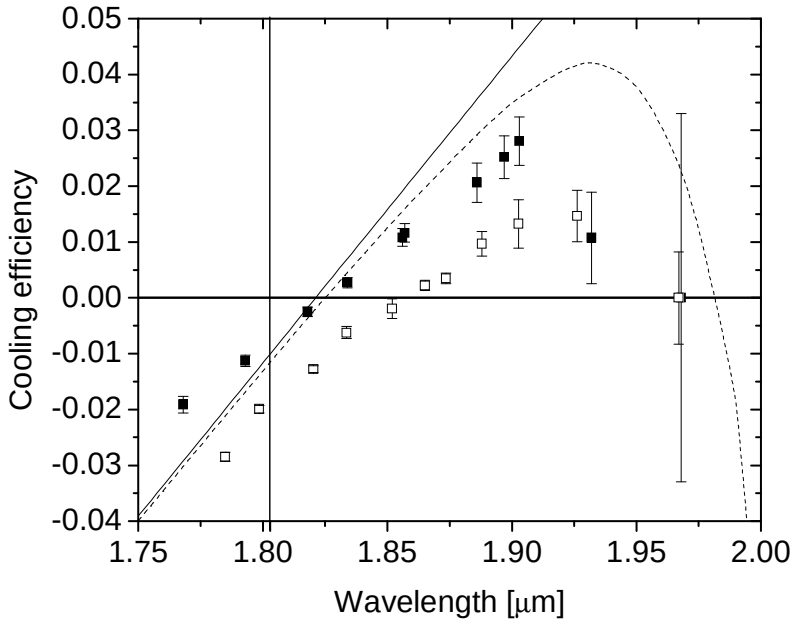

Figure 4.10: Cooling efficiency versus pump wavelength for two Tm^{3+}:ZBLANP samples. The solid squares correspond to single-pass data for sample Tm A and open squares to sample Tm B. The solid lines correspond to ideal cooling efficiency adjusted for non-unity external quantum efficiency and the dashed line also includes background absorption. The vertical line corresponds to the mean fluorescent wavelength.

and non-radiative rates as above, Eq. 2.7 gives $\widetilde{\eta_q} \approx 98.9\%$, which indicates that a decrease in extraction efficiency does not fully account for the observed value of $\widetilde{\eta_q} \approx 97.5\%$. Equation 2.7 suggests that the non-radiative decay rate increases by a factor of greater than 2, assuming the radiative decay rate (W_{rad}) remains constant at 83 s^{-1}.

Equations 4.4 and 4.5 can be used to compare cooling efficiencies in different rare earth solid cooling systems. Figure 4.11 shows cooling efficiency as a function of the pump frequency represented by the ratio of mean fluorescent and pump photon energy difference ($h\nu_f - h\nu$) to thermal energy (k_BT). We compare single-pass cooling data for sample Tm A (filled squares) and ytterbium-doped ZBLANP (open

triangles) [21]. The slope of thulium cooling efficiency is approximately 50% greater than that of ytterbium. At a pump wavelength corresponding to maximum efficiency in both samples (pump energy $\sim 1.3k_BT$ from mean fluorescent wavelength), the figure indicates that thulium cooling is almost twice as efficient. This implies that, under identical conditions, a thulium-doped sample should cool nearly twice as much as a ytterbium-doped sample for a given absorbed pump power. This is expected since cooling efficiency scales as the inverse of dopant energy gap as discussed in Sect. 2.2.

Figure 4.11 directly shows the scale to which these cooling systems are limited by the absorption-related heating effects discussed above. The average difference between mean fluorescent photon energy and pump photon energy is practically limited to $\sim k_BT$ in both systems. As discussed above (*c.f.* Eq. 2.8), finite heat-generating background absorption begins to overwhelm cooling as resonant absorption diminishes at pump energy differences greater than $\sim k_BT$ (*i.e.* long pump wavelengths). Table 4.4 compares cooling efficiency at a pump wavelength corresponding to an energy $\sim 1.3k_BT$ from mean fluorescent wavelength for ZBLANP samples doped with Tm^{3+} and Yb^{3+} ions. Cooling efficiency is determined from Fig. 4.11, as is the slope of the fitted line.

Table 4.4: Rare-earth comparison

Sample	Doping [wt. %]	η_{cool} at $h\Delta\nu \sim 1.3k_BT$	Slope
Tm A	1	3	2.5
Yb	1	1.5	1.75

Comparison of cooling efficiency at a pump wavelength corresponding to an energy $\sim 1.3k_BT$ from mean fluorescent wavelength for ZBLANP samples doped with Tm^{3+} and Yb^{3+} ions. Cooling efficiency is determined from Fig. 4.11, as is the fitted line.

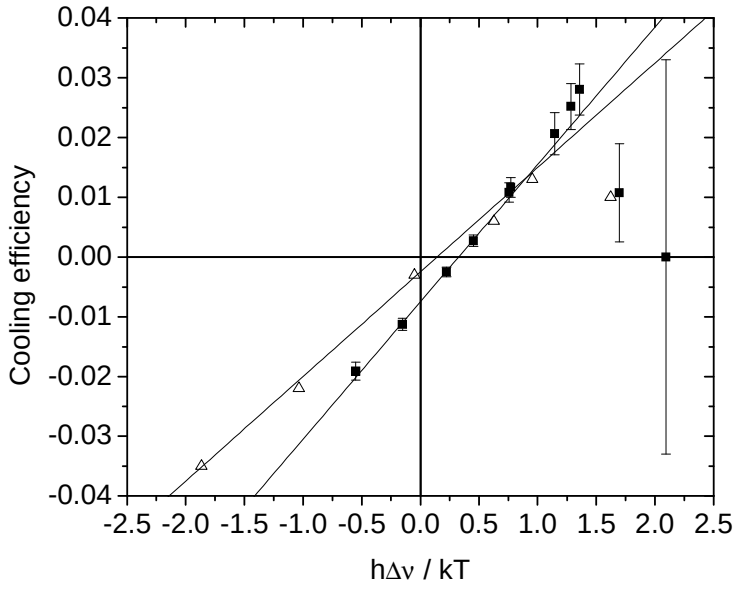

Figure 4.11: Cooling efficiency as a function of the pump frequency. The abscissa is the difference of mean fluorescent and pump photon energies ($\Delta\nu = \nu_f - \nu$) as a fraction of room temperature thermal energy (k_BT). Filled boxes correspond to single-pass data for a 1 wt.% Tm^{3+}:ZBLANP sample and the open triangles correspond to single-pass bulk cooling data obtained by Epstein *et al.* in ytterbium-doped ZBLANP [21]. Slopes are 2.5 and 1.75, respectively.

4.4 Optical refrigerator: multiple-pass cooling

A cryogenic cooler based on anti-Stokes fluorescence requires careful attention to certain practical considerations, including the temperature dependence of cooling efficiency [2, 28, 46, 51]. This factor is an important natural occurrence: for a given pump wavelength in the long-wavelength region of the absorption spectrum, absorption decreases with decreasing temperature due to the decrease in population of the high-lying states in the ground state manifold according to the Maxwell-Boltzman distribution. Behavior relating to this issue will be examined in Chpt. 5. Maximizing the absorbed power seen in the first bracketed factor of Eq. 2.6 is also an important consideration. This is readily addressed through multiple-pass schemes. Heeg *et al.* have studied the possibility of cooling a sample placed inside a laser resonator operating at the appropriate wavelength [43]. Alternatively, one might place the sample in an external resonant cavity (Fabry-Perot) with active stabilization to optimize internal pump power. This idea will be developed in Chpt. 6. Here we consider placing the sample in a non-resonant cavity (NRC) external to the pump source as shown in Figs. 4.12 and 4.13. The former setup is used to cool the cuboid sample Tm A and the latter to cool Brewster-cut samples Tm C and D. The mirrors in Fig. 4.12 are placed close to the sample facets in order to reduce loss by recycling facet reflections back to the sample. This is not necessary for negligible facet reflections in Fig. 4.13, which uses typical mirror separations of 11 cm.

The first bracketed term in Eq. 2.6 increases with multiple pump passes. If P_{in} is the power just to the right of the first mirror in Fig. 4.12, then the absorbed power upon mutliple passes through the sample with total effective absorptivity ($\alpha_{total}(\lambda)$) and length L is

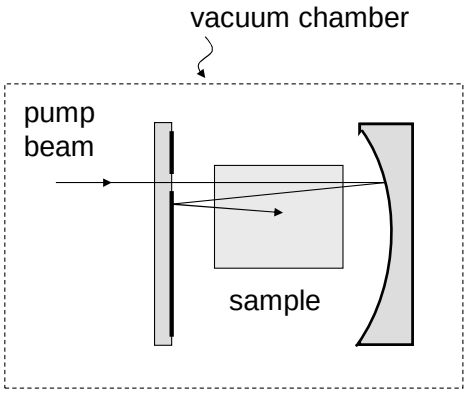

Figure 4.12: Cuboid sample multiple-pass illustration.

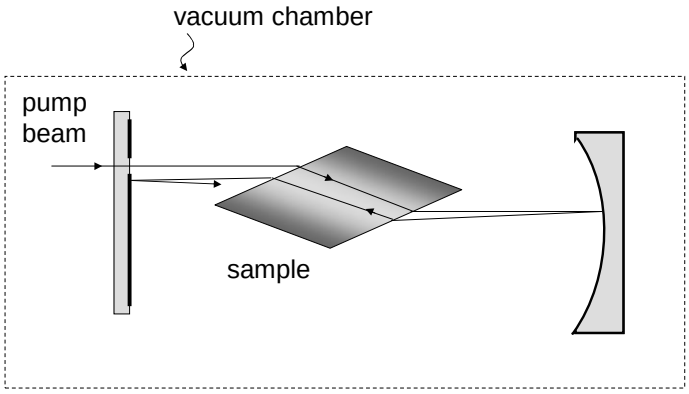

Figure 4.13: Brewster sample multiple-pass illustration.

$$
\begin{aligned}
P_{abs} &= P_{in}(1-e^{-\alpha_{total}(\lambda)L})\left[1+Re^{-\alpha_{total}(\lambda)L}+R^2e^{-2\alpha_{total}(\lambda)L}+\cdots\right] \\
&= P_{in}(1-e^{-\alpha_{total}(\lambda)L})\sum_{j=0}^{N-1}S^j \\
&= P_{in}(1-e^{-\alpha_{total}(\lambda)L})\frac{1-S^N}{1-S}, \qquad (4.6)
\end{aligned}
$$

where N is number of passes, $S = R\exp[-\alpha_{total}L]$, and R is the reflectance of the

confining mirrors at each pass. A simplification for the geometric series was used in Eq. 4.6. The following term now multiplies Eq. 2.6:

$$M = \frac{1 - S^N}{1 - S}, \tag{4.7}$$

and we can express the net power transferred to the sample as

$$P_{net} = M P_{in}(1 - e^{-\alpha_{total}(\lambda)L})\eta_{cool}. \tag{4.8}$$

In Eq. 4.8, P_{net} is negative for cooling (i.e. η_{cool} as defined in Eq. 2.6 is negative). Total absorption includes resonant absorption ($\alpha_r(\lambda)$) and an effective absorption due to scattering losses (α_s), which accounts for the Fresnel reflections from the sample facets, for example. Also included in total absorption is a generalized background absorption that contributes to heating. In Eq. 2.6 and Eq. 2.8, α_b is replaced with the generalized background absorption α_b', which includes both the material's fixed background absorption ($\sim 10^{-4}$ cm^{-1} for experiments above) and any other nearly wavelength-independent heat-generating absorption. This absorption becomes important in samples with mirrors deposited directly on two opposite surfaces. In this case, scattering losses are low and a large number of passes (N) can be achieved. However, absorption in the mirrors that causes heating can be included in the generalized background absorption (α_b') now present in Eq. 2.6 and Eq. 2.8. This can weaken net cooling or even lead to heating.

The factor M in Eq. 4.7 is effectively maximized when mirrors are deposited directly on the sample because of a potentially large number of passes (N), but the potentially large α_b' in Eq. 2.8 can be detrimental. This is avoided in the case of mirrors external to the sample. In this case the effective background absorption is

due to the material alone. However, M is no longer optimized due to finite scattering losses (*e.g.* Fresnel reflections) and the difficulty of maximizing N.

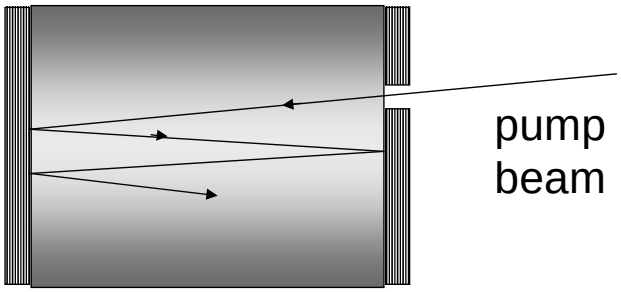

Figure 4.14: Mirrored sample multiple-pass diagram.

Cooling in both of the above multiple-pass schemes is attempted. Highly-reflecting dielectric mirrors (Cascade Optical) are deposited directly on opposite sides of a cylindrical 1 wt.% Tm^{3+}:ZBLANP sample with radius ~ 3 mm and a small entrance aperture for the pump beam is made in one of the mirrors. Such a sample is illustrated in Fig. 4.14, where the thickness of the multi-layer dielectric coating is exaggerated. After coupling the pump into the sample, heating was observed at all pump wavelengths. Because heating magnitude varies with pump wavelength, the character of the data as the pump wavelength is scanned shows evidence of water absorption in the mirrors. Two sets of such data are shown in Fig. 4.15 (filled and open squares). The solid line in the figure is a qualitative fit using Eq. 2.10 with an additional absorption due to water in the mirrors. This absorption, taken from Fig. 5.3(b) after Ref. [85], is contained in the effective total absorption (*i.e.* added to $\alpha_b = 0.0002$ cm^{-1}) distributed across the sample length.

Figure 4.16 displays data from a cooling experiment in which the pump beam passes multiple times through sample Tm A in the NRC arrangement shown in Fig. 4.17. Raw data is recorded as phase change in the Mach-Zehnder interferometer and corresponding temperature change is obtained through the calibration discussed

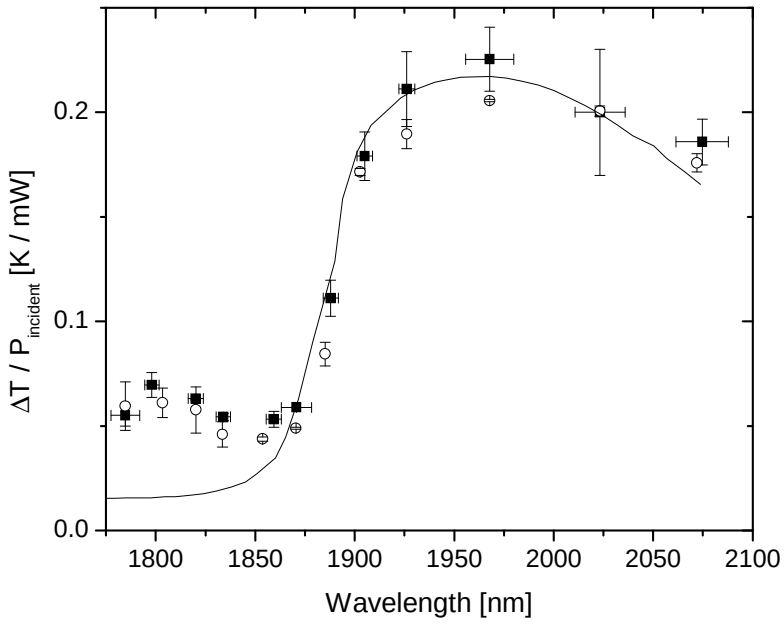

Figure 4.15: Mirrored sample heating with qualitative fit using water absorption.

above. At a time $t \sim 10$ min the pump (power ∼3.5 W and wavelength 1.9 μm) is coupled into the sample. The second curved mirror has a radius of 1 m. The sample cools 19 K below room temperature within 25 min. As discussed in Appendix C, the particular arrangement of the interferometer shown in Fig. 4.17 has an offset in phase change due to the slight difference in path length of the two beams through the second, curved mirror as its temperature increases. The time scale of this offset is small with respect to the time to reach steady-state temperature, allowing the offset to be subtracted. The slight oscillations in the phase change data seen in Fig. 4.16 are also traced to this offset. Both the cold sample and the hot mirror mounts can be seen in the inset of Fig. 4.16, which is a thermal image taken from directly above the experiment. Here bright regions correspond to temperatures cooler than room temperature and dark corresponds to hotter than room temperature.

The cooling experiment shown in Fig. 4.16 suggests the effectiveness of external

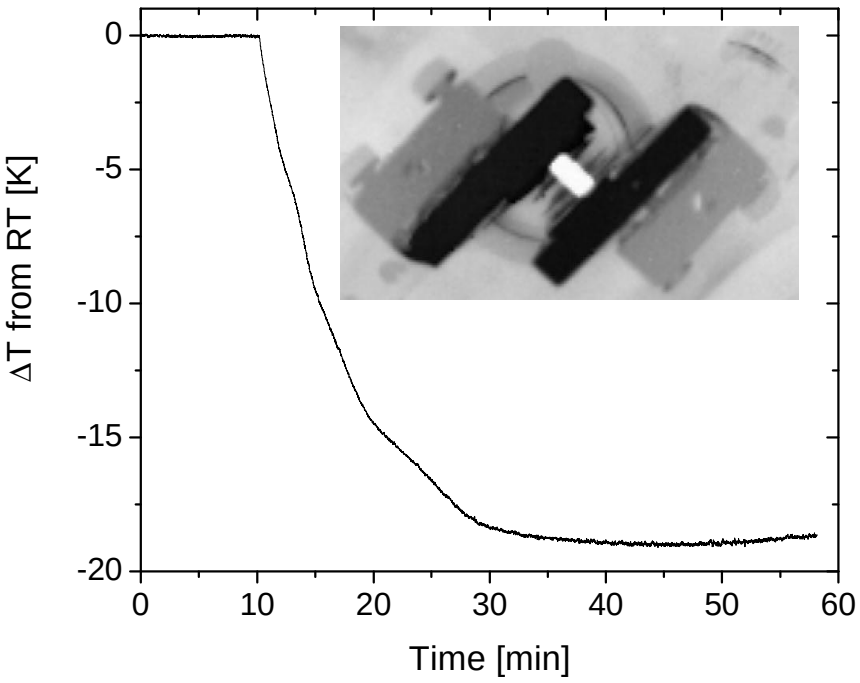

Figure 4.16: Cooling data for multiple pump passes through the Tm^{3+}:ZBLANP sample Tm A. Raw data is recorded as phase change in the Mach-Zehnder interferometer. Both the cold sample and the hot mirror mounts can be seen in the inset, which is a thermal image taken from above the experiment. Bright areas correspond to cooling and dark to heating.

mirrors in a NRC configuration. In this case heating of the sample by direct contact with the mirrors is eliminated but the parameters in Eq. 4.7 are not optimized since the pump beam suffers two $\sim$ 4% Fresnel losses at each pass. Figure 4.18 models cooling power for three different multiple-pass schemes: cuboid sample Tm A with Fresnel losses as in Fig. 4.17, a similar hypothetical sample cut with Brewster-angle faces as in Fig. 4.13, and a similar hypothetical sample with mirrors deposited directly on the surfaces as in Fig. 4.14. The solid line shows cooling power from Eq. 4.8 with the following values: $\alpha_b = 0.0002$ cm^{-1}, $\alpha_r = 0.025$ cm^{-1}, $\widetilde{\eta_q} = 0.99$, and sample length is 0.84 cm. An effective absorptivity associated with 4% loss at two surfaces per pass is added to total absorptivity as α_s as discussed above.

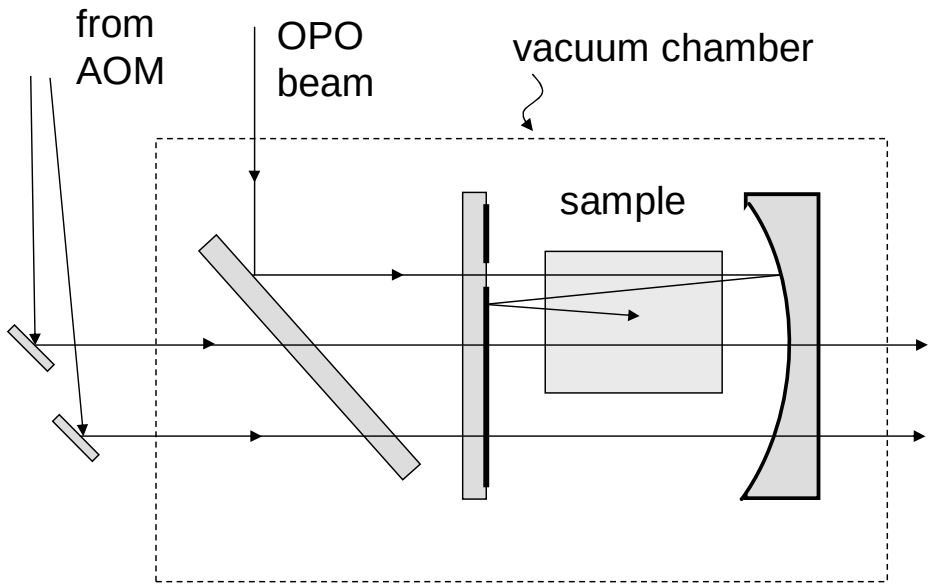

Figure 4.17: Cuboid sample non-resonant cavity arrangement.

The reflectivity of the external mirrors is $R = 99.9\%$, the incident pump power is 4.5 W at $\lambda = 1.9$ μm and $\lambda_f = 1.803$ μm. The dotted line represents cooling power with the same calculation except a loss of 0.5% arbitrarily assigned to the facet losses associated with Brewster-cut surfaces. The dashed line is the same calculation except the mirrors are now deposited directly on the sample. In this case $\alpha_s = 0$ but a background absorption in the mirrors must be arbitrarily assigned for the model and added to $\alpha_b = 0.0002$ cm^{-1}. As discussed above, background absorption becomes α_b' and includes both α_b and effective mirror absorption. If the deposited mirrors have a reflectance of 99.95% and the remaining power directly heats the mirror then each mirror has an optical density (OD) of $(\alpha L)_{mirror} = 0.0005$. The dashed line in the figure represents this OD distributed over the sample length as an effective background absorption.

The values assigned to the case of mirrors deposited directly on the sample in Fig. 4.18 (dashed line) are arbitrary and can realistically be significantly better (*i.e.* less

background absorption in the mirrors). This is illustrated Fig. 4.19, which shows the same model model for cooling power as in Fig. 4.18 as a function of deposited mirror optical density. The dashed and dotted lines represent 20 and 50 passes, respectively.

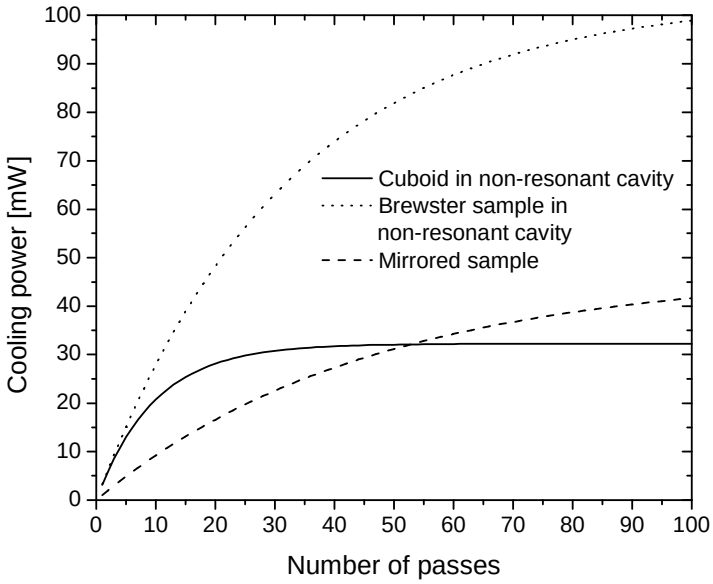

Figure 4.18: Room temperature multiple-pass cooling power modelling for a sample placed in a non-resonant cavity (NRC) and a sample with mirrors deposited directly on its surfaces.

Figure 4.20 displays data corresponding to cooling Brewster-cut samples Tm C and Tm D. The thick and thin lines in the figure indicate temperature changes with respect to RT of samples Tm D and C, respectively. At a time $t \approx 10$ min. the pump is coupled into the sample in the arrangement shown in Fig. 4.21. Pump powers of 4.35 W and 4.5 W are incident on the first facet of the sample for Tm C and Tm D, respectively. For both experiments the curved mirror in Fig. 4.21 has a radius of 20 cm and the cavity length is ~ 11 cm. At a time $t \approx 73$ min. the pump is blocked and the sample warms to room temperature. The data has been scaled according to the known systematic drift in the interferometer as described in Ap. C. Using Eq. 2.12, the cooling power corresponding to the temperature changes of sample Tm

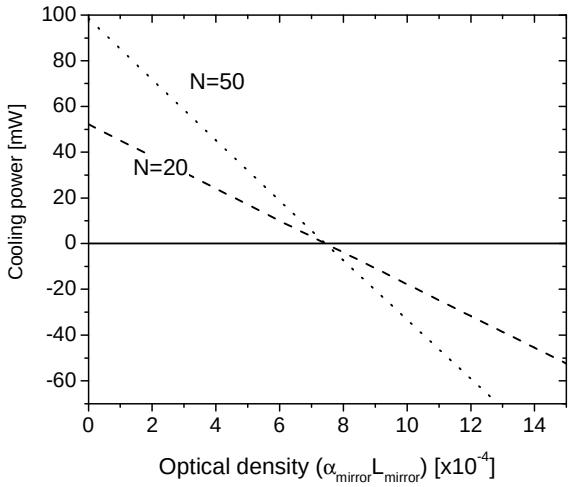

Figure 4.19: Room temperature mirrored sample cooling power modelling.

C and Tm D are 73 mW and 40 mW, respectively. Using Eqs. 2.6 and 2.12, the absorbed powers in sample Tm C and Tm D are 2.23 W and 1.22 W, respectively. Cooling results for these samples are summarized in Table 4.5.

Table 4.5: Brewster-cut sample cooling results

Sample	ΔT from RT [K]	P_{abs} [W]	P_{cool} [mW]	τ_{fit} [s]	τ_{calc}
Tm C	-19	2.23	73	13.8	12
Tm D	-24	1.22	40	9	7.8

Also shown in Fig. 4.20 is the expected temporal behavior of temperature change according to Eq. A.6 as derived in Ap. A. The fitted lines for the data of samples Tm C and D use time constants of $\tau = 13.8$ min. and $\tau = 9$ min., respectively. Using unity emissivity for the sample and chamber, Eq. A.7 of Ap. A yields theoretical time constants for the two samples of $\tau = 12$ min. and $\tau = 7.8$ min., respectively. Although the fitted value for τ is 15% different in each case, if sample emissivity is changed to 0.9 this difference is reduced to 5% in both cases.

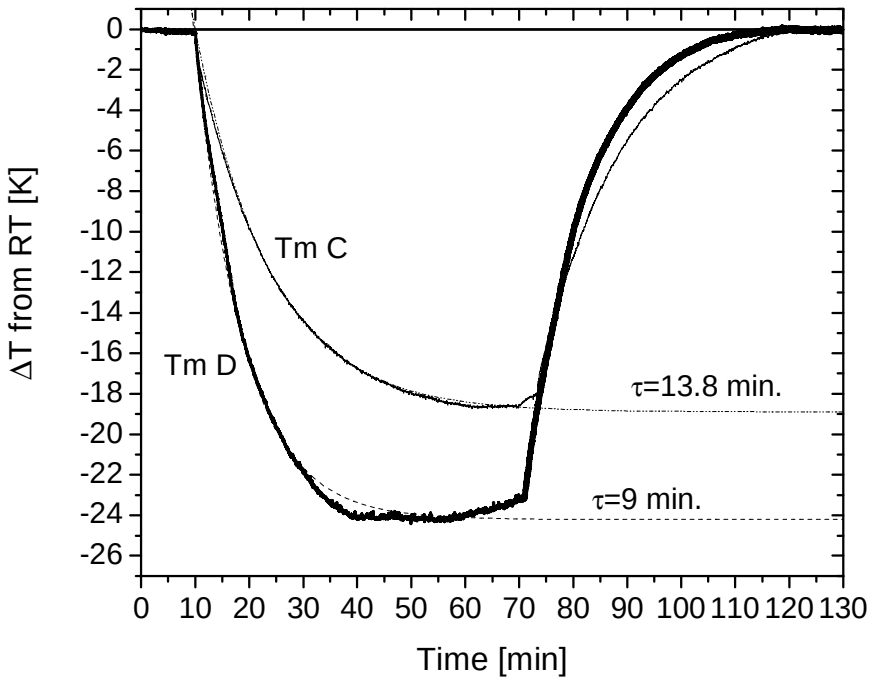

Figure 4.20: Multiple-pass cooling with Brewster-cut samples Tm C and Tm D. The dashed and dotted lines fit temporal behavior of temperature change as described in Ap. A.

Heat load to the sample scales linearly with the sample surface area according to Eq. 2.12. Because of this, a sample with relatively small surface area should reach relatively low temperatures for the same absorbed pump power. Assuming that factors involved in cooling efficiency (*e.g.* α_b and $\widetilde{\eta_q}$) are equivalent, then cooling two samples of surface area $A_{1,2}$ should result in following ratio of their normalized temperature changes:

$$\frac{\Delta T_1/P_{abs,1}}{\Delta T_2/P_{abs,2}} = \frac{A_2}{A_1}. \tag{4.9}$$

In Eq. 4.9, $P_{abs,i}$ is the absorbed power in sample i. An optical fiber is a geometrical limit of this issue and is the reason Gosnell was able to cool a Yb^{3+}-doped ZBLANP

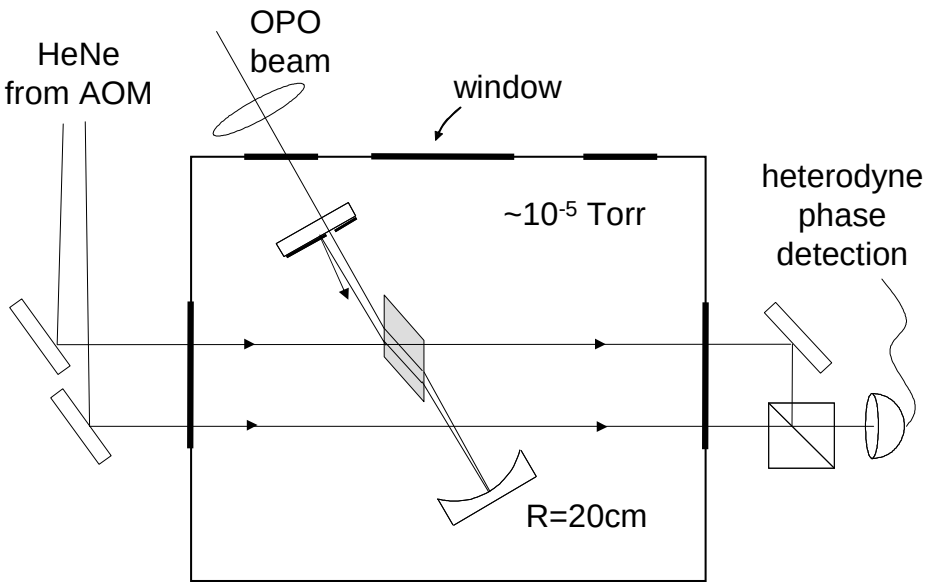

Figure 4.21: Brewster sample non-resonant cavity arrangement.

fiber -65 K from RT [30]. To test this scaling, samples Tm A and Tm C are cooled simultaneously in a single-pass geometry. After normalizing temperature change to absorbed power, the left-hand side of Eq. 4.9 is found to be 2.8, while the right-hand side is 3.7. This disagreement may be explained by the assumption of identical cooling efficiency in sample Tm C for which no detailed spectroscopy has been obtained. If background absorption is decreased by 20% and resonant absorption increased by 20%, for example, Eq. 4.9 would be exactly satisfied.

Another type of scaling is tested using sample Tm A. In the experimental arrangement shown in Fig. 4.17, the sample is cooled under identical conditions while varying the input pump power. Results are shown in Fig. 4.22. Phase change is scaled to temperature change and normalized to incident pump power – data is shown in Fig. 4.22(a). The systematic background drift in phase change is neglected since it results in a reproducible DC offset that scales linearly with pump power. The steady-state normalized temperature change as a function of input power is displayed

in Fig. 4.22(b). The large error bars in the latter figure result from the uncertainty in temperature change as discussed above and a slight uncertainty in DC offset for this particular experimental arrangement.

The results in Fig. 4.22 indicate a nonlinearity in cooling efficiency as a function of input power. There is an expected nonlinearity due to temperature-related manifold populations, and cooling efficiency as a function of temperature is modelled in Chpt. 5. The expected slope of temperature change as a function of temperature for small changes is obtained by fitting a line between points of calculated efficiency in Fig. 5.14 at T=250 and 300 K. This slope is used with the temperature changes corresponding to the data in Fig. 4.22. The result is plotted as the dashed line in Fig. 4.22(b) – this nonlinearity, more severe at lower temperatures, is not enough to explain the nonlinearity of the data in Fig. 4.22. Other explanations could include nonlinear diffraction caused by a higher-order index of refraction in the glass (n_2). This would lead to poor spacial confinement of the pump beam at higher pump powers. Another possibility is nonlinearities associated with excited state absorption on the ${}^3F_4 \rightarrow {}^3H_4$ transition.

The experimental apparatus is tested for systematic nonlinearities that would explain the results shown in Fig. 4.22. Average power is measured before and after the first mirror in the NRC shown in Fig. 4.17 while power is varied. Results are shown in Fig. 4.23. The figure indicates that pump beam pointing is relatively stable and the existence of clipping as the beam passes through the $\sim$ 400 μm diameter hole can be eliminated as a source of the nonlinearity shown in Fig. 4.22.

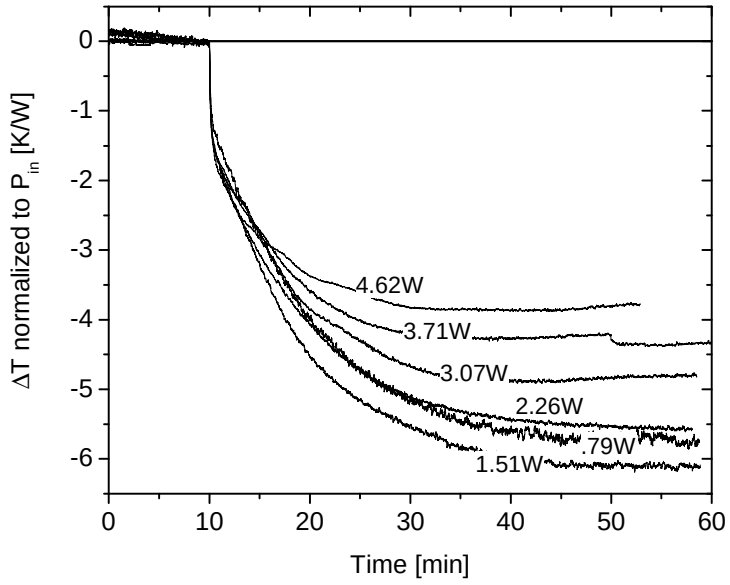

(a)

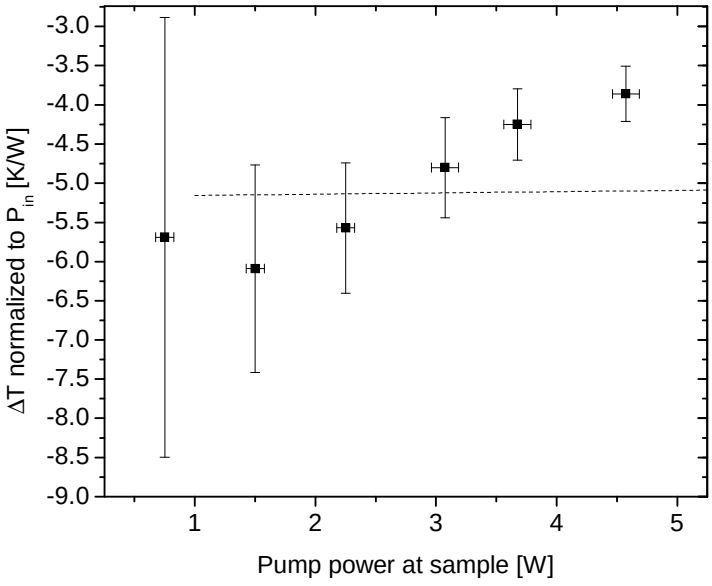

(b)

Figure 4.22: (a) Pump power-normalized phase change scaled to temperature for various pump powers, and (b) steady-state values from the data in (a). The large error bars in (b) are primarily due to the uncertainty in MZ temperature (± 3 K). The dashed line in (b) is the nonlinearity in normalized temperature expected from spectroscopic studies in Chpt. 5.

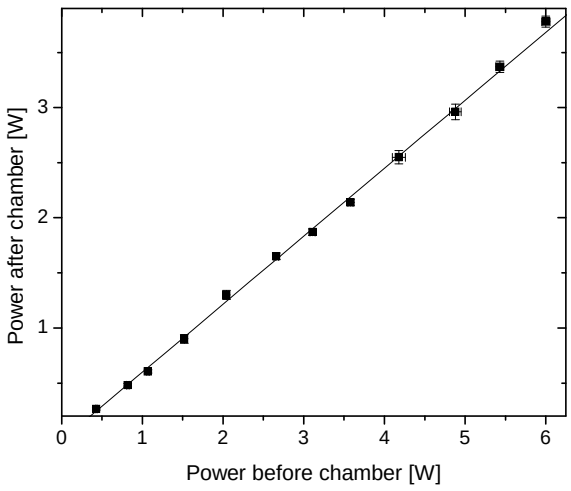

Figure 4.23: Pump beam pointing stability test. Power is measured before and after the NRC in-coupling mirror shown in Fig. 4.17.

Sample chamber

As discussed above in Chpt. 2, attention to certain experimental details can aid the achievement of low temperatures. According to Eq. 2.11, heat load to the sample is greatly reduced if its vacuum chamber has low emissivity and a surface area comparable to that of the sample. For example, assume emissivities of the sample and chamber are $\epsilon_s = 1$ and $\epsilon_c = 0.5$, respectively. If the chamber and sample surface areas are approximately equal ($A_c \approx A_s$), then the factor $1/(1+\chi)$ in Eq. 2.11 is 0.5. (Recall that $\chi \equiv (\epsilon_s A_s/\epsilon_c A_c)(1-\epsilon_c)$.) All other factors being equal (*e.g.* absorbed power) this corresponds to half the radiative heat load to the sample and twice the cooling temperature change relative to scenarios with $A_s/A_c \ll 1$, $\epsilon_{c,s} \approx 1$. A mount is constructed for sample Tm D to test this scaling. As shown in Fig. 4.24, a cylindrical enclosure that holds the Brewster-cut sample sits atop an ~ 1 in. cuboid copper block. A ~ 3 μm thick gold coating is deposited on the inside of the cylindrical region, which is then dipped in a solution of PbS. This coating combination is intended to absorb fluorescence (via PbS), transfer heat to the rest of the mount, and have a low effective emissivity (Au-PbS). Small ZBLANP fibers are inserted into holes inside the cylinder on which the sample rests during cooling experiments. The ends of the cylindrical mount are open since the sample/mount is placed in a NRC as in Fig. 4.21.

Results of cooling sample Tm D in this mount are shown in Fig. 4.25. The top trace shows temperature change relative to RT when the cover is secured over the sample as intended. The bottom trace is an identical experiment with the cover removed. The figure indicates that the coating combination is effectively absorbing fluorescence. However, it appears that the mount has a significant emissivity since cooling magnitude greatly decreases with the cover on, becoming a positive change in temperature with respect to RT at time t $\approx$ 55 min. A cause of this net heating is the poor conductive contact between the mount and the large vacuum chamber

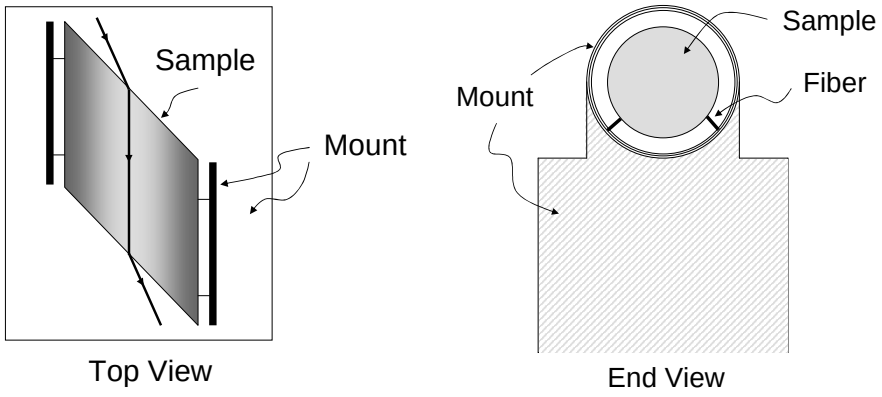

(a) (b)

Figure 4.24: Top (a) and end (b) views of special sample mount. The inside of the cylindrical part of the mount is coated with gold and PbS for absorption of fluorescence and low emissivity.

(sink). Indeed, a straightforward improvement is an effective heat sink to this mount (*e.g.* RT water flowing through the mount).

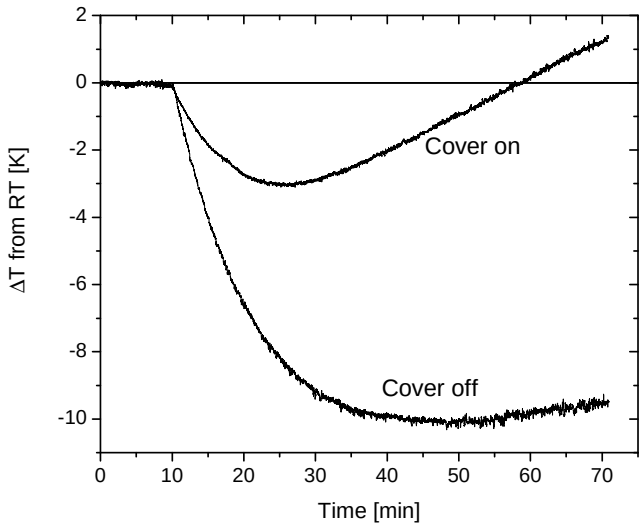

Figure 4.25: Effect of special sample mount on cooling sample Tm D. The mount has a thin coating of PbS on gold.

Monolithic optical maze

Placing a Brewster-cut sample in a NRC for multiple passes is an effective method to increase absorbed power as shown above. Another method makes use of total internal reflection of the pump beam in the sample. As shown in Fig. 4.26, the sample is cut into a cuboid with a small triangular facet in one corner, the normal of which is approximately along the diagonal of the shape. The pump beam is coupled into the sample through this facet at a finite angle with respect to the sample shape's diagonal. Meeting the condition of total internal reflection, the beam is reflected from the opposite corner. The beam is aligned such that the subsequent pass of the beam just misses the facet and is again reflected inside the sample. The dimension of the in-coupling facet is on the order of 100 μm and is determined by the waist of the pump beam, which is optimized such that the Rayleigh range is properly matched to the characteristic dimension of the sample. A sample with dimensions 3.3 x 4.4 x 4.4 mm and an in-coupling facet of side $\sim$ 400 μm is cooled to -7.5 K from RT with an incident pump power of 2.8 W at a wavelength $\lambda = 1.88$ μm. Figure 4.26 shows a diagram of the pump beam coupled into a sample cut in such a manner. Also in the figure is a ~ 1 μm fluorescence image of the pump beam trapped in this manner.

4.5 Error analysis

Error in a quantity $x = f(u, v, \ldots)$ is propagated from constituent fundamental error in $u, v, \ldots$ according to

$$\sigma_x^2 = \sigma_u^2 \left(\frac{\partial x}{\partial u}\right)^2 + \sigma_v^2 \left(\frac{\partial x}{\partial v}\right)^2 + \cdots , \tag{4.10}$$

where each quantity u, v has associated error σ_u, σ_v. Equation 4.10 assumes that there

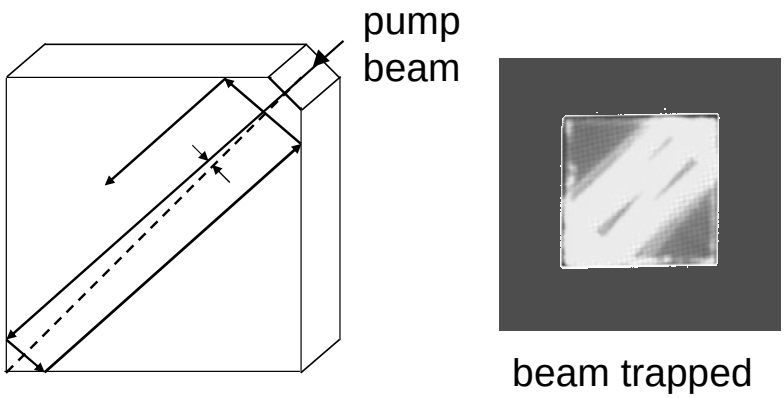

Figure 4.26: Monolithic optical maze for pump beam trapping. The right figure is a near-infrared image of the beam coupled into the sample.

is no correlation between quantities u, v. Uncertainties in this work are calculated according to the equation based on measures of fundamental error. Many of these measures, along with their propagation to other quantities according to Eq. 4.10, are listed in Table 4.6. For example, normalized temperature change for sample Tm B (see Fig. 4.6) has two sources of error: statistical error associated with pump power (P) and both statistical and fitting errors involved in temperature measurement (ΔT) as described in Sec. 4.2.2. According to Eq. 4.10, these fundamental errors are then propagated in normalized temperature change according to

$$\sigma_{\Delta T/P}^2 = \sigma_{\Delta T}^2 \left(\frac{1}{P}\right)^2 + \sigma_P^2 \left(-\frac{\Delta T}{P^2}\right)^2, \tag{4.11}$$

where $\sigma_{\Delta T} = 0.2$ K and σ_P is on the order of 20 mW for a pump power of 2 W.

Quantities in Table 4.6 such as $\widetilde{\eta_q}$ and α_b that are determined from a fit to the data have errors associated with the fitting process. Spectroscopic quantities such as α_r and λ_f have statistical errors associated with the experimental apparatus. However, extensive averaging is used to minimize this error and the primary uncertainty in λ_f

is systematically due to calibration and correction uncertainties. The uncertainty in α_r is determined from a comparison of results from various experiments as illustrated in Fig. 5.5. The errors for κ_{fit} for samples Tm A and Tm B are assessed while fitting Eq. 2.10 to normalized temperature change as described above in Sec. 4.3. The uncertainty in κ_{calc} is obtained using Eq. 4.10. If the errors in $\kappa_{fit,calc}$ for sample Tm A are considered, the fitted value remains different from the calculated by 8%. If the errors in $\kappa_{fit,calc}$ for sample Tm B are considered, the fitted value remains different from the calculated by 3%. Both remaining discrepancies are acceptable because of the assumptions made regarding thermodynamic factors described above.

Methods for determining η_{cool} both directly from temperature change data using Eq. 4.4 (Stefan's law) and the model based on fitted parameters such as $\widetilde{\eta_q}$ (Eq. 4.5) are described above in Sec. 4.3. Uncertainties in η_{cool} for both methods are propagated from fundamental errors according to Eq. 4.10. There is agreement between the two methods within uncertainties. This can be seen in Table 4.6, where the values used in calculations for the uncertainties in η_{cool} (model and experiment) are chosen for $\lambda = 1.903$ μm for samples Tm A and Tm B. This agreement is further illustrated in Fig. 4.27. The data in the figure is the same experimental efficiency (Eq. 4.4) as in Fig. 4.10 for samples Tm A (filled squares) and Tm B (open squares). Error bars are calculated according to Eq. 4.10. Also in Fig. 4.27 is the model efficiency according to Eq. 4.5. This model involves quantities that have fundamental error and this is indicated by the shaded region around the model line for samples Tm A (black region) and Tm B (grey region).

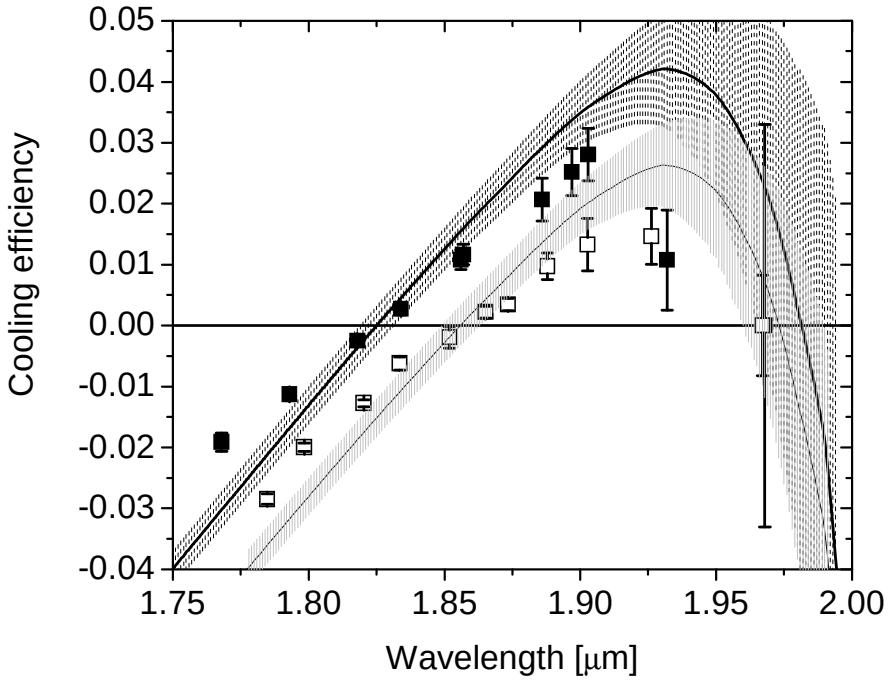

Figure 4.27: Cooling efficiency error. Open squares and grey shaded region correspond to experimental and model efficiencies for sample Tm B, respectively. Filled squares and black shaded region correspond to experimental and model efficiencies for sample Tm A, respectively.

Table 4.6: Error analysis

Quantity	Units	Uncertainty	Typical value	Method
ΔT, Raytheon camera	K	0.2	1.5	statistical, fit
ΔT, ISI camera	K	0.2	1.5	statistical, fit
ΔT, interferometer	K	3	20	statistical, systematic
T_c	K	4	293.15	systematic
$\widetilde{\eta_q}$, Tm A	–	0.0025	0.99	fit
$\widetilde{\eta_q}$, Tm B	–	0.0025	0.975	fit
α_b, Tm A	cm^{-1}	0.0001	0.0002	fit
α_b, Tm B	cm^{-1}	0.0001	0.0004	fit
α_r, Tm A	cm^{-1}	8%	0.025	statistical
α_r, Tm B	cm^{-1}	20%	0.05	statistical, systematic
λ_f	nm	3	1803	statistical, systematic
T_{min}	K	5	150	statistical, systematic
τ_r	ms	0.3	12	statistical
$\widetilde{\eta_q}(T)$	–	0.0005	0.992	Eq. 4.10
κ_{fit}, Tm A	cm K/W	135	591	fit
κ_{calc}, Tm A	cm K/W	34	825	Eq. 4.10
κ_{fit}, Tm B	cm K/W	150	1002	fit
κ_{calc}, Tm B	cm K/W	51	1244	Eq. 4.10
η_{cool}, Tm A experimental	–	0.004	0.028	Eq. 4.10
η_{cool}, Tm A model	–	0.0055	0.036	Eq. 4.10
η_{cool}, Tm B experimental	–	0.004	0.013	Eq. 4.10
η_{cool}, Tm B model	–	0.0044	0.02	Eq. 4.10

Chapter 5

Prospects for cryogenic cooling: spectroscopy

5.1 Introduction

This chapter develops predictions for cooling Tm^{3+}:ZBLANP to low temperatures. These predictions are based on emission and absorption spectroscopy at temperatures between 77 K and room temperature. Results and discussion include:

- Temperature dependence of external quantum efficiency (Table 5.1)
- Fluorescence measurements at various temperatures (Fig. 5.1)
- Absorptivity measurements using Fourier transform infrared spectroscopy (Fig. 5.5)
- Absorptivity measurements using the reciprocal relationship between emission and absorption cross sections (Figs. 5.7 through 5.12)

- Photo-luminescence excitation spectroscopy studies yielding highly-sensitive measurements of absorptivity in the long-wavelength region (Fig. 5.8, 5.10, and 5.12)

- Cooling efficiency calculations for temperatures between 77 K and 300 K (Fig. 5.14 and 5.15): sample Tm A can potentially cool to 150 K at a pump wavelength of 1.866 μm

5.2 Experiment, results, and discussion

There are certain nonlinearities involved in anti-Stokes fluorescence cooling. Cooling efficiency – proportional to the amount of temperature change per amount of absorbed power – is generally a function of temperature. Therefore any model for sample temperature change should include this nonlinearity with respect to temperature. The population of the dopant ensemble within each manifold is determined by the Boltzmann distribution $N(E) = N_0 exp[-E/k_B T]$ under a local thermal equilibrium assumption [19]. Because of this, spectroscopic quantities such as absorption and emission will change with temperature. The cooling power possible in a given experimental configuration is generally a function of temperature. Equation 2.6 is rewritten here explicitly:

$$P_{net}(T) = P_{in}(1 - e^{-\alpha_{total}(\nu,T)L}) \cdot \left[\frac{\alpha_b(T) + (1 - \widetilde{\eta_q})\alpha_r(\nu,T) - \alpha_r(\nu,T)\widetilde{\eta_q}\frac{h\nu_f(T) - h\nu}{h\nu}}{\alpha_{total}(\nu,T)} \right]. \quad (5.1)$$

As discussed in Chpt. 2, $\alpha_r(\nu,T)$ is the resonant absorption for the $^3H_6 \rightarrow ^3F_4$ transition, $h\nu_f(T)$ is the mean fluorescent photon energy, and $\widetilde{\eta_q}$ is the external

quantum efficiency given by Eq. 2.7. Total absorption is given by $\alpha_{total}(\nu, T) = \alpha_b + \alpha_r(\nu, T)$, where it is assumed that background absorption (α_b) has a negligible temperature dependence.

Phonon-electron interactions are a further source of nonlinearity in Eq. 5.1. For the transitions presently considered, these interactions in rare earth-doped glasses can be treated in a weak-coupling regime [14]. The probability of radiationless transitions to a lower level via the emission of phonons is expressed as a decay rate. As discussed in Chpt. 1, in the weak-coupling limit for transitions requiring many phonons, the rate takes the form of an exponential:

$$W_{nr} = W_0 exp[-\frac{ln(\varepsilon)}{\hbar\omega}\Delta E]. \tag{5.2}$$

In Eq. 5.2, ε is a measure of electron-phonon coupling, $\hbar\omega$ is the phonon energy involved in the decay transition, ΔE is the energy to the next lowest level of the decay transition. The temperature dependence is contained in the prefactor W_0. Using the Debye model for the density of phonon states in the material, $W_0 = C[n_\omega + 1]^p$, where p is the number of phonons required to bridge the transition gap ΔE and n_ω is the phonon occupation number given by the Bose-Einstein distribution function

$$n_\omega = \frac{1}{e^{\hbar\omega/k_B T} - 1}. \tag{5.3}$$

Together with room temperature data from Ref. [49], one can use the maximum phonon energy in ZBLANP, $\hbar\omega_{max} = 580$ cm^{-1} [51], to calculate how radiationless transitions affect quantum efficiency as the sample cools. For significant temperature changes, $\widetilde{\eta_q} \rightarrow \widetilde{\eta_q}(T)$ in Eq. 5.1 since $W_{nr} \rightarrow W_{nr}(T)$ in Eq. 2.7 with the temperature dependence contained in Eq. 5.3. Using the above relations, values for quantum

efficiency range from 0.99 at room temperature to 0.995 at 77 K – these are listed in Table 5.1.

Figure 5.1 shows fluorescence spectra at sample temperatures ranging from 77 K to 300 K. Fluorescence spectra were obtained using an Oriel MS257 spectrometer in a scanning monochrometer configuration. Figure 5.2 shows the experimental arrangement.

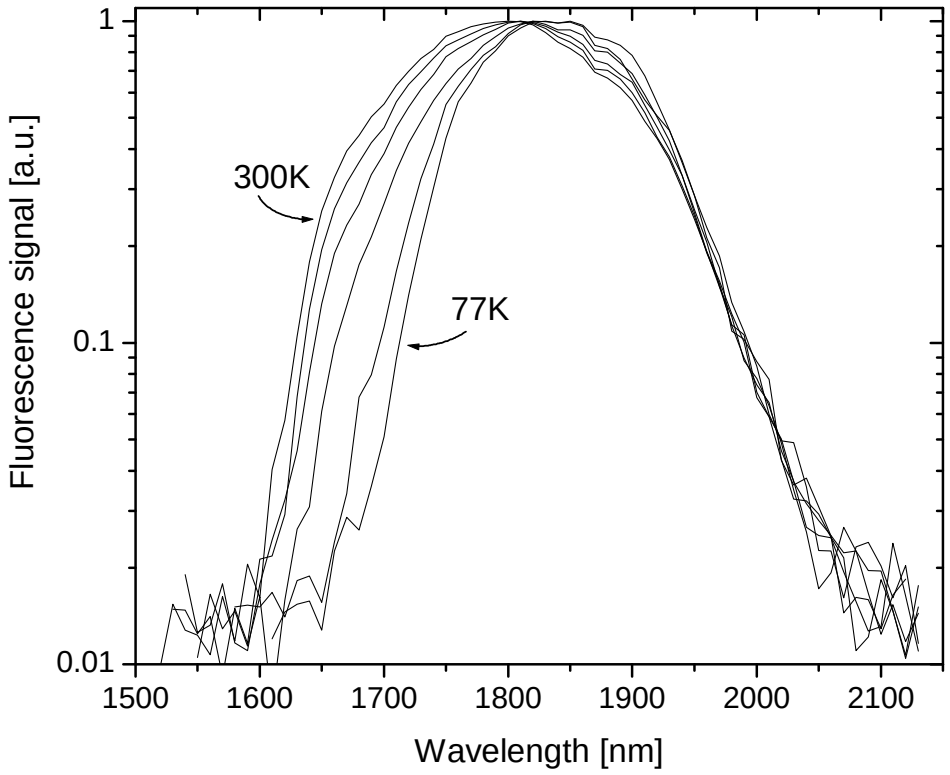

Figure 5.1: Sample Tm A fluorescence spectra. The solid lines correspond, from left to right beginning on the left side of the figure, to 300K, 250K, 200K, 150K, 100K, and 77K.

The sample is clamped in a copper mount connected to the cold finger in an optical cryostat (Janis Research). The pump beam enters sample Tm A along its long axis near its side to reduce fluorescence re-absorption. Fluorescence from this side passes

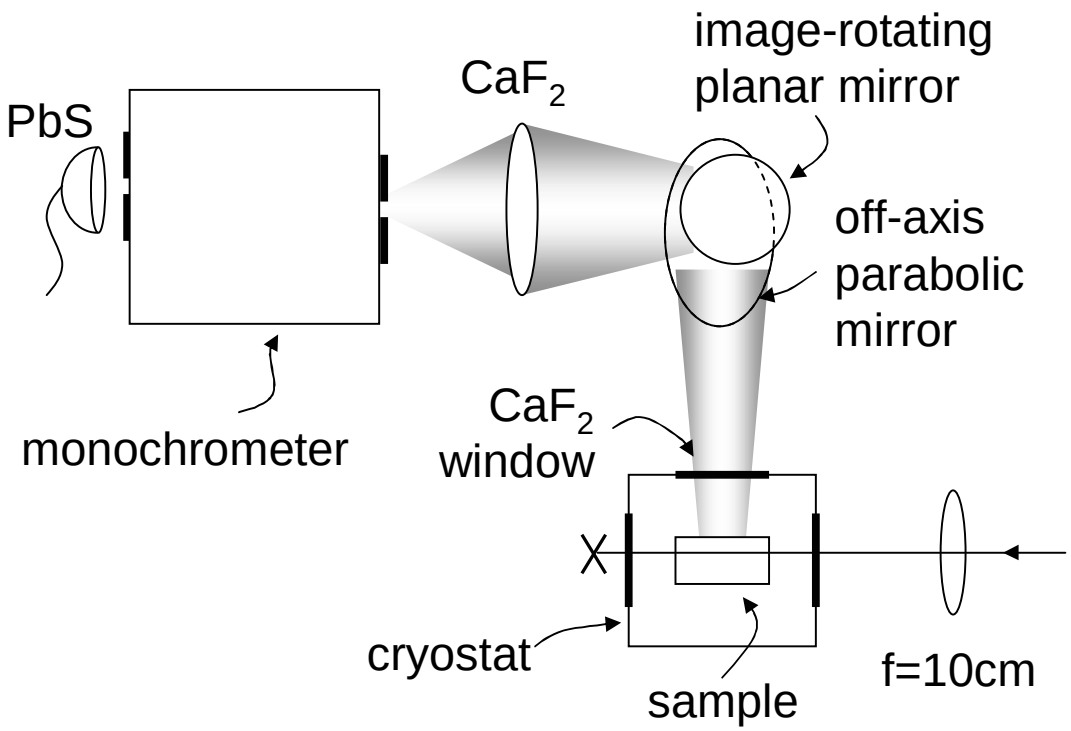

Figure 5.2: Experimental configuration for fluorescence measurements.

through a CaF_2 window and is collected with an off-axis parabolic mirror. The light is then reflected from a planar mirror in a periscope orientation with respect to the parabolic mirror in order to match the horizontal object line (fluorescence) to the vertical slit in the monochrometer. After the image-rotating reflection from the planar mirror, fluorescence is focused onto the input slit of the monochrometer through a CaF_2 lens. The PbS detector (Oriel) is AC-coupled so the radiation is chopped at $\sim$ 800 Hz to avoid 1/f-related noise. The 600 lines/mm grating is blazed for 1.6 μm. The detector is connected to a 102 kHz lock-in amplifier (Stanford Instruments, SR830). Data from the amplifier is collected by a computer that synchronously controls the operation of the spectrometer. Using a krypton arc lamp the spectrometer is calibrated to an accuracy of $\pm$1 nm. All fluorescence data is corrected for the response of the system. The data is normalized to the response of the PbS detector

and grating diffraction efficiency. Both of these factors are shown in Fig. 5.3(a). Since water has an absorption band near $\lambda = 2$ μm, spectra are corrected for an average optical density (αL) of $\sim$0.2. Water absorption is illustrated in Fig. 5.3(b).

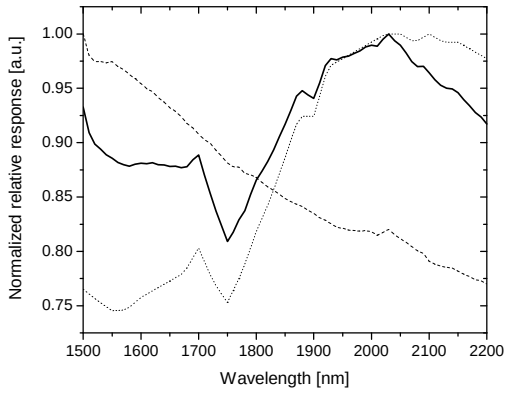

(a) PbS detector response (dotted line) and grating diffraction efficiency (dashed line). Their normalized product is indicated by the solid line.

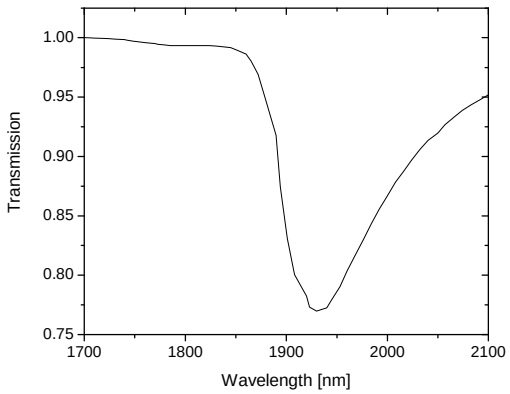

(b) Transmission through 20 μm

Figure 5.3: Spectrometer correction factors. In (a), the dashed line is relative grating diffraction efficiency, the dotted line is the relative response of the PbS detector, and the solid line is their normalized product. (b) Transmission through 20 μm of water.

The use of Fig. 5.3(b) to correct fluorescence spectra agrees with an estimate of effective water absorption based on humidity in the laboratory. The absorption length of water vapor (l_{abs}) can be expressed as

$$l_{abs} = A_w L_w L_p \frac{N_A P_w}{RT}, \tag{5.4}$$

where A_w is the cross-sectional area of water molecules, L_w is the diameter of the molecule, L_p is the physical length between sample and detector, N_A is Avagadro's number, P_w is the partial pressure of water vapor, R is Rydberg's constant, and T is temperature. With a molecular diameter of 2.8 Å [86] and a relative humidity of 25%, total absorption length is ~ 25 μm.

Fluorescence spectra for various sample temperatures is shown in Fig. 5.1. Spectra have been corrected for system response and water absorption as described above. The plots in the figure correspond, from left to right on the left side of the figure, to 300 K, 250 K, 200 K, 150 K, 100 K, and 77 K. Mean fluorescent wavelengths are calculated from these plots according to

$$\lambda_f = \frac{\int \lambda S(\lambda) d\lambda}{\int S(\lambda) d\lambda}, \tag{5.5}$$

where $S(\lambda)$ is the fluorescence power per unit wavelength $d\lambda$. Mean fluorescent wavelengths are listed in Table 5.1 and shown graphically in Fig. 5.4. Also in the latter figure is a solid line representing approximate expected behavior. Assume that the limits of integration in Eq. 5.5 are over the manifold where the emission originates and that $S(\lambda)$ has a simple temperature dependence according to the Boltzmann distribution. For simplicity, assume that this manifold has a homogeneous linewidth $g(\nu)$. Then we can write the mean fluorescent frequency as

$$\nu_f = \frac{\int_{up} g(\nu) e^{-h\nu/k_B T} \nu d\nu}{\int_{up} g(\nu) e^{-h\nu/k_B T} d\nu}. \tag{5.6}$$

As a first approximation assume that $g(\nu)$ is constant over the upper manifold. Make an algebraic substitution to obtain

$$\nu_f = \frac{k_B T}{h} \frac{\int_{up} e^{-x} x dx}{\int_{up} e^{-x} dx}. \tag{5.7}$$

After carrying out the integration we obtain

$$\nu_f = \frac{k_B T}{h} \left[1 + \frac{h\nu_1}{k_B T} \frac{1 - \frac{\nu_2}{\nu_1} exp[-\Delta E / k_B T]}{1 - exp[-\Delta E / k_B T]} \right], \tag{5.8}$$

where $\nu_{2,1}$ correspond to the upper and lower limits of integration, which are the highest and lowest intra-manifold energies in the originating manifold, respectively. The difference between these energies is $\Delta E = h(\nu_2 - \nu_1)$. Equation 5.8 is plotted as the solid line in Fig. 5.4 for an frequency ν_1 corresponding to an energy of 5362 cm^{-1} (1.86 μm) and a manifold width of 500 cm^{-1}.

Table 5.1: Modelling parameters

Temperature [K]	λ_f [nm]	$\widetilde{\eta_q}$
77	1846	0.995
100	1840	0.995
150	1827	0.995
200	1816	0.994
250	1809	0.992
300	1803	0.990

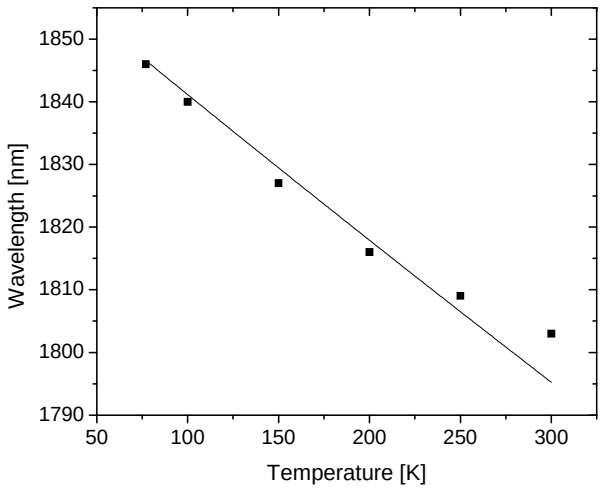

Figure 5.4: Mean fluorescent wavelength as a function of temperature. The solid line is an approximate fit using Eq. 5.8
.

Absorption spectra for sample Tm A at temperatures between 77 K and 300 K are shown in Fig. 5.5. Absorptivity is obtained using a ThermoNicolet Fourier transform infrared (FTIR) spectrometer with a resolution of 4 cm^{-1}. The sample is clamped in a copper mount inside an optical cryostat (Janis Research), which is then placed in the FTIR spectrometer. Plots in Fig. 5.5 correspond, from right to left on the right side of the figure, to 300 K, 250 K, 200 K, 150 K, 100 K, and 77 K. Also shown in the figure as filled boxes are the results of absolute absorptivity measurements at room temperature taken directly with the tunable OPO. These measurements comprised measuring the power of the loosely-focused OPO beam before and after the sample. The 300 K absorptivity measurement is co-incident with the absolute measurement at high absorption, so re-normalization of the 300 K FTIR data is unnecessary. The baselines of the FTIR data at other temperatures are slightly adjusted to match that of 300 K absorptivity.

A local thermal equilibrium (LTE) model assumes that the populations in manifolds $^3H_6$ and $^3F_4$ reach thermal equilibrium within their respective manifolds on a

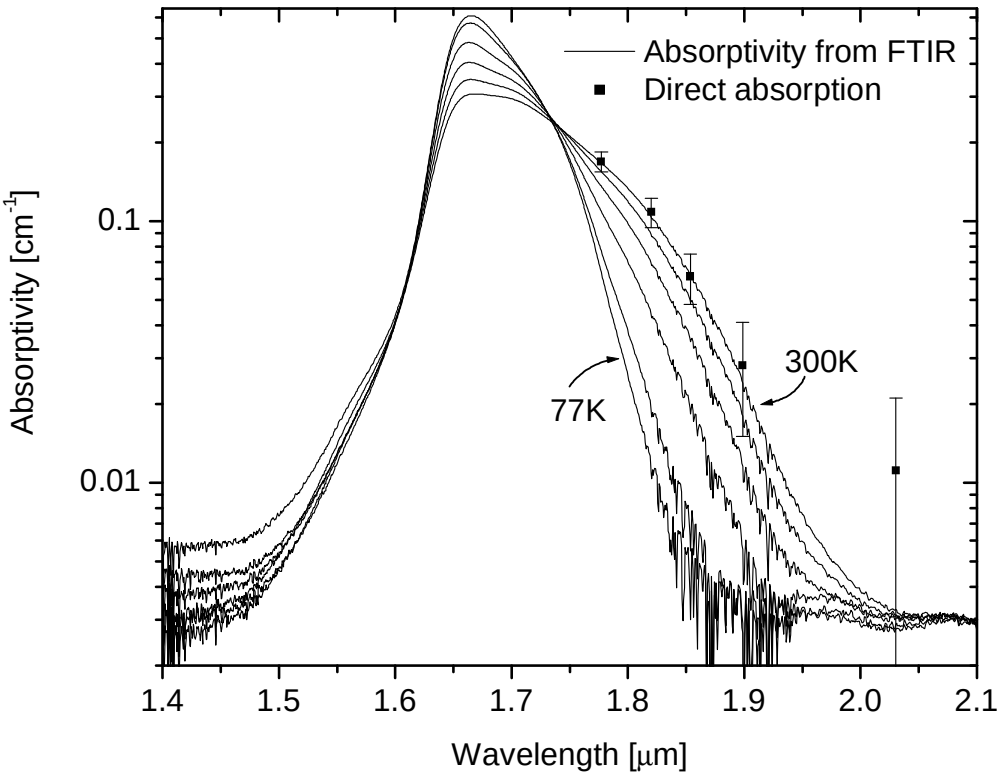

Figure 5.5: FTIR absorptivity for all temperatures. The solid lines correspond, from right to left beginning on the right side of the figure, to 300 K, 250 K, 200 K, 150 K, 100 K, and 77 K. Filled boxes indicate absolute absorptivity measurements at room temperature taken directly with the tunable OPO.

time scale short with respect to radiative decay. Rare-earth ions in glass hosts are subject to inhomogeneous broadening and have many small energy splittings within each manifold [14, 19]. A simple picture of quasi-continuous energies within each manifold is therefore appropriate. Following the treatment of Verdeyen [19], one can then express the stimulated emission and absorptive rates as integrals over the energy distributions in each corresponding manifold. The two manifolds are shown in Fig. 5.6 with lowest intramanifold energies $E_{1,0}$ and $E_{2,0}$ and manifold widths ΔE_1 and ΔE_2. These integrals contain factors that reflect the temperature-related Boltzmann population distribution as well as the Einstein B-coefficients for this transition. Re-

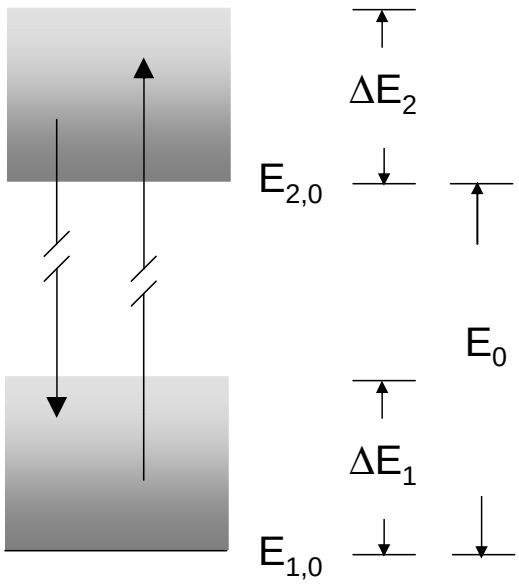

Figure 5.6: Energy manifold diagram.

expressing these integrals as absorption and emission cross sections (σ_{abs} and σ_{em}), one finds the ratio [19]

$$\frac{\sigma_{abs}(\nu)}{\sigma_{em}(\nu)} = e^{h\nu/kT}\frac{N_{2eq}}{N_{1eq}} \tag{5.9}$$

$$= e^{h\nu/kT}\left[\frac{g_2/\Delta E_2}{g_1/\Delta E_1}\frac{Z_2(T)}{Z_1(T)}e^{-E_0/kT}\right]. \tag{5.10}$$

In Eq. 5.9, N_{1eq} and N_{2eq} are the total populations in manifolds one and two at true thermal equilibrium. Photon energy is $h\nu$, k_BT is thermal energy, $g_{1,2}$ are degeneracy factors, and E_0 is the lowest energy level in the upper manifold as shown in Fig. 5.6. The function $Z_i(T) = (1 - exp[-\Delta E_i/k_BT])$ is used to describe the atomic populations at the lowest energy manifold edge, which are proportional to $1/Z_i(T)$. The relationship between cross sections in Eq. 5.9 is general [87] and the

specification made in Eq. 5.10 is particular for a LTE situation. The integrals over energies in each manifold for absorption and emission have cancelled in the ratio of Eq. 5.9 since the Einstein coefficients for absorption and emission are directly related. Defining an energy ϵ such that the bracketed quantity is $exp[-\epsilon/k_BT]$, Eq. 5.10 is expressed

$$\sigma_{abs}(\nu) = e^{(h\nu-\epsilon)/k_BT}\sigma_{em}(\nu). \tag{5.11}$$

This reciprocal relationship between cross sections was first established by McCumber [20] and later generalized by other researchers [87, 88, 89]. It is the reason that the absorption data appear to cross at a single wavelength for all temperatures in Fig. 5.5. If we assume that the non-exponential terms on the right-hand side of Eq. 5.10 are independent of temperature (valid for $\Delta E_i \gg k_BT$), they can be included in the exponential involving E_0 as an adjustment to this energy. If all of the other temperature dependence is included in the exponential (i.e. cross sections do not depend explicitly on temperature), then there is a certain pump photon energy in Eq. 5.10 for which absorption is approximately independent of temperature. Further, the order of this photon energy is E_0. Figure 5.5 indicates that the wavelength corresponding to this energy is ~ 1.74 μm, or 5700 cm^{-1} and the peak of absorption is at ~ 6000 cm^{-1}.

Stimulated emission is related to spontaneous emission by

$$\sigma_{em}(\nu) = A_{21}g(\nu)\frac{\lambda_0^2}{8\pi n^2}, \tag{5.12}$$

where A_{21} is the Einstein A-coefficient for the transition, $g(\nu)$ is the lineshape, λ_0 is the center free-space wavelength, and n is index of refraction. Absorptivity ($\alpha(\nu)$)

is described by the Beer-Lambert Law [14] for irradiance attenuation $I(z)/I_0 = exp[-\alpha(\nu)z]$ and is related to absorption cross section by

$$\sigma_{abs}(\nu) = \frac{\alpha(\nu)}{N_1}, \tag{5.13}$$

where N_1 is the population density. Multiplying Eq. 5.12 by the population density of manifold two (N_2) we find

$$N_2\sigma_{em} = F_p(\nu)\frac{c^2}{\nu^2 n^2}. \tag{5.14}$$

In Eq. 5.14, $F_p(\nu)$ is the number of fluorescent photons emitted from a unit volume per element frequency per element solid angle. Absorptivity can then be expressed in terms of fluorescence power per unit wavelength ($S(\lambda)$) [51]:

$$\alpha(\lambda) \propto \lambda^5 S(\lambda) exp\left[\frac{hc}{\lambda k_B T}\right]. \tag{5.15}$$

Figures 5.7 through 5.12 display fluorescence and FTIR absorptivity data as described above, in addition to absorptivity derived from fluorescence data as described by Eq. 5.15 for 77 K, 100 K, 150 K, 200 K, 250 K, and 300 K. Absorptivity obtained from reciprocity has been normalized to FTIR absorptivity at large absorptions in each case. As can be seen from the figures, this method yields values for absorptivity at relevant wavelengths over an order of magnitude below the noise floor for the FTIR spectrometer. For this reason, values obtained in this manner are used for all modelling below.

In addition to the reciprocity method described above, photo-luminescence excitation (PLE) spectroscopy offers a sensitive absorption measurement technique [90].

The number of absorbed photons per second in a given sample is proportional to the abosorption cross section of the relevant transition, the atom number density, the number of laser photons, and the sample length. Assuming unity quantum efficiency, in steady-state the number of fluorescence photons emitted per second is equal to absorbed photons. Given an excitation laser at ω the number of fluorescence photons collected per second is proportional to the number of absorbed laser photons, with the proportionality constant depending on factors such as the size of collection optics, efficiency of the detector, etc. The absorption information is therefore contained in an integrated fluorescence signal. Normalizing each collected PLE signal to the input laser power at ω, one obtains a relative map of absorptivity. This highly sensitive map is limited by the noise of the laser and sensitivity of the detection system. The latter can be quite high.

Figures 5.8, 5.10, and 5.12 show the results of PLE spectroscopy for sample Tm A at 100 K, 200 K and 300 K, respectively. In an experimental setup similar to that of fluorescence measurements described above, the OPO is tuned to a certain wavelength and passes through the sample. Instead of scanning the grating in the spectrometer as in the monochrometer configuration described above, the grating is fixed and a large exit slit is used ($\sim$ 1 mm) to select a portion of the spectrum that does not include the pump wavelength. In this way the detector signal integrates over a portion of the fluorescence at each pump wavelength. As seen in the figures, after normalizing to the FTIR spectra at large absorptions, the PLE spectra agrees remarkably well with reciprocity spectra.

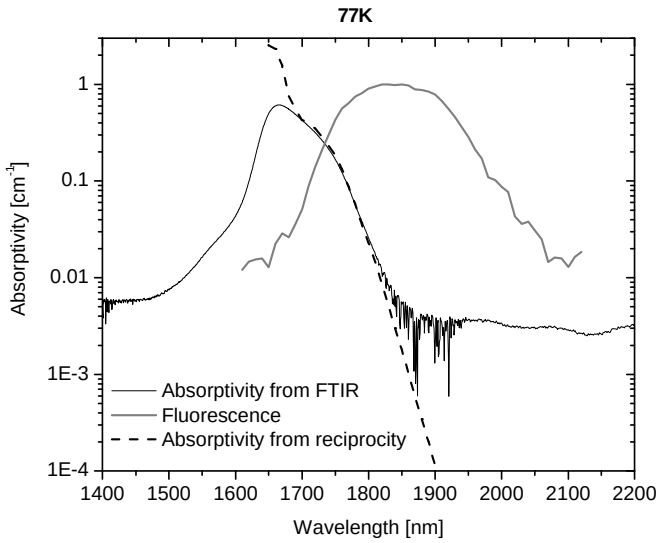

Figure 5.7: Fluorescence (grey solid line), FTIR (black solid line) and reciprocity spectra (dashed line) for 77 K. Fluorescence is given in arbitrary units.

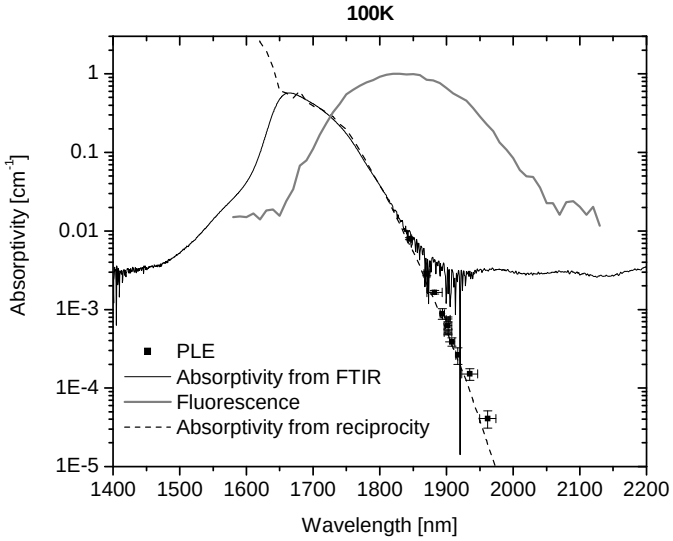

Figure 5.8: Fluorescence (grey solid line), FTIR (black solid line), PLE (data points) and reciprocity spectra (dashed line) for 100 K. Fluorescence is given in arbitrary units.

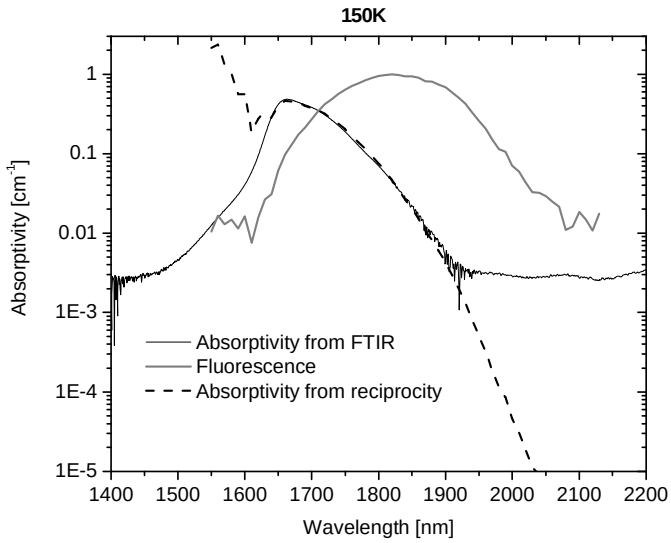

Figure 5.9: Fluorescence (grey solid line), FTIR (black solid line) and reciprocity spectra (dashed line) for 150 K. Fluorescence is given in arbitrary units.

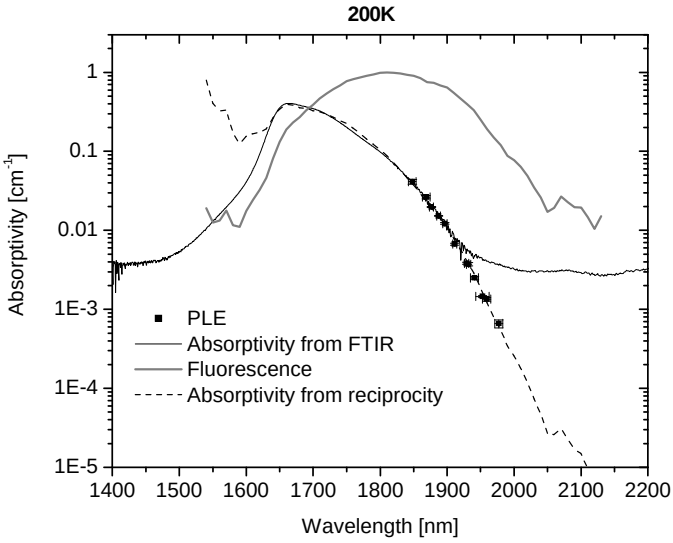

Figure 5.10: Fluorescence (grey solid line), FTIR (black solid line), PLE (data points) and reciprocity spectra (dashed line) for 200 K. Fluorescence is given in arbitrary units.

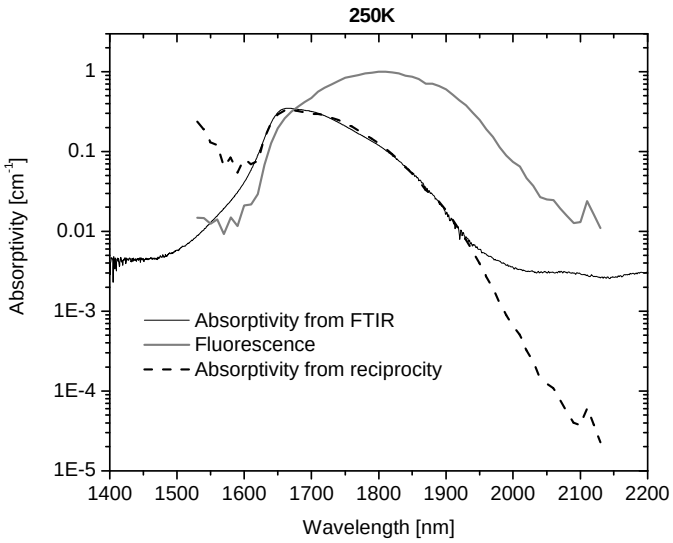

Figure 5.11: Fluorescence (grey solid line), FTIR (black solid line) and reciprocity spectra (dashed line) for 250 K. Fluorescence is given in arbitrary units.

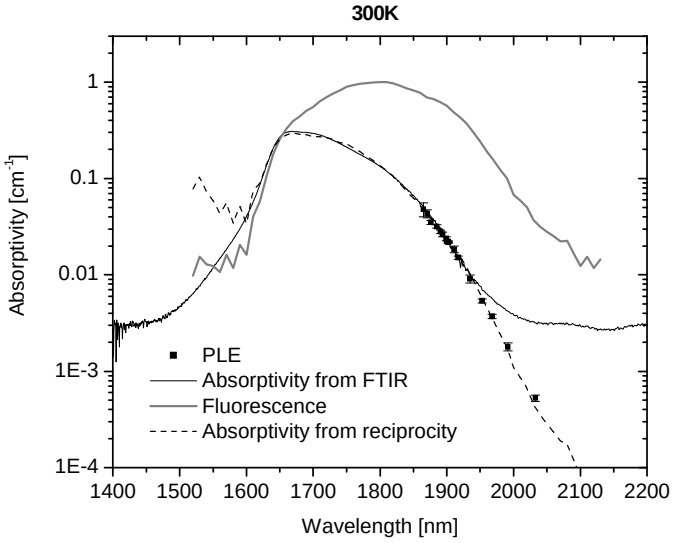

Figure 5.12: Fluorescence (grey solid line), FTIR (black solid line), PLE (data points) and reciprocity spectra (dashed line) for 300 K. Fluorescence is given in arbitrary units.

Using the values determined by the above spectra, cooling (or heating) behavior at low temperatures can be predicted. Cooling efficiency is the second bracketed term in Eq. 5.1:

$$\eta_{cool}(T,\lambda) = \frac{\alpha_b(T) + [1-\widetilde{\eta_q}(T)]\alpha_r(\lambda,T) - \alpha_r(\lambda,T)\widetilde{\eta_q}(T)\frac{\lambda-\lambda_f(T)}{\lambda_f(T)}}{\alpha_{total}(\lambda,T)}. \tag{5.16}$$

For the modelling below, background absorption is assumed to be independent of temperature (*i.e.* $\alpha_b(T) \rightarrow \alpha$). Each quantity in Eq. 5.16 has been defined above. To find the lowest attainable temperature, the roots of $\eta_{cool}(\alpha_r, T) = 0$ from the Eq. 5.16 are found at a given temperature for each pump wavelength (λ) in the cooling region. This yields absorptivity as a function of pump wavelength. These roots are plotted for a given temperature as a function of λ and any intersection with the known aborptivity indicates a solution. A single intersection will correspond to the minimum attainable temperature. Two intersections indicate the wavelength region over which cooling is possible (*c.f.* Fig. 4.6). Keeping background absorption fixed at $\alpha_b = 2 \times 10^{-4}$ cm^{-1} and including the temperature dependence of quantum efficiency discussed above, one finds that sample Tm A can reach a temperature of 150 K at a pump wavelength of 1.866 μm. Numerical results using these assumptions are shown for 100 K, 150 K and 200 K in Fig. 5.13. Absorptivity obtained by the reciprocity method are the lines beginning at top-left (labelled by temperature), while the root-solutions are the corresponding curved lines. The absence of an intersection of the reciprocity absorptivity at 100 K and the numerical solution for the same temperature indicates that cooling is not possible at any pump wavelength for this temperature under the above assumptions. Two intersections of the two plots for 200 K suggests that cooling is possible at this temperature for pump wavelengths between $\sim$ 1834 nm and $\sim$ 1934 nm. A single intersection of the two plots for 150 K indicates that cooling is possible to this minimum temperature in the vicinity of $\lambda = 1866$ nm (*i.e.* ± 9 nm).

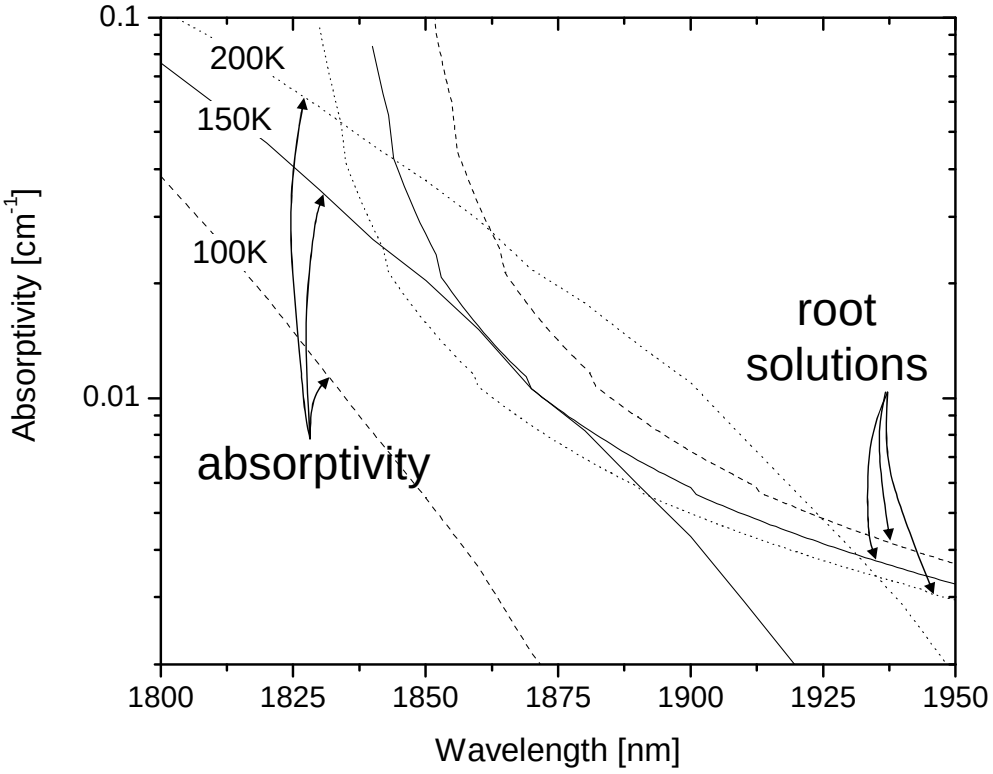

Figure 5.13: Graphical solution for nonlinear cooling efficiency. Absorptivity obtained by reciprocity is indicated by the lines beginning at top left and are labelled by temperature. Root-solutions as described in the text are the corresponding curves.

Figure 5.14 shows the values of cooling efficiency calculated from Eq. 5.16 for various pump wavelengths. Fixing background absorption at $\alpha_b = 2 \times 10^{-4}$ cm^{-1} and including the temperature dependance of quantum efficiency discussed above (see Table 5.1), results are plotted for two fixed pump wavelengths. Open circles correspond to $\lambda = 1.9$ μm and filled triangles to $\lambda = 1.866$ μm. Also shown in the figure is the case of ideal efficiency (filled boxes), where background absorption is fixed at zero and quantum efficiency at unity. Here the limit is obtained:

$$\eta_{cool}(T) = \frac{\lambda - \lambda_f(T)}{\lambda_f(T)}. \tag{5.17}$$

For this ideal case in the figure, the pump wavelength is chosen at each temperature such that absorptivity is 10^{-3} cm^{-1}. Figure 5.15 shows the values of cooling efficiency

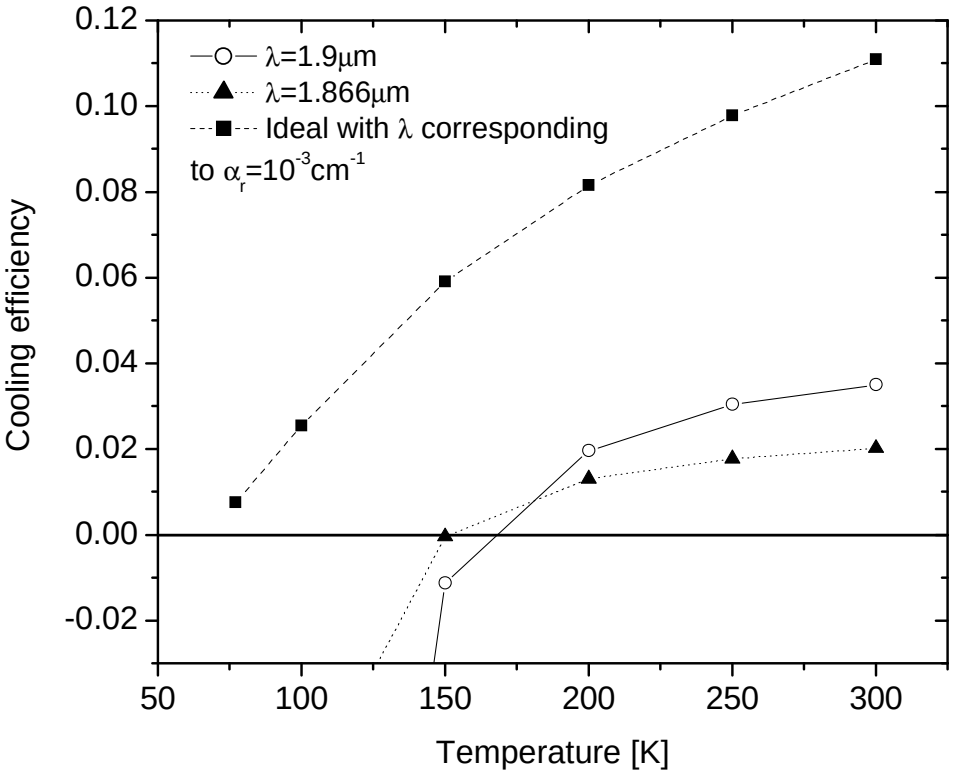

Figure 5.14: Cooling efficiency as a function of temperature for three pump wavelengths. Also included is the ideal efficiency corresponding to zero background absorption and unity quantum efficiency. For this ideal case, the pump wavelength is chosen at each temperature such that absorptivity is 10^{-3} cm^{-1}.

calculated from Eq. 5.16 for a pump wavelength of $\lambda = 1.866$ μm and four different values of background absorption, varying from $\alpha_b = 4 \times 10^{-4}$ cm^{-1} to $\alpha_b = 5 \times 10^{-5}$ cm^{-1}. As indicated by the figure, for the latter absorption sample Tm A could, in principle, cool to less than ~ 125 K.

Practical considerations for reaching low temperatures are determined by the radiative, conductive and convective heat load to the sample from its environment.

Conductive loads are reduced by careful attention to sample mounts as discussed in Chpt. 4. By considering energy carried to the sample by air molecules we calculate that convective loads are negligible for vacuum pressures below 10^{-4} Torr. This pressure is easily achieved in practice. As described above in Chpt. 2 (*c.f.* Eq. 2.11), radiative load is determined by factors such as sample and chamber surface areas, as well as their respective emissivities. As discussed in Section 4.4, sample mounts can be constructed as miniature chambers with low-emissivity coatings (see Fig. 4.24). Along with relatively low sample surface area and high absorbed power, practical efforts such as these could feasibly lead to the low temperatures predicted in Fig. 5.15.

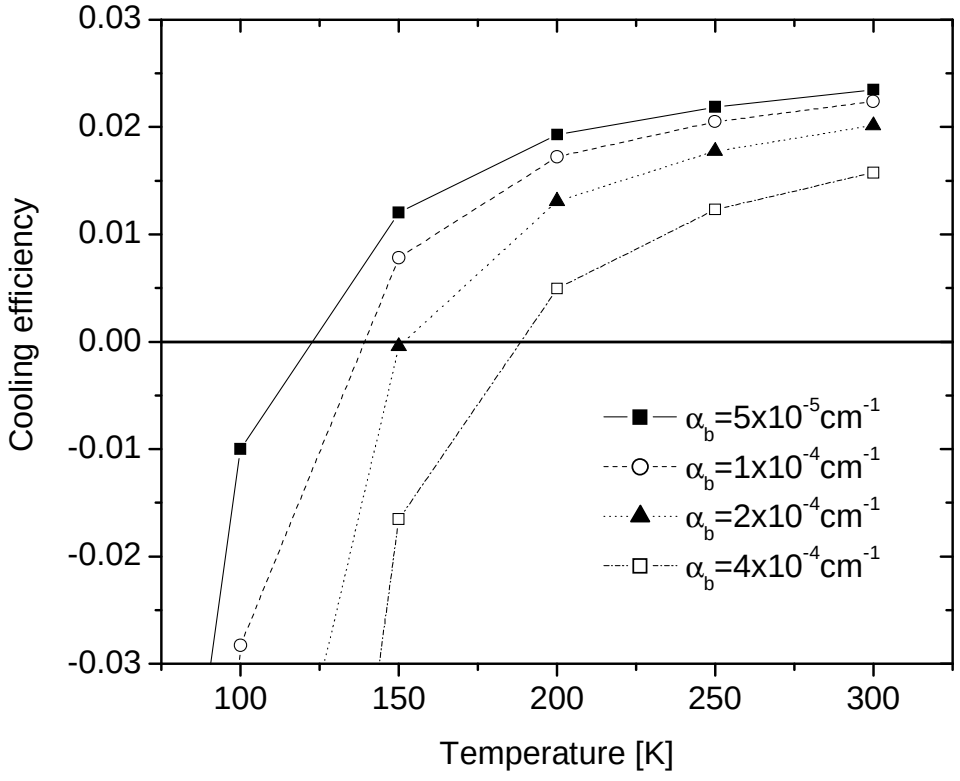

Figure 5.15: Cooling efficiency as a function of temperature for $\lambda = 1.866$ μm and four values of background absorption. The value from experimental fits is $\alpha_b = 2 \times 10^{-4}$ cm^{-1}.

Chapter 6

Future work

6.1 Introduction

The work presented in this manuscript can be extended and its methods improved. Relatively straightforward ideas could lead to lower temperatures and a better understanding of the physical processes involved in cooling. These may include the following:

- The special sample chamber discussed in Chpt. 4 can be actively cooled to ambient temperature. The effect of reduced chamber surface area and emissivity might then be separated from the effects of a poor heat sink as shown in Fig. 4.26. A reduced heat load (discussed in text) might then be recovered. Research into other materials that absorb in the $\sim$ 2 μm wavelength range and have relatively low emissivity such as PbTe, InAs, InSb and Ge should be pursued.

- The predictions of Chpt. 5 can be tested by cooling the sample at low temperatures. Together with a relatively long sample to increase the signal-to-noise

ratio, the large dynamic range of the interferometer should enable successful testing.

- Mirror deposition should be pursued further with particular attention to the benefits of ion beam sputtering techniques.

- Monolithic optical maze processing technology should be refined to assure tight tolerances on its right angles. Even small deviations from 90 degrees will cause the beam to deviate after a number of passes such that it no longer meets the condition of total internal reflection.

- Radiative heat load to the sample could be dramatically decreased by using a host material such as BaYF that has low emissivity.

6.2 External resonant cavity

Chapter 4 proved the success of using a non-resonant cavity (NRC) arrangement to increase absorbed power. Relative to single-pass cooling in sample Tm A, an increase in absorbed power of 480% is obtained when Brewster-cut sample Tm C with similar length is cooled in a NRC. Only 51% of the incident power is absorbed in this case, however. It may be possible to improve this fraction, even to the point of nearing 100%. This may be achieved by placing the sample in a resonant cavity external to the pump source as shown in Fig. 6.1 [91]. Since high intracavity power relies on interference effects the OPO must be operated in a continuous-wave configuration, which is accomplished by disengaging the active-modelocking system in the OPO pump source. OPO threshold increases according to a decrease in peak irradiance.

Consider the external resonant cavity (ERC) as shown in the figure with mirror reflectances $R_{1,2}$ and transmittances $T_{1,2}$. The single-pass phase in a cavity of length L and sample with length l, index n, and facet transmittance T_f is $\theta = k_0 L + \Delta n k_0 l -$

$i\alpha_r(\lambda)l/2$ for a laser wavenumber k_0, $\Delta n = n - 1$, and absorptivity $\alpha_r(\lambda)$. The absorptivity in this phase relation corresponds to that defined through the Beer-Lambert irradiance attenuation law. After coherently adding fields on sequential passes and using a geometric series simplification, the total irradiance transmitted through the ERC (*i.e.* travelling to the right of mirror 2) in Fig. 6.1 is

$$I_{trans}(\theta) = I_{inc}\frac{T_f^2(1-R_1)(1-R_2)}{(1-T_f^2\sqrt{R_1R_2})^2 + 4T_f^2\sqrt{R_1R_2}sin^2\theta}, \tag{6.1}$$

where $T_f = 1 - R_f$ is the transmittance of the sample facet. Similarly, the reflected irradiance $I_{ref}(\theta)$ is

$$I_{ref}(\theta) = I_{inc}\frac{(1-R_1)^2R_2T_f^4 - 2(1-R_1)\sqrt{R_1R_2}T_f^2(1-2sin^2\theta - \sqrt{R_1R_2}T_f^2)}{(1-T_f^2\sqrt{R_1R_2})^2 + 4T_f^2\sqrt{R_1R_2}sin^2\theta} + R_1. \tag{6.2}$$

Equations 6.2 and 6.1 are combined to yield a measure of fractional intracavity irradiance (I_{ic}):

$$I_{ic}(\theta) = 1 - [I_{ref}(\theta) + I_{trans}(\theta)], \tag{6.3}$$

where incident irradiance is normalized to unity. Intracavity power at resonance condition (*i.e.* $Re[\theta] = m\pi$ for m $= 0, 1 \ldots$) is shown in Fig. 6.2 (solid line) for a typical absorptivity $\alpha_r = 0.02$ cm^{-1}, a facet transmittance $T_f = 0.96$ and a reflectance $R = 1$ for the second mirror. Multiple-cavity coherent effects due to the internal surfaces are neglected. The dashed line represents fractional intracavity resonant irradiance according to

$$I'_{ic}(\theta) = 1 - [I_{ref}(\theta) + I_{trans}(\theta) + I_{ref1}(\theta) + I_{ref2}(\theta)], \tag{6.4}$$

where $I_{ref1,2}$ are the irradiances corresponding to field losses from reflection at either side of the sample as shown in Fig. 6.1.

The intracavity irradiance described by Eq. 6.4 represents absorbed power relative to incident power, assuming that all losses at the sample facets are not absorbed. The dotted line in Fig. 6.2 indicates the reflected relative irradiance described by Eq. 6.2 for a second mirror with 100% reflectance. By setting the derivative of Eq. 6.4 equal to zero and solving for R_1, we find that the reflectance of mirror 1 for maximum absorbed power for a given absorptivity $\alpha_r(\lambda)$ is $R_1 = exp(-2\alpha_r(\lambda)l)$.

This represents a nonlinear system since index change (Δn) will vary with temperature and the resonance condition will correspondingly change. As indicated in Fig. 6.1, active stabilization of the cavity is necessary. Further, since ZBLANP has been calibrated for net phase shift as a function of temperature (*c.f.* Eq. 4.1), this feedback mechanism will allow temperature to be determined.

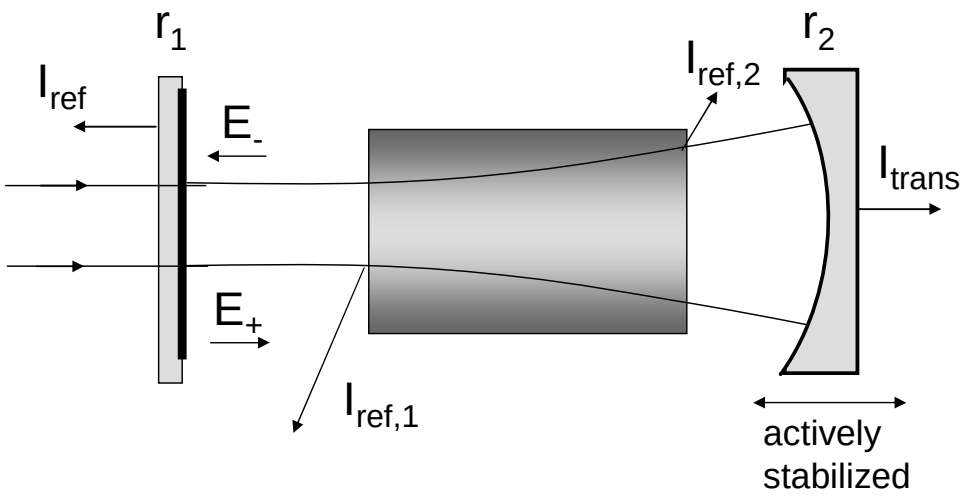

Figure 6.1: External resonant cavity arrangement. The OPO pump beam is mode-matched to the cavity with high-reflectance mirrors. As the sample cools the condition for resonance changes and cavity length must be actively stabilized.

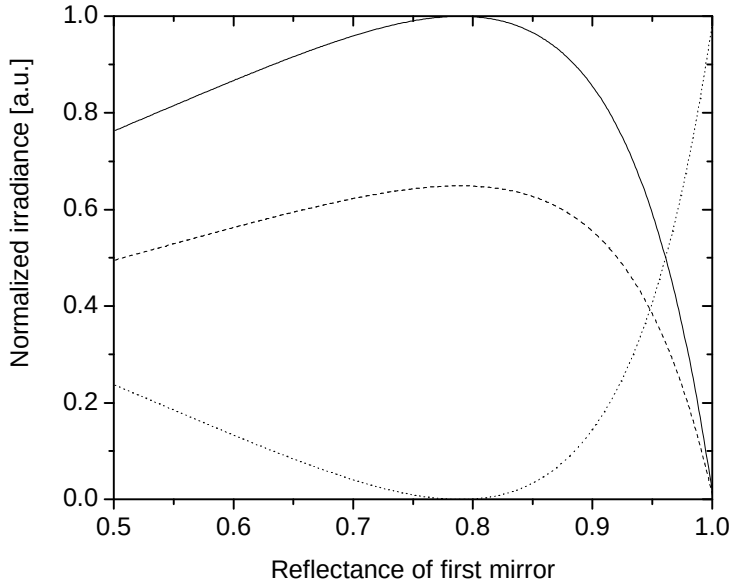

Figure 6.2: Intracavity pump power in the external resonant cavity arrangement as a function first mirror reflectance for the case of unity reflectance for the second mirror. The solid line represents a fractional irradiance inside the cavity but disregards losses due to sample facets. The dashed line signifies intracavity irradiance including facet losses. The dotted line is irradiance reflected from the cavity if facet losses are disregarded.

Appendix

A Cooling time constant

B OPO autocorrelation measurements

C Mach-Zehnder interferometer error analysis

Appendix A

Cooling time constant

The rate of heat flow in the system consisting of the sample and surrounding chamber is given by [36]

$$C\frac{dT}{dt} = P_{total}. \tag{A.1}$$

In Eq. A.1, C is the sample's heat capacity, dT/dt is its change in temperature in a differential time, and P_{total} is the total power. The latter quantity includes the net power deposited by the laser to the sample as in Eq. 2.6 ($P_{cool} = P_{abs}\eta_{cool}$ for negative temperature changes), and, assuming negligible convective and conductive loads, the radiative load to the sample given by Eq. 2.11.

Inserting the sum of P_{cool} and the expression for radiative load in Eq. 2.11 as P_{total} in Eq. A.1, for small temperature changes we obtain

$$C\frac{dT_s}{dt} = P_{abs}\eta_{cool} + 4\epsilon_s\sigma A_s\frac{1}{1+\chi}T_c^3\Delta T. \tag{A.2}$$

In Eq. A.2, P_{abs} is absorbed power, η_{cool} is cooling efficiency, σ is the Stefan-Boltzmann constant, A_s is sample surface area, $T_{s,c}$ is the sample and chamber temperature, $\Delta T = T_c - T_s$ is the difference between chamber and sample temperature, and $\chi \equiv (\epsilon_s A_s/\epsilon_c A_c)(1-\epsilon_c)$ where $\epsilon_{s,c}$ are the sample and chamber emissivities, respectively.

Now define a characteristic constant with units of a rate:

$$k \equiv \frac{4\epsilon_s \sigma A_s T_c^3}{C(1+\chi)}. \tag{A.3}$$

Now Eq. A.2 can be expressed

$$dT_s = \left[\frac{P_{abs}\eta_{cool}}{C} + k\Delta T\right] dt. \tag{A.4}$$

With the initial condition $T_s = T_{s,0}$ at $t = 0$, the solution to Eq. A.4 is

$$\Delta T = \Delta T_0 exp[-kt] + \frac{P_{abs}\eta_{cool}}{kC}(exp[-kt] - 1), \tag{A.5}$$

where $\Delta T_0 = T_c - T_{s,0}$. Given the initial condition $T_{s,0} = T_c$ this reduces to

$$\Delta T = \frac{P_{abs}\eta_{cool}}{kC}(exp[-t/\tau] - 1), \tag{A.6}$$

where $\tau \equiv 1/k$. Heat capacity is related to specific heat (c_m) as $C = c_m \rho V_s$, where ρ and V_s are sample density and volume, respectively. So from Eq. A.3,

$$\tau = \frac{c_m \rho V_s (1+\chi)}{4\epsilon_s \sigma A_s T_c^3}. \tag{A.7}$$

See Table 4.5 and Fig. 4.20 for numerical examples.

Appendix B

OPO autocorrelation measurements

The experimental arrangement to obtain second order autocorrelations (pulsewidths) of the OPO beam is shown in Fig. B.1. The second harmonic of the OPO ($\sim 1.87\ \mu$m) is generated from a KTP crystal ($KTiOPO_4$, potassium titanyl phosphate) cut for type II phasematching (o + e $\rightarrow$ o for positive uniaxial crystal ($n_e > n_o$) [59]). Since the OPO beam is P-polarized with respect to the autocorrelator mirrors and no polarizing optics are used, the crystal must be oriented such that the beam is at an angle $\pi/2$ with respect to the crystal phasematching angles. As shown in the figure two corner cubes are used in a Michelson interferometer arrangement, one mounted on a long translation stage (Newport). The stage is controlled via serial communications by a computer, which synchronously records both the reference (extended indium-gallium-arsenide) and signal (silicon) detectors. The collinear arms result in an interferometric signal, which can be interpreted as an intensity autocorrelation by averaging over the phase-dependent terms. In the absence of a rapidly moving corner cube in the translated arm, this can be done by averaging through many passes or simply averaging the interferometric data in software. The latter technique yields

the autocorrelation traces for the case of intra-cavity prism in Fig. B.3 and Fig. B.2.

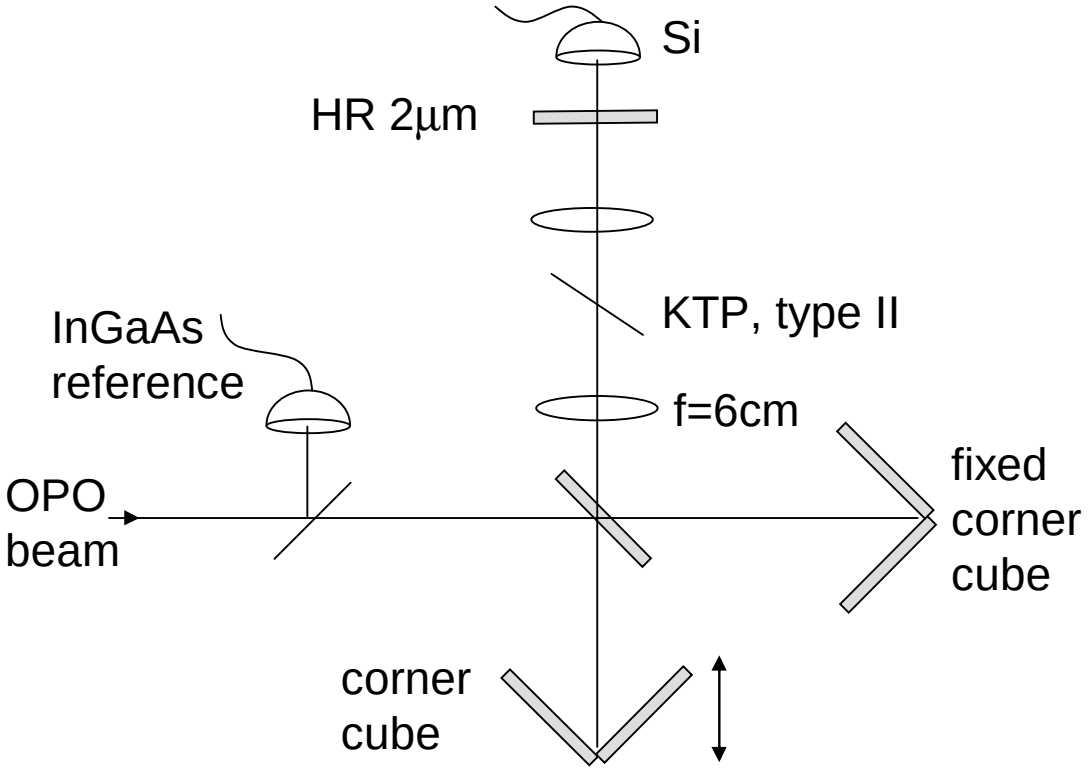

Figure B.1: Interferometric autocorrelation experimental setup. The KTP crystal is cut for type II phasematching.

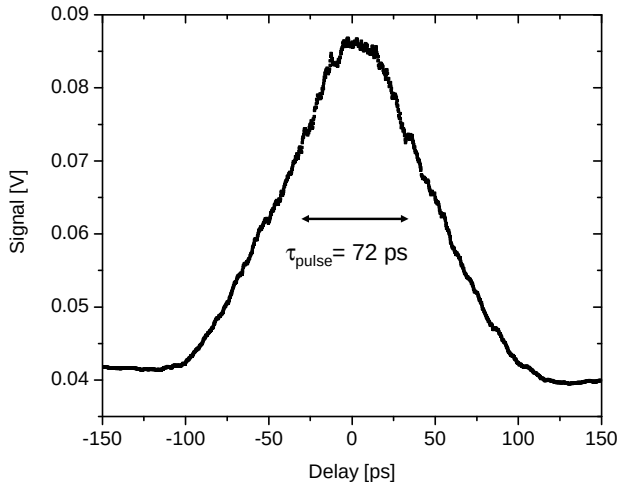

Figure B.2: Second-order autocorrelation trace of the OPO pulse when a frequency-stabilizing prism is introduced into the cavity. Assuming a Gaussian pulse-shape, the full width, half maximum of the pulse is 77 ps.

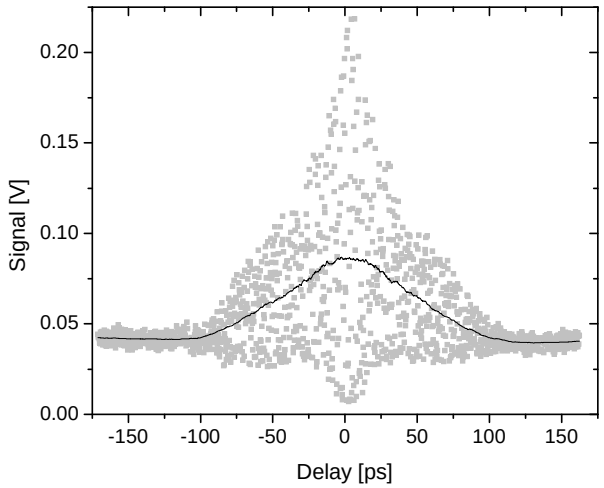

Figure B.3: Interferometric autocorrelation trace of the OPO pulse when a frequency-stabilizing prism is introduced into the cavity. Assuming a Gaussian pulse shape, the full width, half maximum of the pulse is 77 ps. The solid line is an intensity autocorrelation resulting from averaging over the interferometric data in software.

The characteristic temporal width of the pump pulses from the Nd^{3+}:YAG laser (Coherent Antares) were obtained in a similar arrangement shown in Fig. B.4. The KTP type II crystal is replaced by a KTP crystal cut for type I phasematching. The non-collinear arms are focused into the crystal leading to a true background-free second harmonic signal. The vector phasematching scheme is illustrated in the inset. Data showing the autocorrelation signal is shown in Fig. B.5.

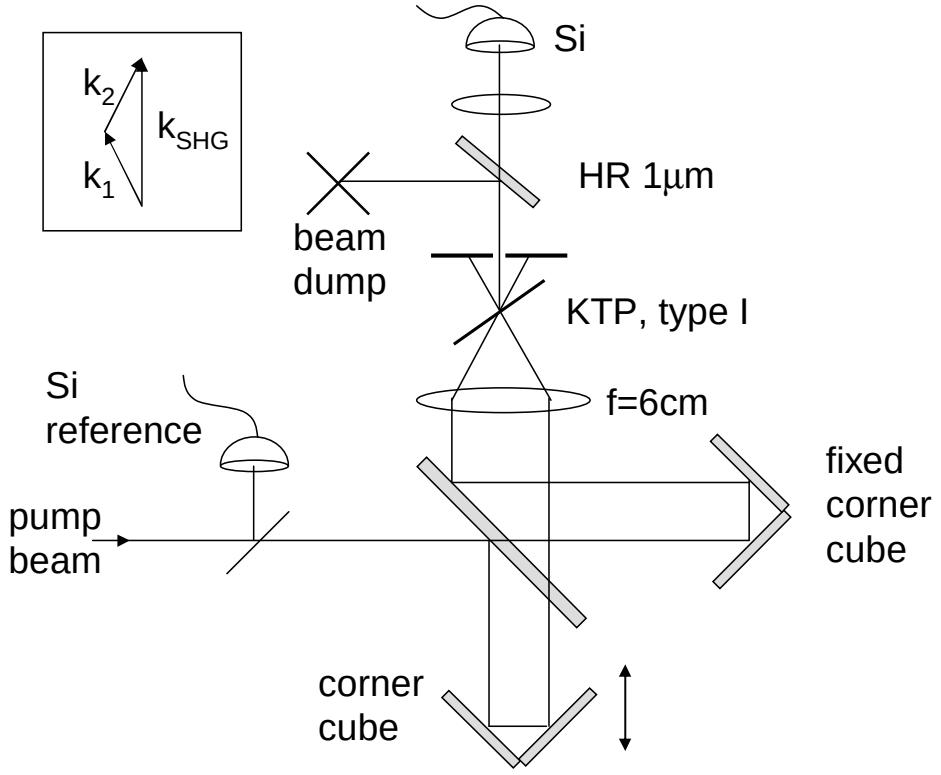

Figure B.4: Intensity autocorrelation experimental setup. The KTP crystal is cut for type I phasematching.

The Fourier transform of the envelope of a first order autocorrelation is directly related to the beam's power spectrum [61]. The bandwidth characteristics of the OPO beam are established in this manner for various intracavity frequency-narrowing elements (see Ch. 3 for a discussion). The experimental arrangement for this technique

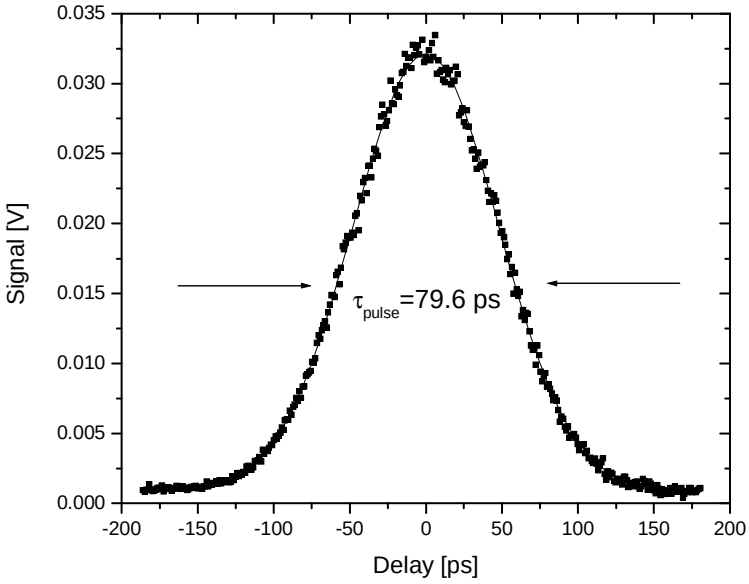

Figure B.5: autocorrelation trace of the OPO pump pulse. Assuming a Gaussian pulse-shape, the Coherent Antares Nd^{3+}:YAG laser has a full width, half maximum pulsewidth of 79.6 ps.

is similar to that shown in Fig. B.1, except no second harmonic crystal is used. Results of measurements with various intracavity elements are shown in Fig. B.6. The dashed line in each plot indicates the Fourier-transform limit corresponding to the measured pulsewidths of two intracavity etalons in Fig. B.6(a) (72 ps), intracavity prism in Fig. B.6(b) (72 ps), and no intracavity element in Fig. B.6(c) (78 ps).

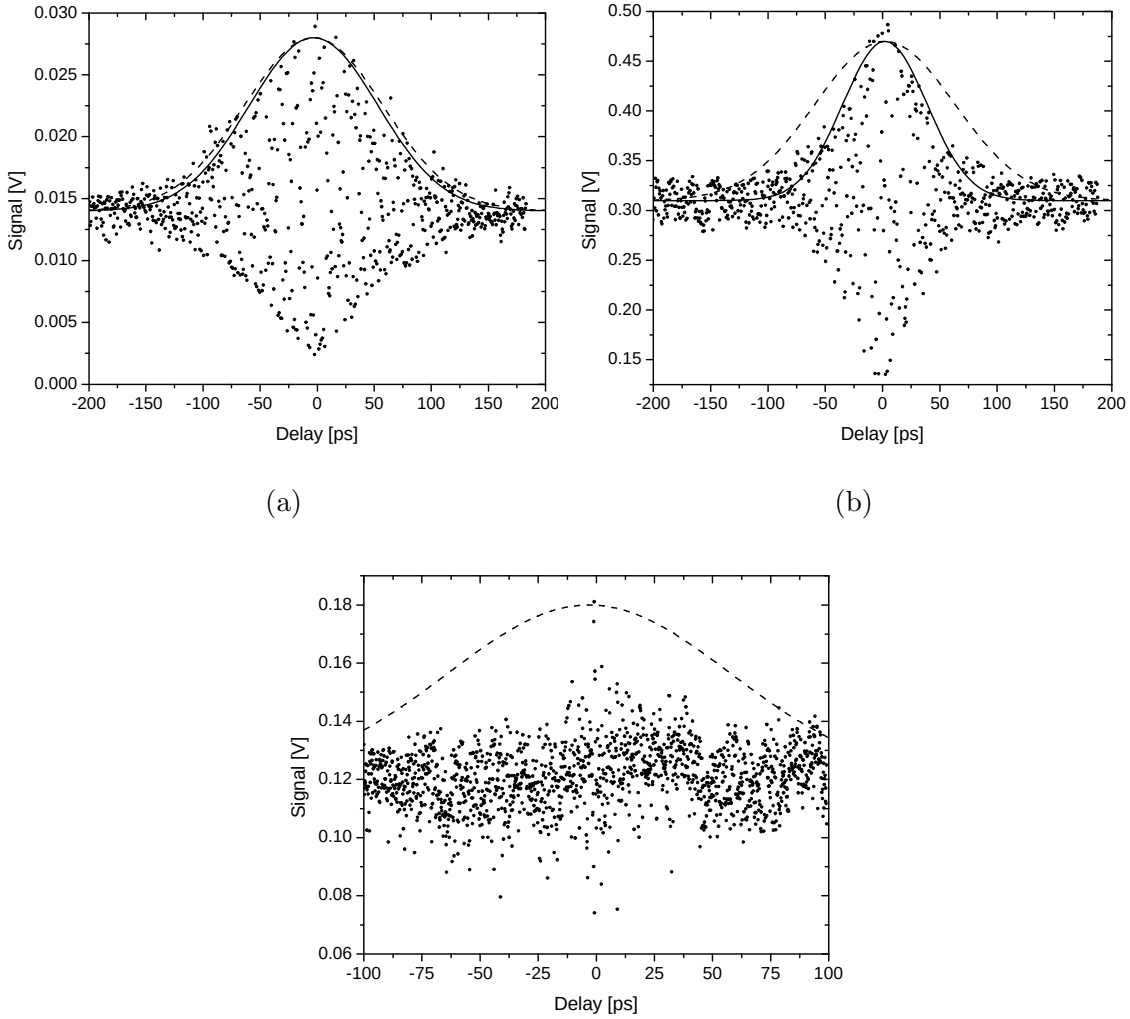

(a) (b)

(c)

Figure B.6: First-order OPO autocorrelation with intracavity etalons (a), prism (b), and no intracavity element (c). The dashed line in each plot corresponds to the Fourier-transform limit of measured pulsewidths: 72 ps (a), 72 ps (b) and 78 ps (c).

Appendix C

Mach-Zehnder interferometer error analysis

As shown in Fig. C.1, the Mach-Zehnder interferometer (MZ) calibration is tested against that of the thermal camera, which is calibrated against a thermocouple as described above, and found to agree to better than 1 K in the region that the camera is not saturated. The solid curve is the phase change due to sample temperature change recorded by the interferometer calibrated to temperature as discussed above. The experimental setup is similar to that pictured in Fig. C.2. Only the last few tens of minutes are shown in the figure as the sample is warming up to room temperature after the pump beam is blocked. The data points correspond to temperature measured by the thermal camera as discussed above with the proper calibration (21.7 pixel values/K) as well as two other incorrect calibrations for comparison. The flat regions of the camera data indicate saturation, expected since blackbody radiation energy flux scales as T^4 and so drops off rapidly from an equilibrium temperature (RT). The agreement between the MZ and camera calibration is well within the resolution of the MZ ($\pm$3 K), which is determined primarily by the possibility of small background phase shifts over time scales of $\sim$1 hr.

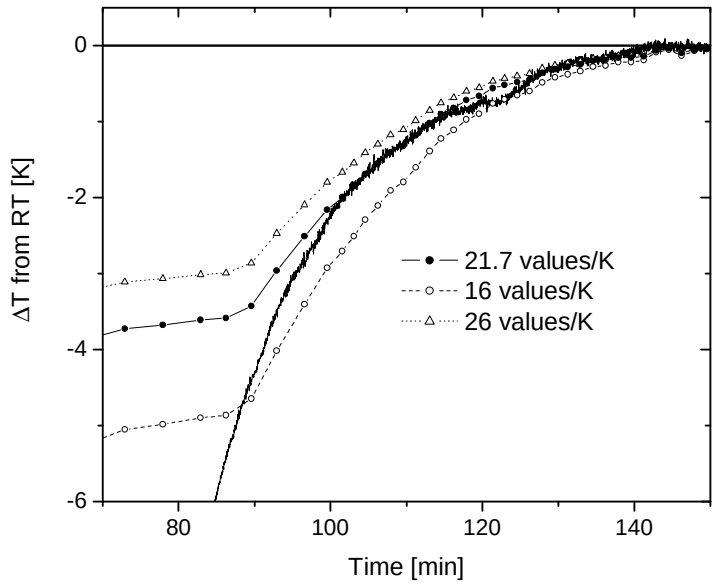

Figure C.1: Mach-Zehnder calibration to thermal camera. The solid line is MZ temperature change data as the sample warms to room temperature. Data points correspond to temperature obtained with the micro-bolometer thermal camera with the proper calibration (21.7 pixel values/K) and two others for comparison.

The MZ calibration discussed above is tested *in-situ* against a thermocouple (TC). In an arrangement similar to the setup shown in Fig. C.2, a TC is attached to the sample with epoxy (Duco cement). The pump is coupled into the sample and temperature is recorded with the MZ and TC simultaneously. Resulting data is shown in Fig. C.3. No direct confirmation of calibrations can be made from the figure. The TC indicates an immediate increase in temperature due to absorption of fluorescence in the surrounding epoxy. The MZ beam spans most of the sample, so there is temperature gradient between the edge of the sample the the location of the TC in the epoxy. As seen in the figure, the sample nevertheless cools and lifts heat from the hot epoxy. When the pump beam is blocked at around 85 min. the temperature gradient is lifted and the TC quickly drops to negative temperature change with respect to RT.

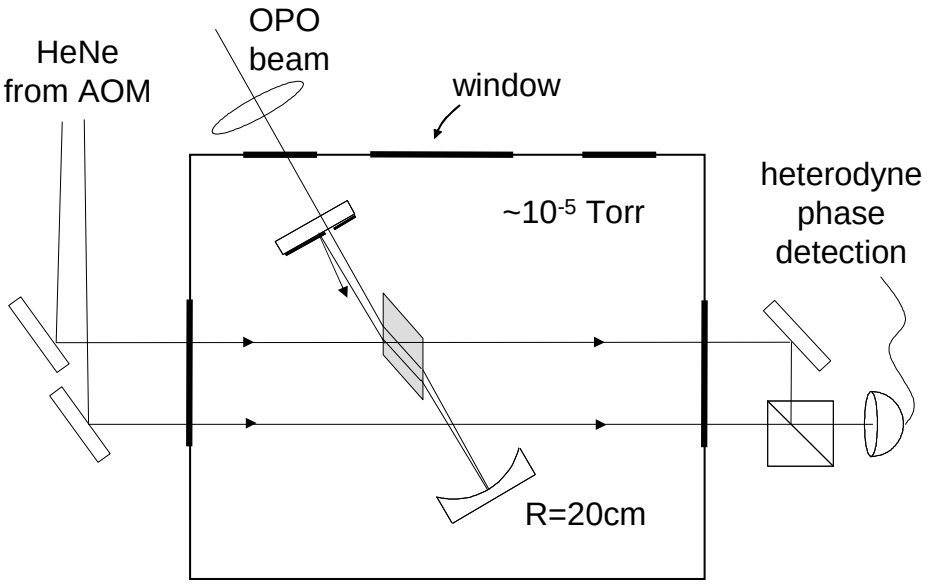

Figure C.2: Brewster sample non-resonant cavity arrangement.

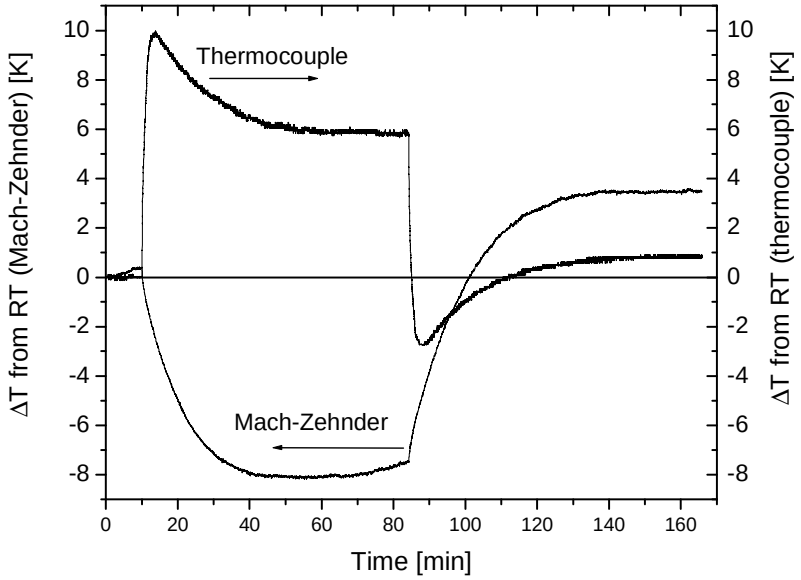

Figure C.3: Mach-Zehnder calibration to thermocouple.

There is an offset of the MZ temperature as the sample approaches equilibrium in Fig. C.3. This offset and others like it are explained by statistical and systematic drifts in the MZ. Statistical drifts are caused primarily by air currents and thermal changes in the optical table on a time scale of tens of minutes. Five experiments measuring these drifts are shown in Fig. C.4. These experiments are identical to those that involve sample cooling except for the absence of the pump and sample. To show the effect of the drift on cooling data, the phase change is scaled to temperature. The longest drift in the figure was taken early in the morning.

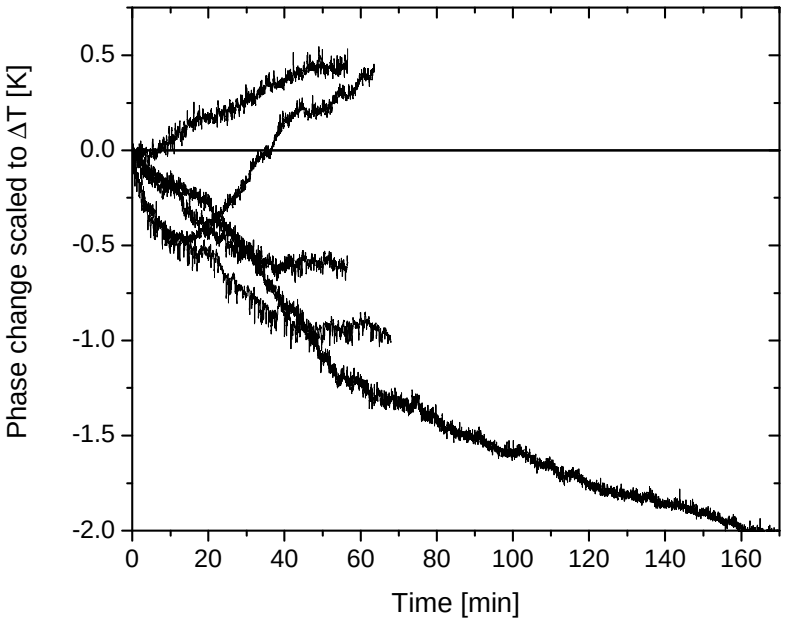

Figure C.4: Mach-Zehnder background drift.

Systematic drifts in the MZ are caused by non-uniform mechanical heating and vary with the particular experimental arrangement. For the multiple-pass configuration shown in Fig. C.5, a DC offset in phase change results from non-uniform heating in the curved mirror. Since the arms of the interferometer pass through different parts of this mirror they encounter different physical lengths. Even assuming uniform temperature across the mirror, Eq. 4.1 indicates that this will lead to a net

change in phase which manifests as a change in sample temperature. To quantify this, numerous experiments are done identical to those involving sample cooling except for the absence of the sample. Figure C.6 shows the results of one of these experiments. The bottom data shows the raw phase change data resulting from a multiple-pass cooling experiment, calibrated to temperature change. The upper trace corresponds to the identical experiment in the absence of the sample. The figure indicates that the background phase shift due to the curved mirror occurs on a fast time scale relative to the time to steady-state sample temperature. Because of this it is straightforward to subtract this DC offset to obtain temperature to within three degrees. The offset is reproducible for a given mirror alignment and linear with respect to pump power. Any change in cavity configuration for experiments using the setup in Fig. C.5 requires a new offset measurement.

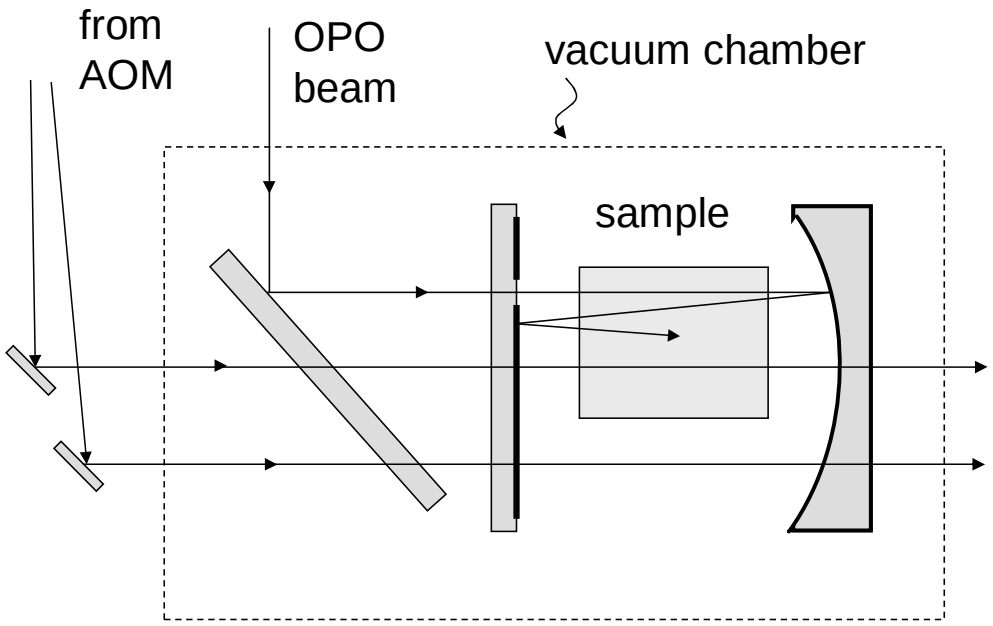

Figure C.5: Cuboid multiple-pass arrangement with interferometer.

A different systematic drift is associated with the experimental arrangement shown in Fig. C.2. Here the MZ beams do not pass through the mirrors forming

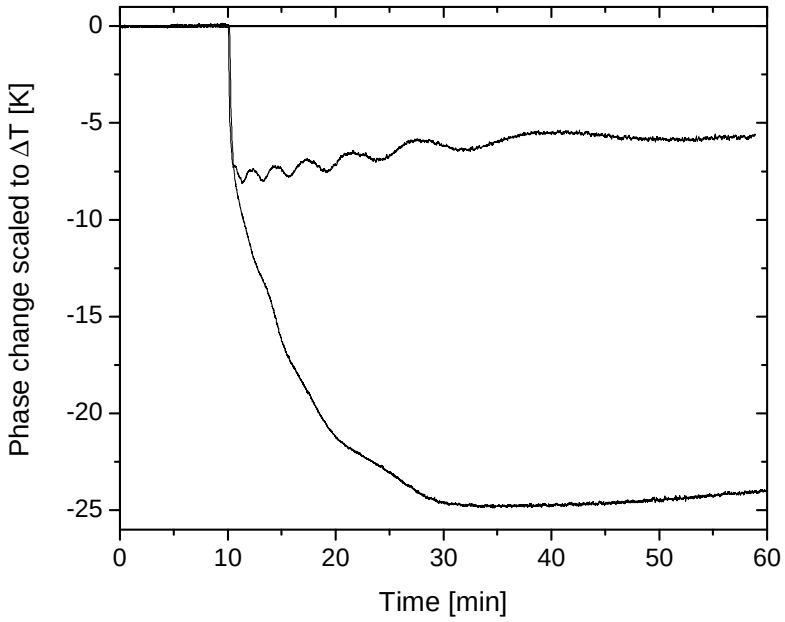

Figure C.6: Mach-Zehnder phase offset for the experimental arrangement in Fig. C.5. Raw phase data is normalized to temperature. The bottom trace indicates phase change when the pump is coupled into the sample. The top trace corresponds to the identical experiment with no sample.

the cavity for multiple pump passes and so avoid the systematic drift just described. However, tests similar to those described above reveal a less extreme but qualitatively reproducible phase change not associated with sample temperature change.

Figure C.7 shows these results. With the sample removed the experiment is performed in a manner identical to cooling experiments with the pump beam blocked in various places. The top three dark traces correspond to the following case: the pump beam passes through the first cavity mirror and is reflected for multiple passes. At a time of ~ 54 min. the pump beam is turned off a distance away from the chamber. The bottom two dark traces correspond to the following case: the pump beam passes through the first mirror and is reflected directly out of the chamber through a chamber window other than that through which the MZ beams pass. Again, at a time

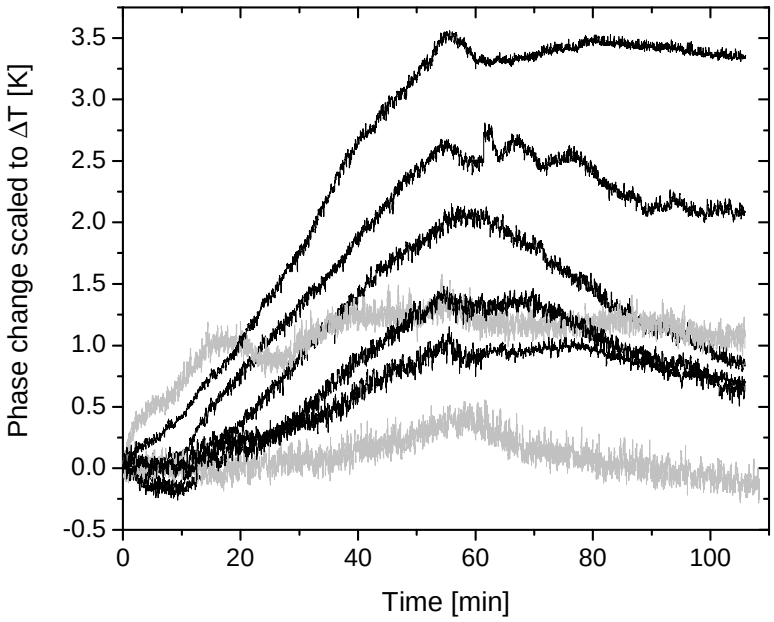

Figure C.7: Mach-Zehnder systematic phase drift for the experimental setup in Fig. C.2.

of ~ 54 min. the pump beam is turned off a distance away from the chamber. The two grey traces correspond to the following case: the pump beam is blocked before it enters the vacuum chamber – the pump is again blocked in the same place as the previous tests at a time of ~ 54 min. These results suggest that the presence of the pump non-uniformly heats the chamber window through which the MZ beams enter. They also indicate that any cooling experiment using this multiple-pass arrangement will suffer a phase change (linear in time) acting opposite to that of actual temperature change. This results in a cold steady-state temperature (pump on) slightly warmer than actuality. Further, the subsequent phase change when the pump is blocked will lead to the indication of an equilibrium temperature warmer than RT. This can be seen in the MZ data in Fig. C.3. Accordingly, phase shifts that are linear in time are subtracted from MZ data in experiments described below that are based on the setup in Fig. C.2. The final RT offset at equilibrium is kept as a measure of

uncertainty.

References

[1] G. Mills, J. Fleming, Z. Wei, and J. Turner-Valle (unpublished).

[2] C. E. Mungan, M. I. Buchwald, B. C. Edwards, R. I. Epstein, and T. R. Gosnell, "Internal laser cooling of Yb^{3+}-doped glass measured between 100 and 300 K," Applied Physics Letters **71,** 1458–1460 (1997).

[3] H. J. Metcalf and P. van der Straten, *Laser Cooling and Trapping* (Springer-Verlag, New York, NY, 1999).

[4] W. D. Phillips, P. L. Gould, and P. D. Lett, "Cooling, stopping, and trapping atoms," Science **239,** 877–883 (1988).

[5] L. Hollberg, S. Chu, J. E. Bjorkholm, A. Cable, and A. Ashkin, "Laser cooling and confining of atoms," Journal of the Optical Society of America A **2,** P50 (1985).

[6] S. Chu, "Cold atoms and quantum control," Nature **416,** 206–210 (2002).

[7] W. D. Phillips, "Laser cooling and trapping of neutral atoms," Reviews of Modern Physics **70,** 721–741 (1998).

[8] W. D. Phillips and H. Metcalf, "Laser deceleration of an atomic beam," Physical Review Letters **48,** 596 (1982).

[9] K. B. Davis, M. O. Mewes, M. R. Andrews, N. J. van Druten, D. S. Durfee, D. M. Kurn, and W. Ketterle, "Bose-Einstein condensation in a gas of sodium atoms," Physical Review Letters **75,** 3969 (1995).

[10] M. H. Anderson, J. R. Ensher, M. R. Matthews, C. E. Wieman, and E. A. Cornell, "Observation of Bose-Einstein condensation in a dilute atomic vapor below 200 nanokelvin," Science **269,** 198 (1995).

[11] M. Sheik-Bahae, M. P. Hasselbeck, and R. I. Epstein, "Prospects for Laser Cooling in Semiconductors," In *Proceedings of the Conference on Quantum Electronics and Laser Science*, p. 103 (Optical Society of America, Washington, DC, 2002).

[12] H. Gauck, T. H. Gfroerer, M. J. Renn, E. A. Cornell, and K. A. Bertness, "External radiative quantum efficiency of 96% from a GaAs/GaInP heterostructure," Applied Physics A - Materials Science and Processing **64,** 143–147 (1997).

[13] E. Finkeissen, M. Potemski, P. Wyder, L. Vina, and G. Weimann, "Cooling of a semiconductor by luminescence up-conversion," Applied Physics Letters **75,** 1258–1260 (1999).

[14] R. C. Powell, *Physics of Solid-State Laser Materials*, Vol. 1 of *Atomic, Molecular, and Optical Physics*, 1 ed. (Springer-Verlag, New York, 1998).

[15] H. Inoue, K. Soga, and A. Makishima, "Simulation of the optical properties of Tm:ZBLAN glass," Journal of Non-Crystalline Solids **306,** 17–29 (2002).

[16] W. J. Miniscalco, in *Rare Earth Doped Fiber Lasers and Amplifiers*, M. J. F. Digonnet, ed., (Marcel Dekker, New York, USA, 1993).

[17] W. T. Carnall, P. R. Fields, and K. Rajnak, Journal of Chemical Physics **49,** 4412 (1968).

[18] C. Kittel, *Introduction to Solid State Physics* (Wiley, New York, 1976).

[19] J. T. Verdeyen, *Laser Electronics*, *Prentice Hall Series in Solid State Physical Electronics*, 3 ed. (Prentice Hall, New Jersey, 1995).

[20] D. E. McCumber, "Einstein relations connecting broadband emission and absorption spectra," Physical Review **136,** A954–A957 (1964).

[21] R. I. Epstein, M. I. Buchwald, B. C. Edwards, T. R. Gosnell, and C. E. Mungan, "Observation of laser-induced fluorescent cooling of a solid," Nature **377,** 500–503 (1995).

[22] J. L. Clark and G. Rumbles, "Laser Cooling in the Condensed Phase by Frequency Up-Conversion," Physical Review Letters **76,** 2037–2040 (1996).

[23] B. C. Edwards, J. E. Anderson, R. I. Epstein, G. L. Mills, and A. J. Mord, "Demonstration of a solid-state optical cooler: An approach to cryogenic refrigeration," Journal of Applied Physics **86,** 6489–6493 (1999).

[24] P. Pringsheim, "Zwei Bemerkungen über den Unterschied von Lumineszenz und Temperaturstrahlung," Zeitschrift für Physik **57,** 739–746 (1929).

[25] L. Landau, "On the thermodynamics of photoluminescence," J. of Physics (Moscow) **10,** 503–506 (1946).

[26] A. Kastler, J. Phys. Radium **11,** 255–265 (1950).

[27] C. W. Hoyt, M. Sheik-Bahae, R. I. Epstein, B. C. Edwards, and J. E. Anderson, "Observation of Anti-Stokes Fluorescence Cooling in Thulium-Doped Glass," Physical Review Letters **85,** 3600–3603 (2000).

[28] J. Fernandez, A. Mendioroz, A. J. Garcia, R. Balda, and J. L. Adam, "Anti-Stokes laser-induced internal cooling of Yb^{3+}-doped glasses," Physical Review B–Condensed Matter **62,** 3213–3217 (2000).

[29] A. Rayner, M. Hirsch, N. R. Heckenberg, and H. Rubinsztein-Dunlop, "Distributed laser refrigeration," Applied Optics **40,** 5423–5429 (2001).

[30] T. R. Gosnell, "Laser cooling of a solid by 65 K starting from room temperature," Optics Letters **24,** 1041–1043 (1999).

[31] S. R. Bowman and C. E. Mungan, "New materials for optical cooling," Applied Physics B - Lasers and Optics **71,** 807–811 (2000).

[32] R. I. Epstein, J. J. Brown, B. C. Edwards, and A. Gibbs, "Measurements of optical refrigeration in ytterbium-doped crystals," Journal of Applied Physics **90,** 4815–4819 (2001).

[33] A. Mendioroz, J. Fernández, M. Voda, M. Al-Saleh, and R. Balda, "Anti-Stokes laser cooling in Yb^{3+}-doped KPb_2Cl_5 crystal," Optics Letters **27,** 1525–1527 (2002).

[34] A. N. Oraevsky, "Cooling of semiconductors by laser radiation," Journal of Russian Laser Research **17,** 471–479 (1996).

[35] L. A. Rivlin and A. A. Zadernovsky, "Laser cooling of semiconductors," Optics Communications **139,** 219–222 (1997).

[36] J. L. Clark, P. F. Miller, and G. Rumbles, "Red edge photophysics of ethanolic rhodamine 101 and the observation of laser cooling in the condensed phase," Journal of Physical Chemistry A **102,** 4428–4437 (1998).

[37] C. W. Hoyt, M. Sheik-Bahae, and M. Ebrahimzadeh, "High power picosecond optical parametric oscillator based on periodically poled lithium niobate," Optics Letters **27,** 1541–1543 (2002).

[38] In publication for a special issue of the Journal of the Optical Society of America B, entitled "Laser Cooling of Matter," May, 2003.

[39] C. W. Hoyt, M. Sheik-Bahae, R. I. Epstein, B. C. Edwards, and J. E. Anderson, "Observation of anti-Stokes fluorescent cooling in thulium-doped glass," In *Post-Deadline Proceedings of the Conference on Quantum Electronics and Laser Science*, p. 17 (Optical Society of America, Washington, DC, 2000).

[40] G. Rumbles, "A laser that turns down the heat," Nature **409,** 572–573 (2001).

[41] S. N. Andrianov and V. V. Samartsev, "Laser cooling of solids," Optics and Spectroscopy **84,** 696–701 (1998).

[42] X. Luo, M. D. Eisaman, and T. R. Gosnell, "Laser cooling of a solid by 21K starting from room temperature," Optics Letters **23,** 639–641 (1998).

[43] B. Heeg, G. Rumbles, A. Khizhnyak, and P. A. DeBarber, "Comparative intra- versus extra-cavity laser cooling efficiencies," Journal of Applied Physics **91,** 3356–3362 (2002).

[44] G. Lamouche, P. Lavallard, R. Suris, and R. Grousson, "Low temperature laser cooling with a rare-earth doped glass," Journal of Applied Physics **84,** 509–516 (1998).

[45] R. Frey, F. Micheron, and J. P. Pocholle, "Comparison of Peltier and anti-Stokes optical coolings," Journal of Applied Physics **87,** 4489–4498 (2000).

[46] T. J. Edwards, G. A. Turnbull, M. H. Dunn, M. Ebrahimzadeh, and F. G. Colville, "High-power, continiuous-wave, singly resonant, intracavity optical parametric oscillator," Applied Physics Letters **72,** 1527–1530 (1998).

[47] P. T. Landsberg and G. Tonge, "Thermodynamic energy-conversion efficiencies," Journal of Applied Physics **51,** R1–R20 (1980).

[48] R. Kosloff, E. Geva, and J. M. Gordon, "Quantum refrigerators in quest of the absolute zero," Journal of Applied Physics **87,** 8093–8097 (2000).

[49] L. Wetenkamp, G. F. West, and H. Tobben, "Optical properties of rare earth-doped ZBLAN glasses," Journal of Non-Crystalline Solids **140,** 35–40 (1992).

[50] R. G. Smart, J. N. Carter, A. C. Tropper, and D. C. Hanna, "Continuous-wave oscillation of Tm^{3+}-doped fluorozirconate fibre lasers at around 1.47 μm, 1.9 μm and 2.3 μm when pumped at 790nm," Optics Communications **82,** 563–570 (1991).

[51] G. Lei, J. E. Anderson, M. I. Buchwald, B. C. Edwards, and R. I. Epstein, "Determination of spectral linewidths by Voigt profiles in Yb^{3+}-doped fluorozirconate glasses," Physical Review B–Condensed Matter **57,** 7673–7678 (1998).

[52] B. Saleh, *Fundamentals of Photonics*, *Wiley Series in Pure and Applied Optics* (Wiley, New York, 1991).

[53] N. H. Balshaw, *Practical Cryogenics: An introduction to laboratory cryogenics*, 1 ed. (Oxford Instruments (UK), Oxon, England, 1996).

[54] R. F. Barron, *Cryogenic Systems*, *Monographs on Cryogenics*, 2 ed. (Oxford University Press, New York, 1985).

[55] B. C. Edwards, M. I. Buchwald, and R. I. Epstein, "Development of the Los Alamos solid-state optical refrigerator," Review of Scientific Instruments **69,** 2050–2055 (1998).

[56] R. L. Byer, "Parametric Oscillators and Nonlinear Materials," In *Nonlinear Optics*, P. G. Harper and B. S. Wherrett, eds., pp. 47–245 (Academic Press, London, 1977).

[57] L. E. Myers, R. C. Eckardt, M. M. Fejer, and R. L. Byer, "Quasi-phase-matched optical parametric oscillators in bulk periodically poled $LiNbO_3$," Journal of the Optical Society of America B **12,** 2102–2116 (1995).

[58] M. E. Dearborn, Optical sciences, University of New Mexico, Albuquerque, New Mexico, 1998.

[59] R. W. Boyd, *Nonlinear Optics*, 1 ed. (Academic Press, San Diego, 1992).

[60] J.-C. Diels and W. Rudolph, *Ultrashort laser pulse phenomena : fundamentals, techniques, and applications on a femtosecond time scale*, *Optics and Photonics*, 1 ed. (Academic Press, San Diego, 1996).

[61] M. V. Klein and T. E. Furtak, *Optics*, *Wiley Series in Pure and Applied Optics*, 2 ed. (John Wiley & Sons, Inc., New York, 1986).

[62] M. Ebrahimzadeh and M. H. Dunn, in *Handbook of Optics IV*, M. Bass, J. M. Enoch, E. W. V. Stryland, and W. L. Wolfe, eds., (Optical Society of Americal, McGraw-Hill, 2000), Chap. Optical Parametric Oscillators, pp. 2201–2272.

[63] B. Ruffing, A. Nebel, and R. Wallenstein, "High-power picosecond LiB_3O_5 optical parametric oscillators tunable in the blue spectral range," Applied Physics B - Lasers and Optics **72,** 137–149 (2001).

[64] T. W. Tukker, C. Otto, and J. Greve, "A narrow-bandwidth optical parametric oscillator," Optics Communications **154,** 83–86 (1998).

[65] C. Grasser, D. Wang, R. Beigang, and R. Wallenstein, "Singly resonant optical parametric oscillator of KTiOPO4 synchronously pumped by the radiation of a continuous-wave mode-locked Nd-YLF laser," Journal of the Optical Society of America B **10,** 2218–2221 (1993).

[66] B. Ruffing, A. Nebel, and R. Wallenstein, "All-solid-state cw mode-locked picosecond $KTiOAsO_4$ (KTA) optical parametric oscillator," Applied Physics B - Lasers and Optics **67,** 537–544 (1998).

[67] W. R. Bosenberg, A. D. Drobshoff, J. I. Alexander, L. E. Myers, and R. L. Byer, "Continuous-wave singly resonant optical parametric oscillator based on periodically poled $LiNbO_3$," Optics Letters **21,** 713–715 (1996).

[68] W. R. Bosenberg, J. I. Alexander, L. E. Myers, and R. W. Wallace, "2.5-W, continuous-wave, 629-nm solid-state laser source," Optics Letters **23,** 207–209 (1998).

[69] M. E. Dearborn, K. Koch, G. T. Moore, and J. C. Diels, "Greater than 100photon-conversion efficiency from an optical parametric oscillator with intracavity difference-frequency mixing," Optics Letters **23,** 759–761 (1998).

[70] K. Finsterbusch, R. Urschel, and H. Zacharias, "Fourier-transorm-limited, high-power picosecond optical parametric oscillator based on periodically poled lithium niobate," Applied Physics B - Lasers and Optics **70,** 741–746 (2000).

[71] S. Guha, F.-J. Wu, and J. Falk, "The effects of focusing on parametric oscillation," IEEE Journal of Quantum Electronics **QE-18,** 907–912 (1982).

[72] A. V. Smith, sNLO nonlinear optics code available from A. V. Smith, Sandia National Laboratories, Albuquerque, NM 87185-1423.

[73] K. Puech, L. Lefort, and D. C. Hanna, "Broad tuning around degeneracy in a singly resonant synchronously pumped parametric oscillator by means of a diffraction grating," Journal of the Optical Society of America B **16,** 1533–1538 (1999).

[74] S. M. Lima, J. A. Sampaio, T. Catunda, A. C. Bento, L. C. M. Miranda, and M. L. Baesso, "Mode-mismatched thermal lens spectrometry for thermo-optical properties measurement in optical glasses: a review," Journal of Non-Crystalline Solids **273,** 215–227 (2000).

[75] J. M. Jewell, C. Askins, and I. D. Aggarwal, "Interferometric method for concurrent measurement of thermo-optic and thermal expansion coefficients," Applied Optics **30,** 3656–3660 (1991).

[76] S. M. Lima, T. Catunda, R. Lebullenger, A. C. Hernandes, M. L. Baesso, A. C. Bento, and L. C. M. Miranda, "Temperature dependence of thermo-optical properties of fluoride glasses determined by thermal lens spectrometry," Physical Review B–Condensed Matter **60,** 15173–15178 (1999).

[77] T. B. Carlson, S. M. Denzer, T. R. Greenlee, R. P. Groschen, R. W. Peterson, and G. M. Robinson, "Vibration-resistant direct-phase-detecting optical interferometers," Applied Optics **36,** 7162–7171 (1997).

[78] R. Kristal and R. W. Peterson, "Bragg cell heterodyne interferometery of fast plasma events," Review of Scientific Instruments **47,** 1357–1359 (1976).

[79] G. M. Robinson, D. M. Perry, and R. W. Peterson, "Optical Interferometry of Surfaces," Scientific American **265,** 66–71 (1991).

[80] A. Brenier, C. Pedrini, B. Moine, J. L. Adam, and C. Pledel, "Fluorescence mechanisms in Tm^{3+} singly doped and Tm^{3+}, Ho^{3+} doubly doped indium-based fluoride glasses," Physical Review B–Condensed Matter **41,** 5364–5371 (1990).

[81] J. McDougall, D. B. Hollis, and M. J. P. Payne, "Spectroscopic properties of Tm^{3+} in ZBLAN fluoride glass. Part 2. Judd-Ofelt parameters," Physics and Chemistry of Glasses **36,** 139–140 (1995).

[82] G. P. Morgan and W. M. Yen, in *Laser Spectroscopy of Solids II*, Vol. 49 of *Topics in Applied Physics*, 1 ed. (Springer-Verlag, Berlin, 1989), Chap. Optical Energy Transfer in Insulators, pp. 77–122.

[83] M. J. Weber, in *Laser Spectroscopty of Solids*, Vol. 49 of *Topics in Applied Physics*, 2 ed. (Springer-Verlag, Berlin, 1986), Chap. Laser excited fluorescence spectroscopy in glass, pp. 189–239.

[84] D. L. Huber, in *Laser Spectroscopy of Solids*, Vol. 49 of *Topics in Applied Physics*, 2 ed. (Springer-Verlag, Berlin, 1986), Chap. Dynamics of incoherent transfer, pp. 83–111.

[85] L. H. Kou, D. Labrie, and P. Chylek, "Refractive-indexes of water and ice in the 0.65 μm to 2.5 μm spectral range," Applied Optics **32,** 3531–3540 (1993).

[86] J. L. Finney, "The water molecule and its interactions: the interaction between theory, modelling, and experiment," Journal of Molecular Liquids **90,** 303–312 (2001).

[87] D. E. McCumber, "Theory of phononterminated optical masers," Physical Review **134,** A299–A306 (1964).

[88] Y. B. Band and D. F. Heller, "RElationships between the absorption and emission of light in multilevel systems," Physical Review A–Atomic, Molecular and Optical Physics **38,** 1885–1895 (1988).

[89] S. Payne, L. L. Chase, L. K. Smith, W. L. Kway, and W. F. Krupke, "Infrared cross-setion measurements for cystals doped with Er^{3+}, Tm^{3+} and Ho^{3+}," IEEE Journal of Quantum Electronics **28,** 2619–2630 (1992).

[90] W. Demtröder, *Laser Spectroscopy: Basic Concepts and Instrumentation*, Vol. 5 of *Springer Series in Chemical Physics*, 2 ed. (Springer-Verlag, Berlin, 1996).

[91] Personal communication with Michael Hasselbeck and Mansoor Sheik-Bahae.